Bound by
Abbey
Bookbinding Co.
105 Cathays Terrace, Cardiff CF24 4HU, U.K.
Tel: +44 (0)29 2039 5882
Email: info@bookbindersuk.com
www.bookbindersuk.com

CARDIFF UNIVERSITY
PRIFYSGOL CAERDYDD

Sir Herbert Duthie Library
Llyfrgell Syr Herbert Duthie

University Hospital
of Wales
Heath Park
Cardiff
CF14 4XN

Ysbyty Athrofaol Cymru
Parc y Mynydd Bychan
Caerdydd
CF14 4XN

029 2074 2875
duthieliby@cardiff.ac.uk

Monte Carlo Portal Dosimetry

Pik Wai CHIN

A thesis presented to the University of Wales in partial fulfilment of the requirements for the degree of Doctor of Philosophy

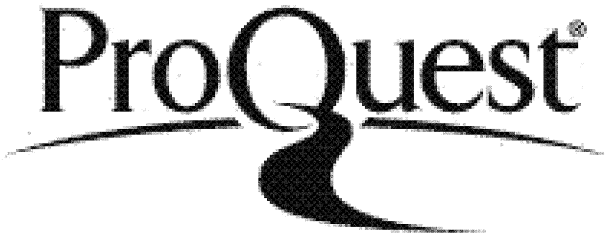

ProQuest LLC
789 East Eisenhower Parkway
P.O. Box 1346
Ann Arbor, MI 48106-1346

春夏秋冬走三回
讀生命中的燦爛
寫點滴滴的光彩

spring summer autumn winter walk three rounds. read radiance of life. write overflowing colours of light

Contents

ACKNOWLEDGMENTS

I thank

- Cancer Research Wales and Yr Ysgol Uwchradd Tregaron, for funding.
- Geraint Lewis and Cyril Smith, for the incredible opportunities.
- Emiliano Spezi, for the tradition of excellence.
- Jeffrey Siebers, for co-supervising part of the work (Chapter 6).
- Paul Keall et al. at VCU and Phil Evans et al. at ICR/RMH, for imaging facilities and helpful discussion.
- Frank Verhaegen and Amanda Barry, for reviewing the thesis.
- Rebecca Cufflin, for proof-reading the thesis.
- Jonathan Giddy, for facilitating High Throughput Computing services.
- colleagues at Velindre Cancer Centre, for friendship and tremendous support.
- Richard Jarvis, for assistance with image acquisition.
- Mel Jones et al., for making the phantoms.
- Andrew Edwards, for fixing the bike.
- colleagues in the scientific community far and near, for encouragement.
- housekeepers and porters at Neuadd Meirionnydd, for laughter.
- Sr Hermine, for being an inspiration still.
- Dato' Dr Sivananthan and the late Dato' Dr Pathmanathan, for medical care when I was tiny.
- physics, for 16 years of fascination.
- Brecon Beacons, for your contours of beauty.
- and the ponies, for the rhythm.
- friends and family 7000 miles away, for blessings.
- Sayang, for *sayang*.

List of Tables

List of Figures

ABSTRACT

This project developed a solution for verifying external photon beam radiotherapy. The solution is based on a calibration chain for deriving portal dose maps from acquired portal images, and a calculation framework for predicting portal dose maps. Quantitative comparison between acquired and predicted portal dose maps accomplishes both **geometric** (patient positioning with respect to the beam) and **dosimetric** (2D fluence distribution of the beam) verifications. A disagreement would indicate that beam delivery had not been according to plan. The solution addresses the clinical need for verifying radiotherapy both **pre-treatment** (without patient in the beam) and **on-treatment** (with patient in the beam). Medical linear accelerators mounted with electronic portal imaging devices (EPIDs) were used to acquire portal images. Two types of EPIDs were investigated: the amorphous silicon (a-Si) and the scanning liquid ion chamber (SLIC). The EGSnrc family of Monte Carlo codes were used to predict portal dose maps by computer simulation of radiation transport in the beam-phantom-EPID configuration. Monte Carlo simulations have been implemented on several levels of High Throughput Computing (HTC), including the Grid, to reduce computation time. The solution has been tested across the entire clinical range of gantry angle, beam size (5 cm $\times$ 5 cm to 20 cm $\times$ 20 cm), beam-patient and patient-EPID separations (4 cm to 38 cm). In these tests of known beam-phantom-EPID configurations, agreement between acquired and predicted portal dose profiles was consistently within 2% of the central axis value. This *Monte Carlo portal dosimetry* solution therefore achieved combined versatility, accuracy and speed not readily achievable by other techniques.

Monte Carlo Portal Dosimetry

Chapter 1

INTRODUCTION

Radiation physics is around us and in many ways, for us. It underlies microwave ovens, smoke detectors, airport luggage scanners and nuclear power plants. In medicine, radiation physics has been applied for medical diagnosis and therapy, tissue analysis and equipment sterilisation.

In therapeutic applications, radiation may be administered in a variety of ways e.g. accelerator-generated radiation particles (external beam radiotherapy), sealed (brachytherapy) and unsealed (nuclear medicine) radionuclides. Today, most radiotherapy clinics around the world routinely treat cancer patients using photons and electrons generated by linear accelerators (linacs), which have been around since the early 1950s [Greene and Williams 1997]. Alternative particles [Brahme 2004, Li et al. 2004, Suortti and Thomlinson 2003, Moch et al. 2002, Burmeister et al. 2003, Jakel et al. 2003] and recent technologies such as state-of-the-art helical tomotherapy* [Mackie et al. 1993, Jeraj et al. 2004] are not widely available. This thesis focuses on linac-generated photon beams.

*Tomotherapy is based on a linac mounted on a CT-like ring, in which the beam rotates around the patient to deliver "slice therapy".

1.1 Radiotherapy

Figure 1.1 illustrates how photon beam radiotherapy works. Carefully controlled, the destructive power of radiation is invoked to achieve biological damage to cancerous cells. Photons enter the patient's body and interact with body tissues, generating showers of secondary photons and charged particles (to be discussed in Chapter 3). Energy is deposited along the tracks of these charged particles. This gives rise to highly reactive chemical species which cause DNA damage by impairing cellular functions for progeny production [Johns and Cunningham 1983].

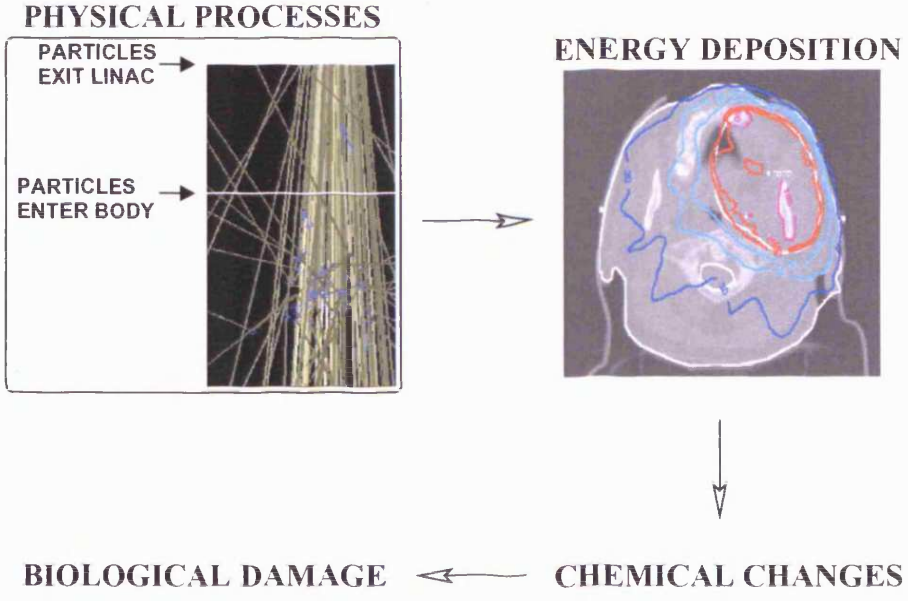

Figure 1.1: How radiotherapy works: from physical processes (photon tracks in yellow, electron tracks in blue) and energy deposition (isodoses connect points of equal dose deposition) in targeted body tissues to chemical changes, and on to biological damage. Image on the right courtesy of E. Spezi.

To improve external beam radiotherapy, continuous research interests have been to shape the beam conformally to the target volume and at the same time avoid the

tissues outside the target volume, particularly radio-sensitive organs. Traditionally, beam shapes were regular (e.g. rectangular) and the dose distribution uniform. More recently, conformal beam-shaping and intensity modulation have been implemented in many clinics alongside the installation of multileaf collimators (MLC) to enable irregularly-shaped beam collimation [Webb 1997, Kutcher et al. 1995]. Such complex treatments typically require many contributing *beamlets* of irregular shapes and non-uniform dose distribution, aimed from different angles at the patient (Figure 1.2). Associated with complex radiation treatments is an increase in the degrees of freedom in various beam-defining parameters. Therefore, stringent verification is crucial [Shalev 1995].

Figure 1.2: The concept of intensity modulated radiation therapy (IMRT). Contributing *beamlets* are shown with corresponding intensity distributions. Image reproduced from www.mayfieldclinic.com.

Pre-treatment verification guards against errors in treatment planning, dose computation, and transfer of parameters to the treatment machine. A thorough pre-treatment verification exercise, however, does not eliminate the need for on-treatment

verification. This is because it is impossible to ascertain linac performance ahead of time* [Mayles et al. 1999], and it is difficult in practice to reproduce patient positioning perfectly with respect to the beam. Although unable to prevent an error, on-treatment verification provides the only knowledge of the radiation actually delivered to the patient. In the event of an error being detected, prompt correction can usually compensate for the inaccuracy in the course of a fractionated therapy, where dose is delivered to the patient over a series of treatment sessions.

Diode arrays and thermoluminescent dosimeters (TLDs) are conventionally used for treatment verification [Khan 1994, Williams and Thwaites 2000, Letourneau et al. 2004]. However, since they are usually placed on the patient's skin surface, dose verification is usually limited to a number of superficial points. 2D, 3D and 4D† verification, whether pre-treatment or on-treatment, is made possible by capturing images during radiotherapy.

1.2 Imaging During Radiotherapy

The purpose of capturing images during radiotherapy is not for diagnostic investigation, but rather to:

- detect and rectify machine and operator errors;

- detect and rectify day-to-day positional variations of the patient;

*E.g. a 100% overdose has been reported as due to the failure of a timer interface card, causing lack of beam hold during MLC motion. A database containing reports of adverse events is available at the United States Food and Drug Administration website www.accessdata.fda.gov/scripts/cdrh/cfdocs/cfMAUDE/search.cfm.

†The 4th dimension accounts for intra-fractional temporal changes such as respiratory motion.

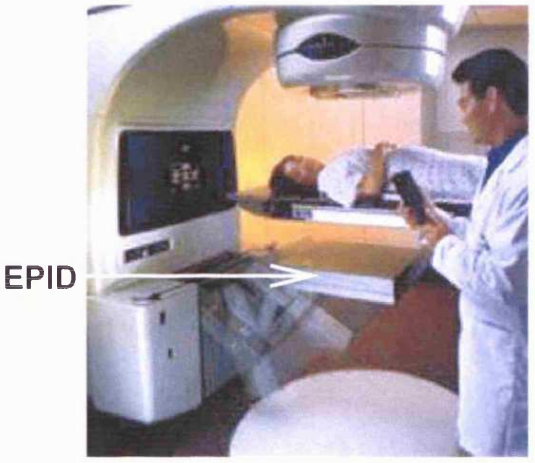

Figure 1.3: A linac mounted with a retractable electronic portal imaging device (EPID). Image adapted from www.varian.com.

- account for inter-fractional and intra-fractional variations in the patient's anatomy such as respiratory motion and changes in bowel filling.

Early efforts at capturing images during treatment were reported by Nielsen and Jensen [1942] for an oesophageal treatment. A stationary photon beam was directed towards the patient. The exit rays hit a fluorescent screen. By viewing the screen through a lead glass window, beam positioning was corrected remotely during treatment delivery.

Image capture during therapy had been primarily film-based despite various deficiencies such as delay in film development, low contrast, narrow *film latitude**, noise associated with film granularity, batch-to-batch inconsistencies and susceptibility to under- and over-exposures. Digital, non-film technology – the electronic portal imaging device (EPID) – began in the 1980s [Boyer et al. 1992, Munro 1995, Herman et al.

*The *film latitude* is the possible range of exposures characterised by the film's characteristic curve.

2001, Antonuk 2002]. EPIDs provide 2D transmission images by capturing images on a plane at the exit side of the patient (Figure 1.3). Apart from real-time operation, digital systems offer better image processing (e.g. windowing, histogram equalisation to improve contrast), display (e.g. registration) and storage. Newer approaches aim for 3D and even 4D imaging by integrating various imaging modalities with the linac. Table 1.1 summarises existing and developing technologies used for digital imaging during radiotherapy.

Table 1.1: Technologies for digital radiotherapy imaging.

Technology	References	Clinical Implementation
camera-based EPID	Partridge et al. [1999], Pang and Rowlands [2000]	Siemens[a] BeamView, Elekta[b] SRI100
scanning liquid ion chamber (SLIC) EPID	van Herk and Meertens [1988], van Herk [1991], Eberle et al. [2003]	Varian[c] PortalVision Mk I and II
amorphous silicon (a-Si) EPID	Antonuk et al. [1996, 1997], Munro and Bouius [1998]	Varian PortalVision aS500 and aS1000, Elekta iViewGT
linacs integrated with cone-beam CT	van Herk et al. [2004], Jaffray et al. [2002], Jaffray [2004]	under study at Netherlands Cancer Institute and Princess Margaret Hospital
linacs integrated with CT-on-rails	Dong et al. [2004]	under study at M. D. Anderson Cancer Centre
linacs integrated with MR	Raaymakers et al. [2004]	under study at University of Utrecht
linacs integrated with ultrasound	as reported by van Herk et al. [2004]	under study in Grenoble

[a]Siemens Medical Solutions. The website is at www.medical.siemens.com.
[b]Elekta Radiation Oncology Solutions. The website is at www.elekta.com.
[c]Varian Medical Systems. The website is at www.varian.com.

Of particular interest in this thesis are the scanning liquid ionisation chamber (SLIC) and the amorphous silicon (a-Si) EPIDs, which will be discussed in detail in Chapter 2.

1.3 Monte Carlo Simulations

The term *Monte Carlo* (MC) was coined by von Neumann in the 1940s [Nahum 1988] to designate a class of numerical methods based on random numbers. Thus named because it is the computer *simulation** of radiation events by "spinning the wheel of chance" or "throwing the dice". Thus designed because events in the birth, life and death of each radiation particle are by nature stochastic.

The contribution of MC simulations towards precise and accurate radiotherapy is not new. MC-derived stopping-power-ratios significantly improved absolute determination of absorbed dose to water using air-kerma calibrated ionisation chambers [Andreo 1988]. To varying extents, MC radiation transport is the foundation for many conventional, kernel-based dose calculations e.g. convolution/superposition techniques [Ahnesjö and Aspradakis 1999]. With increasing demands of complex radiotherapy modalities (Section 1.1), however, restricting MC simulations to a one-off kernel-generation stage is no longer adequate. Interest is therefore growing for implementing case-by-case MC simulations in the clinic.

Details of MC simulations will be given in Chapter 3. An overview here will suffice. Figure 1.4 outlines the working of a MC simulation. The MC simulation code (commonly called *MC engine*) reads in the desired source (e.g. particle type, energy, direction and position), geometry (e.g. coordinates of orthogonal planes), transport parameters (e.g. threshold energy below which tracks should be terminated) and

*Throughout this thesis, *simulation* refers to MC simulation of radiation transport in the computing environment. It should not be confused with the *simulation* procedure which is part of radiotherapy planning, where the patient is positioned as would be during treatment and is scanned using a simulator machine.

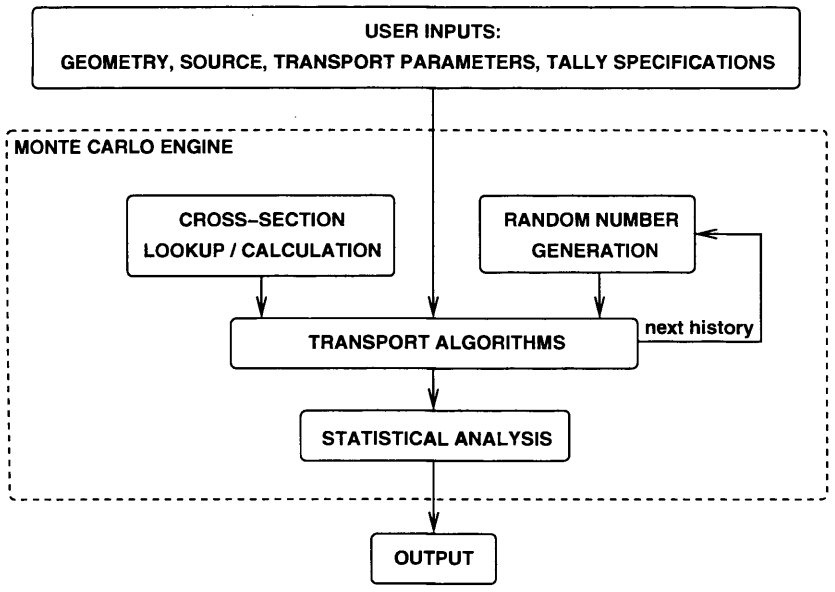

Figure 1.4: How MC simulations work.

*tally** specification (e.g. dose in a specified region). Using a *pseudorandom number*†, a particle is created. During the lifetime of this particle, secondary particles may be created, resulting in a *shower* or a *cascade* of particles. Each particle track is simulated based on interaction physics. A *history* finishes when the particle and all its secondaries

- travel beyond the "universe" of the specified geometry; or

- lose so much energy that the remaining energy falls below a user-defined threshold, determined such that eventual contribution of the particle to the *tally* is expected to be negligible.

*A *tally* is the quantitative outcome the user requests of the simulation.

†In a true random sequence, it would be theoretically impossible to predict the next digit based on the digits up to a given point. Numerical methods normally use digits generated deterministically using algorithms – which means that the next digit can be predicted. Hence the term *pseudorandom*, which is effectively random so long as repetition does not occur within the lifetime of the application.

Computation then moves on to the next history by creating and tracking another particle, and the subsequent shower, using a different *pseudorandom number*. The total number of histories is decided by the user according to statistical requirement. The higher the number of histories, the longer the run time. Each history serves as an independent sample contributing towards the simulation result or *tally*, which is a statistical estimate. When the number of histories simulated is large enough, quantitative information on the transport process may be obtained by averaging over the histories.

Serial computation of millions of histories, one after another, requires long run times*. This is clinically impractical. Hence the delay in implementing MC simulations in radiotherapy clinics.

Parallel computation of histories by distributing the computation over many processors, all working simultaneously, shortens run times. In pursuit of shorter run times, cluster-computing is gaining popularity, to the extent of becoming a necessity, within the MC community [Love et al. 2000, Seco et al. 2005]. The next section goes beyond clusters.

1.4 Grid Computing

The *Grid* is an emerging infrastructure expected to transform our society, particularly in science and industry [Foster and Kesselman 2003]. The idea is to provide computing resources in a way analogous to the electric power grid – pervasive supply on demand.

*Weeks, for a typical clinical case, on an average computer of today.

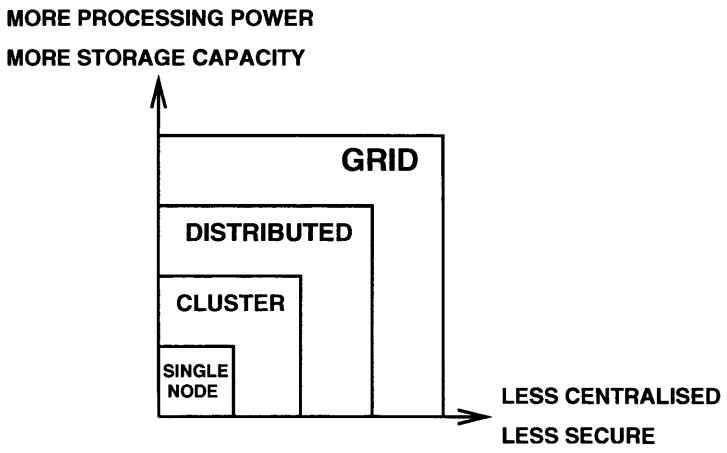

Figure 1.5: Distributed processing in context: single node, cluster, distributed and Grid computing.

Figure 1.5 puts into context the various levels in distributed processing. Cluster computing is simpler because it usually adopts a common operating system; ownership is typically single and local, allowing good control; workload is normally predictable, allowing easy coordination. *Grid* resources, on the other hand, have heterogeneous operating systems managed by service providers; interfacing is complex; resources are abundant; security issues require care.

By combining large-scale resource sharing – computers, networks, data, sensors and people – *Grid* computing is expected to allow new modes of scientific enquiry, previously not feasible, to emerge. It is envisaged to be the problem-solving environment especially for simulation-based and data-intensive sciences.

That is the outlook. Software infrastructure for the *Grid* is under rigorous development towards realising a persistent, coherent, self-regulating *plug-and-play* utility service. Whereas the *Grid* has been extensively deployed in some experimental and

observational areas of physics, medical physics applications such as MC calculations for radiotherapy are only now being initiated into the *Grid* [Chin et al. 2004a]. This thesis presents some initial contributions, results of a joint effort with the Welsh *e-Science** Centre.

1.5 Objective & Context

The objective of this thesis is to develop a clinically practical MC calculation solution for predicting "virtual" portal images for dosimetric verification of external photon beam radiotherapy.

Portal images have been primarily used **qualitatively** for verifying patient setup. Table 1.2 summarises the clinical applications of EPIDs. Of increasing interest is portal dosimetry – **quantitative** use of portal images for 2D dose verification. The demand is largely driven by the clinical need for efficient IMRT verification. Two approaches to using portal dosimetry for treatment verification are:

- **forward portal dose prediction**, where the treatment-time image is compared against the predicted image; and
- **patient dose reconstruction**, where the treatment-time image is used to derive the dose actually received by the patient.

So far, efforts in portal dose prediction have been generally based on:

* *e-Science* refers to the large scale science carried out through distributed global collaborations enabled by the Internet. Such collaborative scientific enterprises typically require access to very large data collections, very large scale computing resources and high performance visualisation.

Table 1.2: Clinical applications of EPIDs.

Application	References
Patient setup verification	Lam et al. [1993], Elgayed et al. [1993], Hunt et al. [1995], Bel et al. [1995], Luchka and Shalev [1996], Pouliot and Lirette [1996], Millar et al. [1997], Yan et al. [1998], Girouard et al. [1998], Boxwala et al. [1999], Samson et al. [1999], Pisani et al. [2000], de Boer et al. [2001], Hatherly et al. [2001], Phillips et al. [2002], Vetterli et al. [2004]
MLC trajectory verification	Keller et al. [1998], Partridge et al. [2000], James et al. [2000], Chen et al. [2002], Ploeger et al. [2002], Popescu et al. [2002], Samant et al. [2002], Vieira et al. [2002], Fielding et al. [2002], Obcemea et al. [2003], Sonke et al. [2004], Chang et al. [2004]
Linac QA	Kirby and Williams [1995], Luchka et al. [1996], Hierholz et al. [1999]
Compensator design and verification	Roback and Gerbi [1995], Evans et al. [1998], Menon and Sloboda [2003]
Organ motion studies	Vigneault et al. [1997], Kroonwijk et al. [1998], Kubo et al. [1999], Vantienhoven et al. [1991], Kaatee et al. [2002], Ford et al. [2002], van Asselen et al. [2003], Berbeco et al. [2003]
2D dose verification	Yin et al. [1994], Zhu et al. [1995], Essers et al. [1996], McNutt et al. [1996, 1997], Boellaard [1998], Keller et al. [1998], Curtin-Savard and Podgorsak [1999], Pasma et al. [1999], El-Mohri et al. [1999], Chang et al. [2001], van Esch et al. [2001], McCurdy et al. [2001], Spezi and Lewis [2002], Grein et al. [2002], Chang et al. [2002], Islam et al. [2003], Greer and Popescu [2003], Warkentin et al. [2003], van Esch et al. [2004]

- convolution/superposition algorithms, which ignore spectral differences and beam hardening, and can be inaccurate particularly when scatter conditions differ from that of the one-time scatter kernel generation. These algorithms have been adopted in all dosimetric work cited in Table 1.2 except Keller et al. [1998], Spezi and Lewis [2002] and Siebers et al. [2004].

- image-to-dose calibration which assumes the EPID to be dosimetrically water-equivalent. This assumption is inherent of all convolution/superposition work cited in Table 1.2 except McCurdy et al. [2001] and Warkentin et al. [2003].

These features impose some constraints, such as:

- the EPID must be placed at least 80 cm away from the patient exit plane [Boellaard 1998], which is clinically impractical; and

- no attenuating objects such as a patient or a phantom could be included in the calculation [van Esch et al. 2004], thereby ruling out on-treatment verification.

This PhD project (April 2002 to March 2005) provides a MC solution for radiotherapy verification of external photon beams, developing work initiated within the same institution [Spezi and Lewis 2002]. In addition to overcoming the limitations of convolution/superposition methods, the work developed herein allows portal dose prediction for oblique beams, which has not been previously reported.

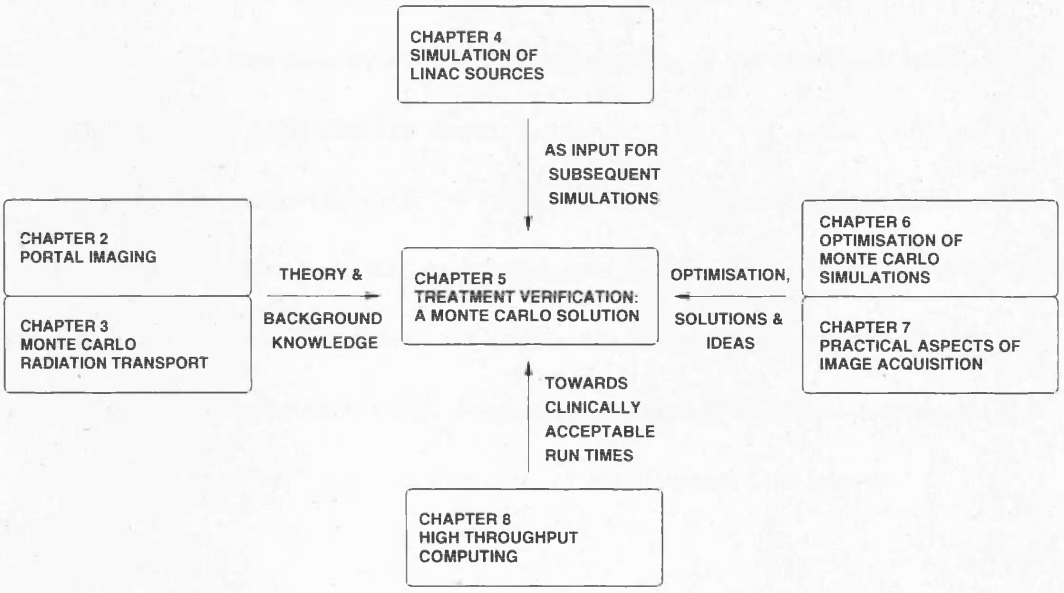

Figure 1.6: Thesis structure.

1.6 Thesis Structure

Chapter 5 is the core of the thesis where its main objective is accomplished. It reports the development of a treatment verification solution which combines the accuracy of MC simulations with the technology of EPIDs. As outlined in Figure 1.6, the other chapters support Chapter 5. Chapters 2 and 3 lay out the theory and background knowledge fundamental to the scope of the thesis. Chapter 4 details the MC simulation of a medical linear accelerator; simulation output from here was subsequently used as radiation source for simulations in Chapter 5. Chapter 6 and 7 further enhance the treatment verification solution by introducing optimisation, new ideas and solutions to problems. Chapter 8 describes how the long run times of MC simulations

may be overcome with several levels of *High Throughput Computing** (HTC), including the *Grid*; this prepares for clinical implementation of the treatment verification solution. Chapter 9 concludes the thesis.

As will be summarised in Table 9.1 and listed in Appendix A, some content of this thesis has already been published in journals and conference proceedings during the project. For all the work reported, the author has been the lead author. Co-authors and collaborators contributed in the form of supervision or technical assistance. It is in this context that "we" is sometimes used in the chapters that follow.

**High Throughput Computing* is an environment that can deliver large amounts of processing capacity over long periods of time.

Chapter 2

ELECTRONIC PORTAL IMAGING

Electronic portal imaging devices (EPIDs) have been introduced in Section 1.2. This chapter begins by introducing the key parameters quantifying imager performance, followed by a discussion on the EPID technologies investigated in this thesis: the scanning liquid ion chamber (SLIC) and the amorphous silicon (a-Si) EPIDs.

2.1 Imager Performance

Fundamentals of medical radiography are covered in several textbooks (e.g. Barrett and Swindell [1981], Webb [1988], Hasegawa [1991]). A portal image is formed by a scatter fluence component added to a primary fluence component; the combined fluence is then modulated by the detector response. In the following section, quantities giving an objective measure of image quality will be described in three levels:

1. basic quantities: contrast, spatial resolution and noise;

2. integrating quantities: modulation transfer function (MTF) and signal-to-noise ratio (SNR);

3. unifying quantity: detective quantum efficiency (DQE).

Contrast describes how much an object stands out from its surroundings. It can be defined by taking into account of the image formation process (Figure 2.1) and is described using

$$contrast = \frac{\phi_{p1} - \phi_{p2}}{\phi_{p1}} \tag{2.1}$$

where ϕ_{p1} and ϕ_{p2} are as defined in Figure 2.1. From Equation (2.1), it can be seen that the greater the difference in attenuation of the object from that of the background, the better the contrast. Due to the strong Z-dependence of photoelectric cross sections, bony structures are differentiated better than soft tissues.

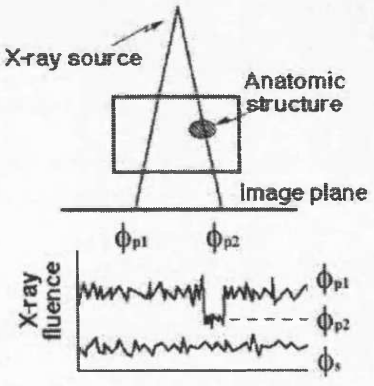

Figure 2.1: Image formation in x-ray transmission radiography. ϕ_{p1} and ϕ_{p2} are photon fluences reaching the image receptor attenuated and unattenuated by the anatomic structure respectively; ϕ_s is the scatter fluence reaching the detector. Reproduced from Herman et al. [2001].

Spatial resolution describes how well edges can be detected. This is the minimum distance at which two objects may be resolved. It depends on the source size, pixel size and image magnification.

Noise in a radiographic image is the uncertainty in signal arising from two main sources:

1. statistical fluctuations in the number of photons detected per unit area (quantum noise);

2. fluctuations due to the properties of the imaging receptor and the display system.

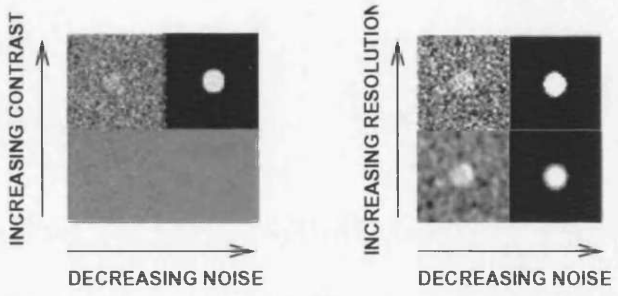

Figure 2.2: Interplay between contrast, resolution and noise on the detectability of a white disc against a black background. Images have been extracted from www.ge.com.

Figure 2.2 shows the interplay between contrast, spatial resolution and noise on the detectability of a white disc against a black background. Detectability is low when: 1) the noise is high even if the contrast or resolution is excellent; or 2) the noise is minimal but the contrast or resolution is poor. By itself, none of the three quantities is adequate in characterising imager performance.

To gauge the interplaying effects between contrast and resolution, the MTF was defined. It is calculated from the Fourier transform of the point spread function. The MTF measures the sharpness, or blur, by characterising how well the system passes different spatial frequencies.

To gauge the interplaying effects between contrast and noise, the SNR was defined:

$$SNR = \frac{\phi_{p2} - \phi_{p1}}{\sqrt{\frac{1}{2}(\phi_{p2} + \phi_{p1} + 2\phi_s)}} \tag{2.2}$$

ϕ_{p1}, ϕ_{p2} and ϕ_s are as given in Figure 2.1. The SNR varies through various stages of image production as more noise is introduced.

The DQE combines the effects of all three basic quantities: contrast, resolution and noise. It tells how efficient the imaging system is at transferring the input information to the output image.

$$DQE = \left(\frac{SNR_{output}}{SNR_{input}}\right)^2 \tag{2.3}$$

It should be emphasised that SNR_{output} should be measured at a point in the detecting system following which no further degradation in SNR is observed [Barrett and Swindell 1981]. The single parameter DQE is representative of image quality and object detectability. Maximising the DQE is therefore the ultimate goal in imager design.

2.2 Megavoltage Imaging

A transmission imaging system consists of a radiation source, the object being imaged and a detector (Figure 2.3). EPIDs, like diagnostic X-ray units, are transmission

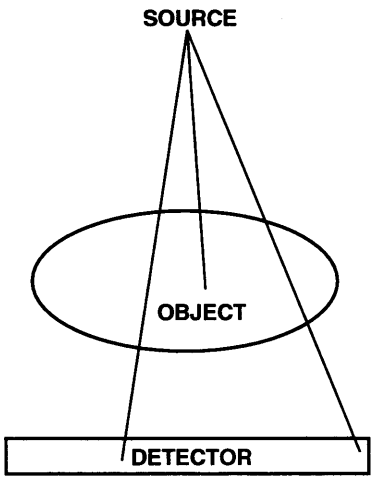

Figure 2.3: A transmission imaging system. X rays transmitted through the object being imaged are detected by the detector.

imaging systems. Electronic portal images (EPIs) are projection maps of photon attenuation (and scatter), similar to X-ray images. Megavoltage (MV) imaging with EPIDs, however, differs from kilovoltage (kV) imaging with diagnostic X-ray machines, as summarised in Table 2.1. Megavoltage images are generally considered poorer in image quality than the kilovoltage equivalent, due to the decrease in contrast, increase in scatter, and the larger size of the radiotherapy source.

Figure 2.4 illustrates visually the difference between kV and MV imaging. On the kV image, bony structures are particularly clear due to high photoelectric absorption in bone. On the MV image, bones are invisible because the dominant process is Compton scattering, which is almost independent of Z. Instead, image contrast is provided by differences in density. Poor discrimination of bony structures at the MV range is explained in Figure 2.5 which plots the bone-to-water and air-to-water contrasts.

Table 2.1: Kilovoltage versus megavoltage imaging.

	Kilovoltage	**Megavoltage**
Image function	Morphological diagnosis.	Radiotherapy record, verification and rectification.
Design	Optimised for excellent image quality.	Constrained to an environment optimised for treatment.
Dominant interaction	Photoelectric absorption, which depends on atomic number of object to the power of 3 to 5.	Compton scatter, which depends on electron density of object. Hence, poorer bone-to-air contrast.
Scatter-to-primary ratio	Lower.	Higher [Jaffray et al. 1994, Swindell and Evans 1996, Spies and Bortfeld 2001, Ozard and Grein 2001]. Scatter adds noise to images.
Main cause of image blur	K-shell fluorescence and transport of optical photons within the scintillator.	Scattered photons and electrons.
Source size	Less than 0.1 mm.	0.5 mm to 3.4 mm [Jaffray et al. 1993]. Hence, decreased resolution and sharpness.
Penetration of source	Lower.	Higher. Hence, decreased detection efficiency.

2.3 The SLIC and the a-Si Technologies

Several EPID technologies have evolved to improve megavoltage imaging during radiotherapy. The SLIC EPID was originally developed at the Netherlands Cancer Institute [van Herk 1991] before being commercialised. A non-optical system, it is compact and glare-free, unlike camera-based systems which impose bulky construction, image spatial distortion and non-uniformity commonly known as "glare" [Heijmen et al. 1995, Partridge et al. 1999]. The frame-rate of the SLIC EPID is, however, less than 1 fps (frame per second), which is too slow for imaging a dynamic multileaf

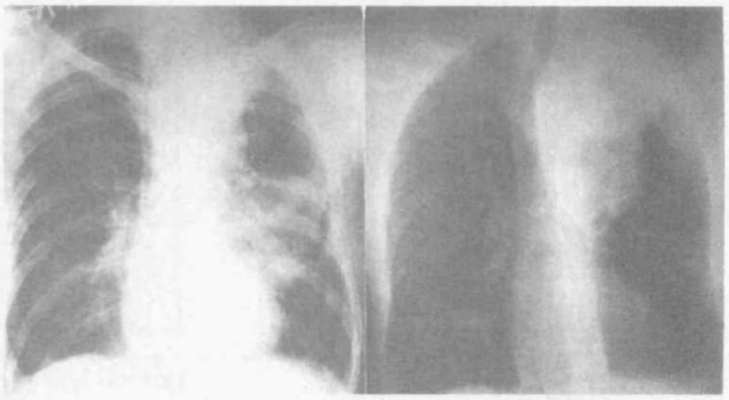

Figure 2.4: Kilovoltage versus megavoltage imaging: chest x rays of the same patient taken on 80 kV (left) and 2 MV (right) x ray machines. Reproduced from Johns and Cunningham [1983].

collimator (DMLC*) beam delivery.

Compared to the SLIC EPID, the a-Si EPID has a higher frame rate (over 3 fps depending on the acquisition mode), a larger detection area (40.0 cm × 30.0 cm) and a higher resolution (0.78 mm). It couples the phosphor scintillator screen with a large-area active matrix readout. The unique technology underlying active matrix flat panel imagers (AMFPIs) is large-area integrated circuits called active-matrix arrays [Antonuk et al. 1997]. The technology allows deposition of semiconductors (e.g. a-Si) across large-area substrates such that physical and electrical properties of the structures can be adapted for a variety of applications.

Stages of radiation detection in the SLIC and the a-Si EPIDs will now be described. Figure 2.6 depicts schematically a typical portal imaging cassette. The *converter* converts the incident radiation into a form detectable by the *detector*. Together these

*DMLC leaves move while the beam is on. Beamlets depicted in Figure 1.2 are delivered continuously without switching off the beam (for rearrangement of leaves).

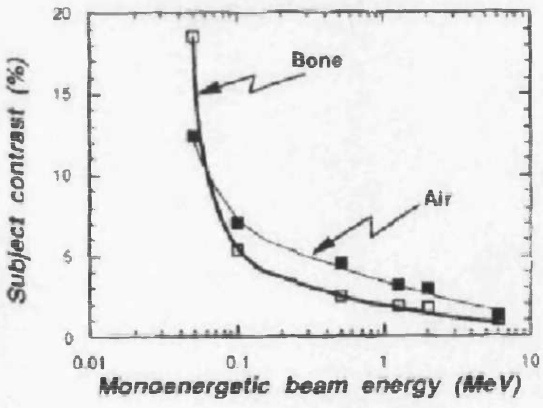

Figure 2.5: Subject contrast for a 1 cm bony structure and a 1 cm air cavity embedded in water. Reproduced from Herman et al. [2001].

two layers form "the heart" of the imager:

- the *converter* may be a metal plate or a combination of a metal plate and a scintillating screen. It stops incident photons so that they may be detected.
  - For the SLIC EPID, the converter is a 1 mm-thick plastoferrite* plate which converts photons into high-energy electrons and screens out low-energy scattered radiation.
  - For the a-Si EPID, the converter is a combination of a copper plate and a phosphor screen: a 1 mm-thick copper plate converts photons into high-energy electrons, at the same time blocking off low-energy scattered radiation; a phosphor scintillating screen† converts electrons into light. The presence of the phosphor improves sensitivity and efficiency [Munro and Bouius 1998].

*The plastoferrite is a compound containing iron and strontium.
†This is a Gd_2O_2S:Tb (gadolinium oxysulphide terbium activated) screen.

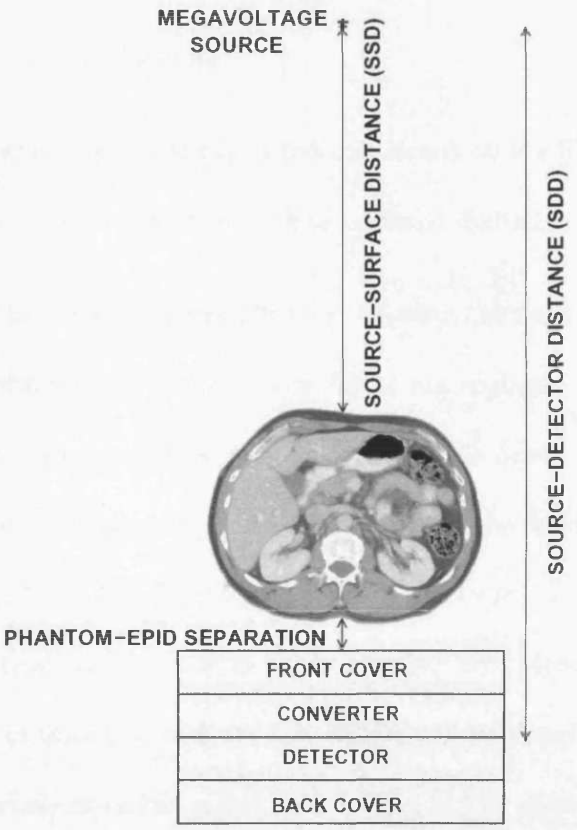

Figure 2.6: Schematic of a generic portal imaging cassette, shown with a megavoltage source irradiating a phantom. Dimensions are not drawn to scale.

- the *detector* is analogous to the piece of film used in traditional portal imaging.
  - For the SLIC EPID, the *detector* is a layer of iso-octane* which serves as the ionising medium for incident electrons. At each pixel, an electrometer converts ionisation into electrical signals.
  - For the a-Si EPID, the *detector* is a glass substrate containing an array of hydrogenated amorphous silicon (a-Si:H) photodiodes and thin film tran-

*The iso-octane is an organic liquid, 2,2,4 trimethylpentane.

sistor (TFT) switches. At each pixel, the photodiode-TFT pair converts light into electrical signals.

Unlike films, where signals are detected and stored on the film itself, detectors in EPIDs detect but do not store – data is stored digitally.

The converter and the detector are sandwiched between the front and the back protective housings. Interleaved between these layers are multiple internal protective layers e.g. foam-like materials, which are not shown in the figure.

Analogous to films, which detect radiation effects in the form of chemical transitions, the SLIC and the a-Si EPIDs detect such effects in the form of ionisation in liquids and electrical conductivity in solids respectively. Monte Carlo studies of radiation transport in the SLIC and the a-Si EPIDs will be presented in Chapter 6.

Practical issues concerning the use of both EPIDs will be discussed in Chapter 7. Some key points here will suffice:

- the liquid thickness in the SLIC EPID varies with cassette orientation, causing the detector response to change with gantry angle;
- unclean discharge and charge trapping in the a-Si EPID cause "ghosting" in subsequent image frames; and
- limitations of acquisition systems e.g. synchronisation with linac pulses and integration of multiple frames complicate radiotherapy verification somewhat.

Chapter 3

MONTE CARLO RADIATION TRANSPORT

Most "experiments" described in this thesis involve computer simulations of stochastic processes in radiation physics – Monte Carlo (MC) radiation transport. Events simulated include transport, interaction and energy deposition of radiation particles in computer representations of the linac, the patient, the electronic portal imaging device (EPID) and the surrounding air. Photons, electrons and positrons were simulated. Since the presence of neutrons is negligible in the energy range of interest (6 MV), they were not simulated. Referring to Figure 1.1, simulation of effects such as chemical changes and biological damage are beyond the scope of this thesis.

3.1 Analog and Non-analog Simulation

The MC technique uses probability distributions of various interactions to simulate the transport, interaction and energy deposition of individual particles in matter. Figure 3.1 steps through the logic behind a typical *analog* transport for a simplified

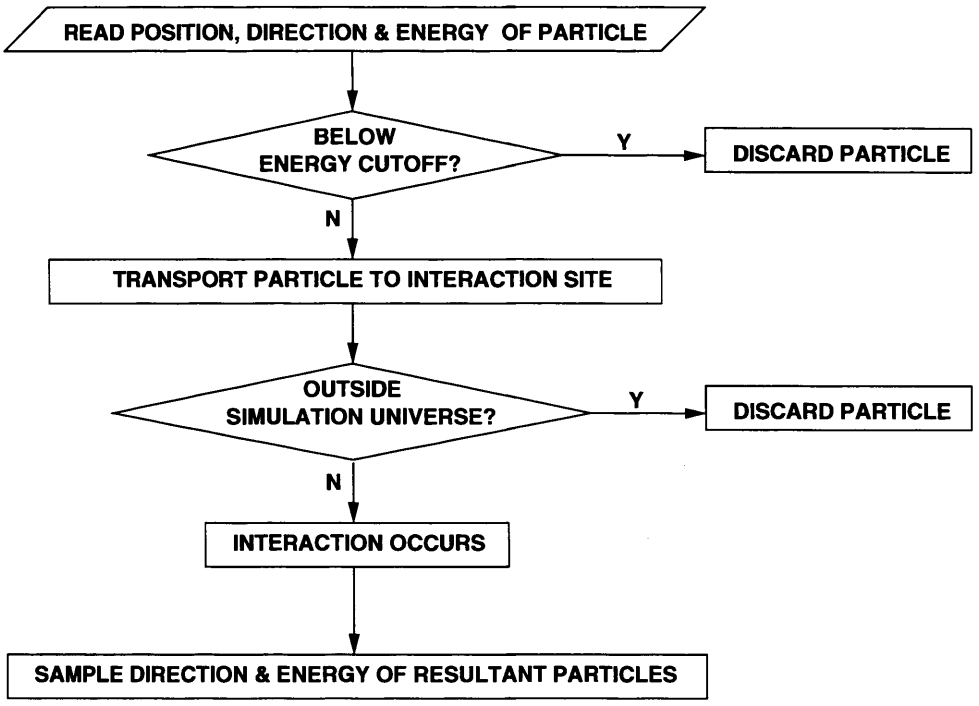

Figure 3.1: Logic in a typical analog transport.

case of a homogeneous single-element geometry. This logic is repeated for all primary and secondary particles. An *analog* transport samples every single event explicitly. Photons are usually simulated this way.

Full step-by-step simulation, however, becomes unrealistic for electrons. There are simply too many interactions. For example, electrons typically undergo 7000 elastic scatterings in slowing down from 500 to 250 keV in gold [Berger and Wang 1988]. To circumvent this difficulty, the cumulative effect of multiple interactions is approximated into a single step. The artificial step length is often chosen to be many mean free paths. This is known as the *condensed history* technique.

An implementation of condensed history for charged particles is shown in Fig-

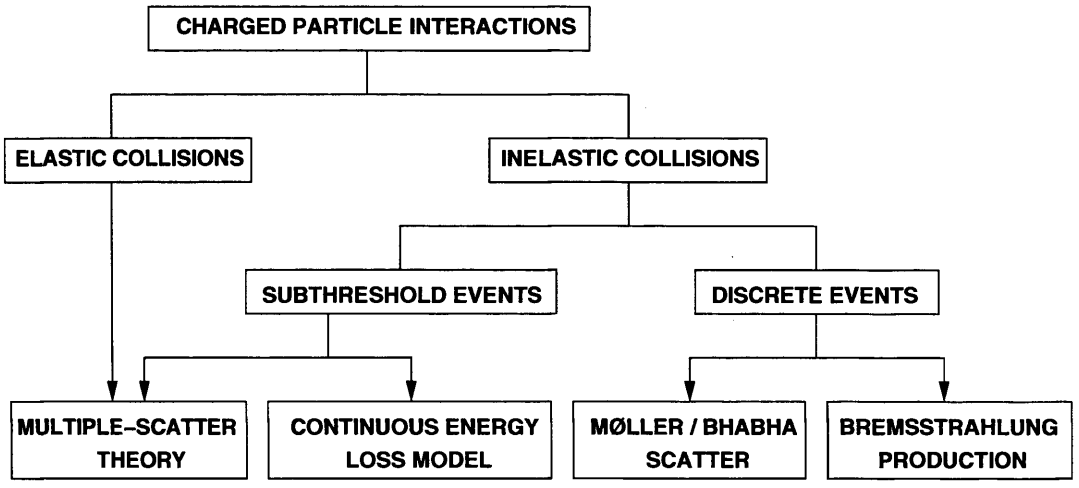

Figure 3.2: An implementation of condensed history for charged particle transport.

ure 3.2*. Elastic collisions are treated using multiple-scatter theories [Kawrakow 2000a, Moliere 1948, Goudsmit and Saunderson 1940]. Inelastic collisions are divided into two groups according to the threshold energy: subthreshold inelastic collisions are treated using continuous energy loss models (for energy loss) and multiple-scatter theories (for angular deflection); above-threshold inelastic events are simulated explicitly event-by-event. The condensed history technique fits into a modified transport logic (Figure 3.3) different from that shown in Figure 3.1. Non-analog simulations such as these, when properly implemented and applied, should not cause any bias in simulation outcome.

*This is the implementation for EGS; implementation in MCNP differs.

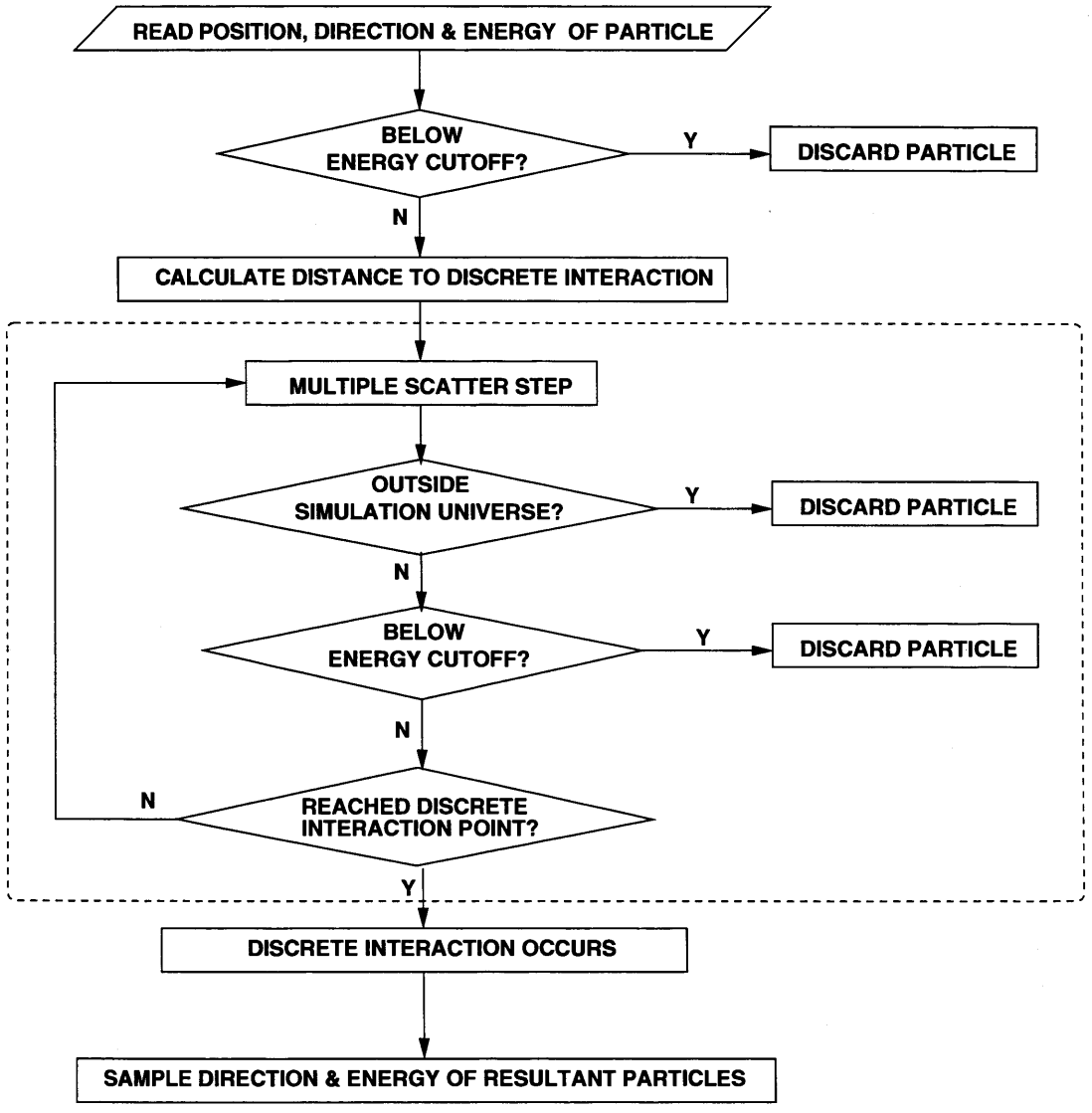

Figure 3.3: Logic in electron transport. Dashed box outlines the difference from Figure 3.1.

3.2 Why Monte Carlo?

As will be demonstrated in later chapters, MC simulation of radiation transport is tremendously powerful:

- it is more accurate than deterministic or analytical calculations particularly under conditions of electronic disequilibrium, mainly due to the complexity of electron transport;
- it allows *tally** placement in areas not accessible by physical measurements, e.g. a point inside a patient's spinal cord;
- it provides information not extractable from physical measurements, e.g. the fraction of particles originating from Compton scatter within a particular region of interest;
- it provides a "virtual" experimental platform not available otherwise, e.g. trial-and-error iterations of various beam configurations on a "virtual patient";
- it facilitates detailed understanding of radiation physics e.g. stages of radiation detection in a detector.

3.3 Choice of Codes

MC code systems are complex. They require substantial development and benchmarking efforts. Large user-bases contribute towards more error-reporting and hence

*The *tally* is a quantitative outcome requested by the user from the MC simulation, e.g. dose in a specific region.

improve code integrity. Established MC code systems include EGS (Electron Gamma Shower) developed by the Stanford Linear Accelerator Center and the National Research Council of Canada [Nelson et al. 1985, Kawrakow 2000a], and MCNP (Monte Carlo N-Particle) by Los Alamos National Laboratory [Briesmeister 1986, 1993]. Each evolves incrementally through code versions, for improved physics and sometimes for wider compatibility (e.g. executable on desktop Windows machines or capable of built-in parallel processing).

MC code systems differ in certain aspects and features such as:

- sampling algorithms, e.g. the new EGS version, EGSnrc [Kawrakow 2000a], has been shown to achieve unprecedented accuracy in electron transport [Kawrakow 2000b];

- implementation of condensed history, e.g. EGS simulates bremsstrahlung processes above a certain energy threshold but MCNP does not;

- particle types simulated, e.g. MCNP simulates neutrons but EGS does not;

- *variance reduction techniques** [Briesmeister 1986, Kawrakow et al. 2004] available, e.g. MCNP offers a wider range of techniques;

- statistical analysis tools available, e.g. MCNP has its *ten statistical tests* whereas EGS only computes the standard error; and

* *Variance reduction techniques* increase simulation efficiency by modifying the conventional random walk sampling, e.g. by preferentially sampling particles that would be more likely to eventually contribute to the *tally*.

- user-base for specific applications, e.g. EGSnrc has the wider radiotherapy user-base.

3.4 EGSnrc, BEAMnrc and DOSXYZnrc

For accuracy in electron transport and applicability to radiotherapy problems, the EGSnrc code system was chosen for the work in this thesis. EGSnrc takes into account the following photon, electron and atomic processes:

- pair production (triplet production is not simulated explicitly but is taken into account using a combined pair-and-triplet cross section compiled by Storm and Israel [1970])*;
- Compton scatter, with options for Klein-Nishina (which assumes electrons to be free) or bound Compton [Johns and Cunningham 1983];
- photoelectric effect;
- Rayleigh scattering, if requested;
- Bremsstrahlung production;
- Møller and Bhabha scattering;
- positron annihilation in flight and at rest;

*In a pair production, the photon interacts with the **Coulomb field of the nucleus** and is absorbed; an electron-positron pair is created. In a triplet production, the photon interacts with the **field of an atomic electron** which receives sufficient energy to be set free.

- multiple scattering of charged particles by Coulomb scattering from nuclei [Kawrakow 2000a];

- collision energy loss determined by the restricted Bethe-Bloch stopping powers with Sternheimer treatment of density effects;

- relaxation of excited atoms following vacancies (due to photoelectric or Compton events), if requested, producing K, L and M shell fluorescent photons, Auger and Coster-Kronig electrons.

EGSnrc, and its radiotherapy-related derivatives BEAMnrc [Rogers et al. 2001] and DOSXYZnrc [Walters and Rogers 2002] were used in various parts of this thesis:

- EGSnrc requires extensive programming but offers greatest flexibility. For instance, particle-labelling (to track information through generations of secondary particles) and *tallies* may be placed at any point in the logic shown in Figure 3.1 and Figure 3.3. EGSnrc was used in detailed investigations such as detector studies (Chapter 6).

- BEAMnrc is a specialised code for modelling of linear accelerators (linacs). It contains a library of component modules (CMs) such as the *flattening filter** and the collimators. The user assembles the geometry by selecting the appropriate components and specifying the dimensions. BEAMnrc was used in simulation of radiotherapy sources (Chapter 4).

*In the megavoltage range, the bremsstrahlung photon beam is peaked in the forward direction. A *flattening filter* is inserted in the beam to make the intensity uniform across the beam.

- DOSXYZnrc is a specialised code for *tallying* dose deposition in a rectilinear voxel geometry. When detailed representation of the inhomogeneous patient body is required, it is capable of importing voxel-by-voxel material and density data from CT scans. DOSXYZnrc was used for dose calculation in phantoms and detectors (Chapter 5). TWIZ&GLU, a pre-processor designed and implemented by the author, extended the usability of DOSXYZnrc for portal dose computation of oblique beams [Chin et al. 2003].

Chapter 4

SIMULATION OF LINAC SOURCES

Accurate Monte Carlo (MC) simulation of clinical beams is essential for providing a realistic representation of radiotherapy sources for dose calculations. At Velindre Cancer Centre, production of photon beams from the medical linear accelerator (linac) has previously been simulated using an earlier BEAM version, BEAM00 [Rogers et al. 2000]. This chapter reports simulation of linac photon beams using the recent version, BEAMnrc [Rogers et al. 2001], which incorporates improved physics and statistical estimation.

The range of field sizes simulated was broader than that previously available. Output from this chapter equips our data library with computer representations of linac photon beams, which can be readily deployed in further simulations (e.g. simulations in the next chapter) so that the same linac need not be simulated repeatedly.

This chapter also covers investigations on transport options, *variance reduction techniques** and statistical uncertainties – all of which are of great scientific interest.

* *Variance reduction techniques* have been introduced in Section 3.3.

4.1 Introduction

As introduced in Section 3.4, BEAM is a specialised MC code for linac modelling. It is built on EGS, which has evolved incrementally through code versions. EGSnrc is the version used for this thesis except in Section 4.2.1 where, for comparison purposes, an earlier version was also used. EGSnrc is the first MC code to pass the most stringent benchmark tests, by successfully simulating ion chamber response and backscatter artefact-free [Kawrakow 2000b]. Since the new features of EGSnrc have been incorporated in BEAMnrc but not BEAM00, BEAMnrc is understood to be more accurate in radiation transport physics. Additionally, as will be explained in Section 4.2.5, an improved statistical estimation in BEAMnrc accounts for the correlation between secondary particles originating from the same source particle [Walters et al. 2002]. We have therefore simulated our linac photon beams using BEAMnrc and recommissioned our phase space library.

Whereas clinical beams are sometimes MC-simulated "one-off" for generating kernel libraries required in convolution/superposition methods, there are growing interests in using the output for subsequent case-by-case, patient-dependent MC simulations. MC simulation of clinical beams has been reported by various groups and has been extensively reviewed (see Verhaegen and Seuntjens [2003] and references therein). Most reports, however, deal with a limited range of field sizes, or lack rigorous analysis of deviation from measured data. To our knowledge, none have reported effects of the improved EGSnrc transport physics on linac beam simulation.

In this work, we explored different transport configurations in the simulation of

a Varian linac. A fine-tuned model of the 6 MV photon beam was found to produce good agreement with measured beam data for 6 tested field sizes ranging from 2 cm × 2 cm to 25 cm × 25 cm.

Section 4.3.5 reports some interesting and unexpected effects on statistical uncertainty when simulating an increasing number of particles. Step-by-step investigations to trace the cause will be presented, along with a new method for validating that a *phase space file** is an adequately representative sample of a beam.

4.2 Materials & Methods

BEAM00, BEAMnrc and DOSXYZnrc were used for simulations in this chapter:

- a Varian Clinac 2100CD linac was simulated using BEAM00 (Section 4.2.1) and BEAMnrc (Section 4.2.1, Section 4.2.2, Section 4.2.3, Section 4.2.4);
- dose deposition in a water phantom was simulated using DOSXYZnrc (Section 4.2.3, Section 4.2.4 and Section 4.2.5).

Table 4.1 gives a general description of the above simulations according to the framework, "How Monte Carlo simulations work" given in Figure 1.4.

*To avoid repeated simulations of the same linac, a *phase space file* is often stored to be used as the radiation source in subsequent dosimetric simulations. It contains data for many particles: one record for each particle crossing a user-specified plane (Figure 4.1). Each record contains the position, direction, energy and statistical weight for one particle.

Table 4.1: Description of simulations performed in this chapter.

	BEAM00/BEAMnrc	**DOSXYZnrc**
Geometry	A computer representation of the linac was constructed by assembling various linac components e.g. the target, the flattening filter[a] and the jaws according to compositions and dimensions provided by the manufacturer[b] (Figure 4.1). The same linac model was used throughout the chapter except in Section 4.2.4, where the opening of the jaws was varied to provide the desired range of field sizes.	A computer representation of a water phantom was constructed as a 3D lattice of voxels (Figure 4.2).
Source	A parallel beam of monoenergetic electrons impinging on the linac target, a tungsten-copper composite (Figure 4.1). In Section 4.2.3, the energy and the radius of this electron source were varied to obtain the best agreement between simulation results and measured beam data.	A phase space file produced from BEAMnrc simulations.
Transport	Transports using BEAM00 and BEAMnrc were compared in Section 4.2.1. For BEAMnrc, an optimised set of transport options was determined in Section 4.2.2 and was used in all subsequent simulations in the chapter.	DOSXYZnrc default transport options were used.
Output	A phase space file.	Dose deposition in each voxel in the 3D lattice.

[a]The *flattening filter* has been introduced in Section 3.4.

[b]Exact details cannot be provided here due to confidential agreements with the manufacturer.

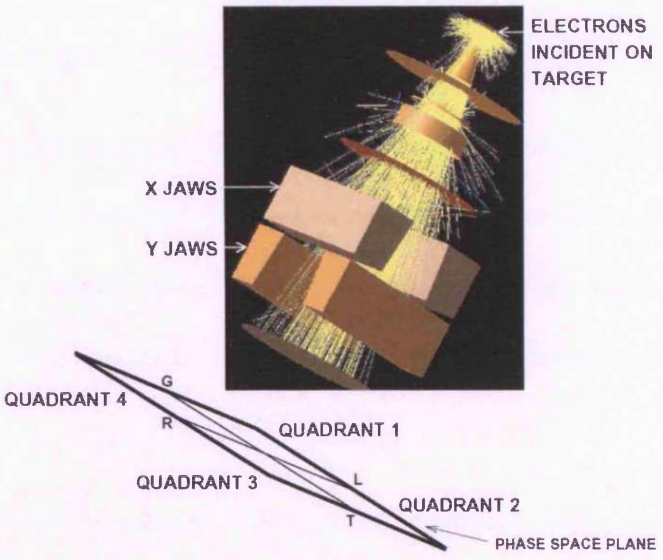

Figure 4.1: BEAMnrc simulation of a linac, where a *pencil beam* of electrons impinges on the linac target. The phase space plane is defined downstream from the linac. Location of X and Y jaw pairs at different levels causes asymmetry in the GT ("Gun-Target", also known as *inplane*) and LR ("Left-Right", also known as *crossplane*) directions on the phase space plane. Particle tracks are also shown.

4.2.1 Migration from BEAM00 to BEAMnrc

To see whether BEAM00 and BEAMnrc produce the same output when the same linac model (geometry) is simulated, simulations were run using the two codes. The phase space files produced were analysed for photon fluence.

4.2.2 Selection of Transport Options

BEAMnrc was used in all sections that follow. For selecting an optimised set of transport options, 3 transport configurations were considered:

- configuration A: detailed transport, henceforth referred to as "first-class" transport, understood to produce unprecedented accuracy, made possible by the re-

lease of EGSnrc. No variance reduction techniques were used. This served as the reference against which other configurations were compared.

- configuration B: transport using BEAMnrc default settings. No variance reduction techniques were used. Investigation of this configuration was to indicate the necessity for caution when adopting the default settings "off-the-shelf". These default settings would be in effect whenever the settings were not explicitly specified.

- configuration C: transport with variance reduction. *Bremsstrahlung splitting*[*] and *Russian roulette*[†] were used to increase simulation *efficiency*. In this context, *efficiency* measures the number of phase space particles produced within a given simulation time, rather than the conventional history-per-time gauge.

Settings of transport options are given in Table 4.2. Details on the transport options and variance reduction techniques used are given in the literature [Kawrakow and Rogers 2002, Kawrakow 2000a]. In all three configurations, a 6.0 MeV electron source of radius 1.0 mm was simulated. Jaw settings were modelled for a 5 cm $\times$ 5 cm field[‡].

Output from all three configurations was tested individually for:

[*] *Bremsstrahlung splitting* is a variance reduction technique where a bremsstrahlung event produces X photons, each with $1/X$ statistical weight, instead of a single photon with unity statistical weight. This is to improve the statistics of bremsstrahlung photons.

[†] *Russian roulette* is a variance reduction technique which imposes a survival threshold on secondary charged particles from photons generated by bremsstrahlung splitting. Depending on the random number generated for each charged particle and the survival threshold, the particle either survives the roulette or is eliminated.

[‡] All field sizes in this thesis are defined at the level of the isocentre, which, for the installations used in this work, is 100.0 cm away from the source and 124.5 cm above the floor. The isocentre is the point where the central axis of all beams intersect when the gantry is rotated.

Table 4.2: Configurations A, B and C for BEAMnrc simulation of linac sources.

	A	B	C
Boundary crossing algorithm[a]	EXACT	PRESTA-I	EXACT
Electron-step algorithm	PRESTA-II	PRESTA-II	PRESTA-II
Spin effects	On	On	On
Photoelectron angular sampling[b]	On	Off	On
Bound Compton scattering	On	Off	On
Atomic relaxations	On	Off	On
Electron cutoff (MeV including rest-mass)	0.521	0.521	0.700
Uniform bremsstrahlung splitting	0	0	500
Russian roulette	Off	Off	On

[a]'EXACT' switches into single elastic scattering mode near boundaries.
[b]Sauter's formula if 'On' [Sauter 1931].

- photon energy fluence and energy spectrum on the phase space plane; and

- dose deposition in a water phantom simulated using DOSXYZnrc, where the phase space output from the BEAMnrc simulation served as the radiation source.

4.2.3 Fine-tuning the Linac Model

The initial model of 6.0 MeV electron *pencil beam* with a 1.0 mm source radius was further fine-tuned for better agreement with dose characteristics in a water phantom. In the fine-tuning process, the incident electron energy was varied from 5.85 MeV to 6.10 MeV; the source radius was varied from 0.5 mm to 2.5 mm. A 5 cm $\times$ 5 cm field was chosen for the fine-tuning process since smaller fields were found to be more sensitive to variations in incident electron energy and source dimension. Moreover, smaller field sizes are of greater interest since they are commonly used for high-precision radiotherapy.

Dose deposition in a water phantom was simulated using DOSXYZnrc, where phase space output from the BEAMnrc simulation served as the radiation source. The in-phantom depth doses and radiation profiles were compared against measured beam data obtained during linac commissioning*. The source model producing the best agreement with measured beam data was chosen to be the fine-tuned model.

4.2.4 Modelling Varying Field Sizes

By changing the jaw positions in the linac model, square fields of varying dimensions were simulated: 2 cm, 5 cm, 10 cm, 15 cm, 20 cm and 25 cm.† For each field size, dose deposition in a 50 cm × 50 cm × 50 cm water tank, simulated using DOSXYZnrc, was compared against measured beam data obtained during linac commissioning.

For dose deposition in a water tank, 3.0 cm × 0.2 cm voxels of varying thicknesses were defined along the central axis (Figure 4.2). The thickness was 0.2 cm for the first 5.0 cm depth, and 1.0 cm for further depths. This was used for all incident field sizes except field size 2 cm × 2 cm, where 1.0 cm × 0.2 cm voxels were used instead of 3.0 cm × 0.2 cm.

Simulation output for dose deposition is in units of *Gray per incident radiation history*, usually of the order of 10^{-17}. Measured beam data is obtained in percentage terms, relative to the maximum reading (for depth doses), or to the central axis reading (for transverse radiation profiles). Normalisation is therefore required before

*An ion chamber was used for measuring depth doses; a diode was used for measuring transverse profiles.

†For portal dosimetry (the topic of this thesis), 25 cm × 25 cm is the maximum field of interest. It is the maximum allowable field when the EPID is positioned at 130 cm from the source; the maximum allowable field is even smaller when the EPID is further away from the source.

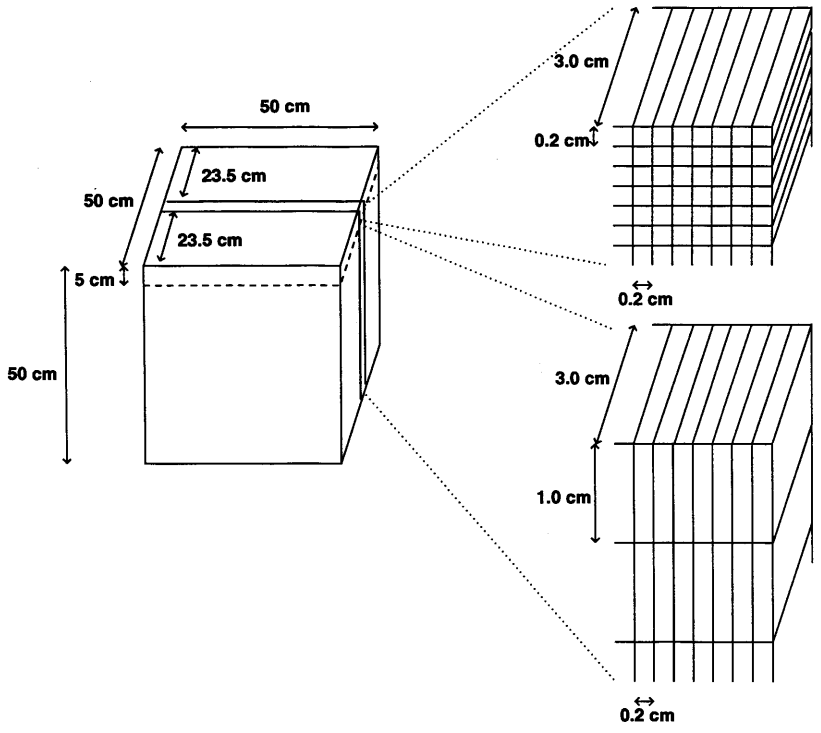

Figure 4.2: Voxel geometry used for tallying dose deposition in a 50 cm × 50 cm × 50 cm water tank: 3.0 cm × 0.2 cm voxels of varying thicknesses were defined as shown. The thickness was 0.2 cm for the first 5.0 cm depth, and 1.0 cm for further depths.

simulation results may be compared against measured data. Figure 4.3 explains each step in the normalisation procedure. Normalised in this way, radiation profiles would have depth dose data included implicitly. Explicit plotting of depth dose curves for comparing the two datasets would therefore not be necessary.

4.2.5 Use of Phase Space Particles

In using phase space files to provide source particles for subsequent simulations e.g. portal image prediction (Chapter 5), there are two sources of uncertainty in the subsequent simulations:

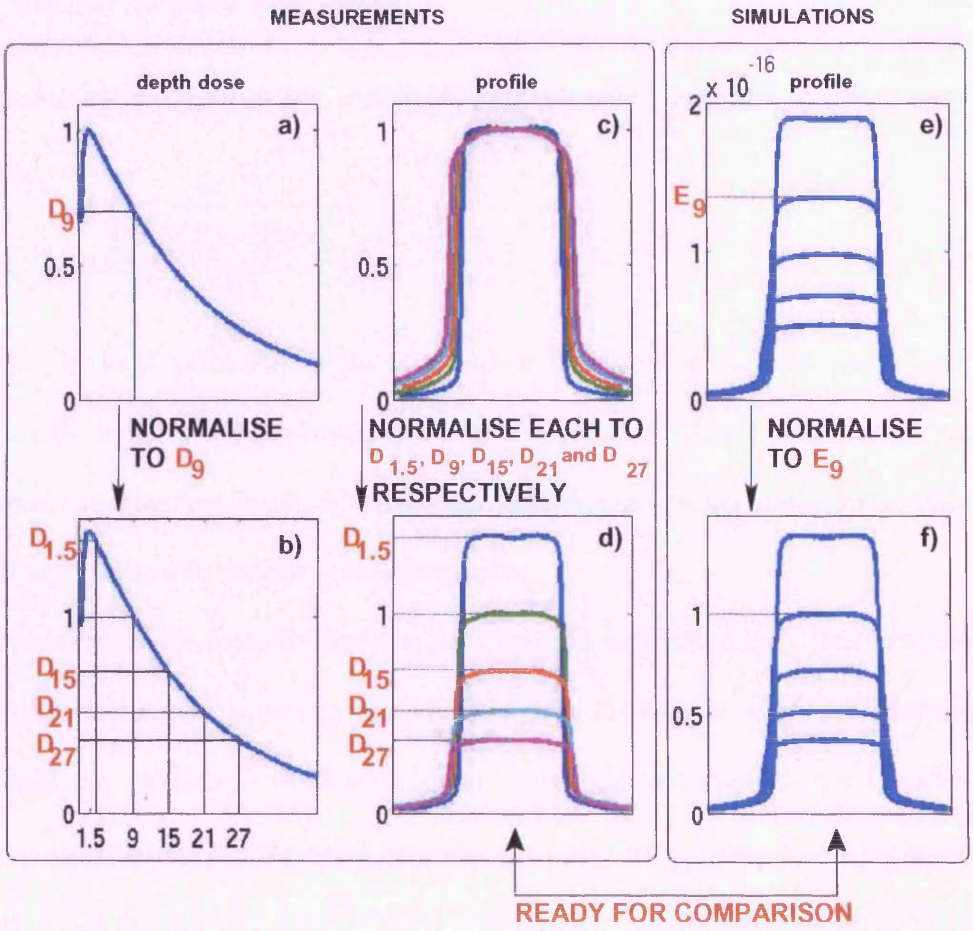

Figure 4.3: Schematic diagram of the normalisation procedure for comparing measured beam data with MC simulation results. From **a** to **b**: normalising the measured depth dose curve to the relative dose value D_9, which is the vertical-axis value at depth 9.0 cm. From **b**: deriving $D_{1.5}$, D_{15}, D_{21} and D_{27}, which are the relative dose values corresponding to depths (horizontal axis) 1.5 cm, 15 cm, 21 cm and 27 cm respectively. From **c** to **d**: normalising the profiles measured at depths 1.5 cm, 15 cm, 21 cm and 27 cm, each to its corresponding value of $D_{1.5}$, D_{15}, D_{21} or D_{27} respectively. From **e** to **f**: normalising the simulated profile to E_9, which is the vertical-axis value on the central beam axis at depth 9.0 cm.

- that due to the random nature of transport in the phantom, detector and air;

- that due to statistical fluctuation, termed *latent variance* by Sempau et al. [2001], in the phase space source.

Uncertainty for the quantity scored (X) was calculated using the standard error formula:

$$s_{\overline{X}} = \sqrt{\frac{\sum_{i=1}^{N}(X_i - \overline{X})^2}{N(N-1)}} \tag{4.1}$$

where X_i is the X value for the ith *independent history*, $\overline{X}$ is the mean value of X and N is the number of *independent histories* [Walters et al. 2002]. Here, the author emphasises *independent histories* because the definition of a *history* requires caution, as will be explained in the next two paragraphs.

A phase space file typically contains data for millions of particles*. However, not all particles constitute an *independent history.* This is because some particles are correlated, e.g. secondaries originating from the same electron impinging on the linac target. To account for correlation between such particles, uncertainty estimation should regard the correlating particles as belonging to the same *independent history.*

The number of phase space particles (serving as incident source) required for a particular simulation depends on the geometry setup, volume of the tally and the desired level of (un)certainty. Since terabytes† of phase space files are impractical under normal circumstances, particles in a phase space file are sometimes reused in order to achieve a smaller uncertainty, $s_{\overline{X}}$. Each time a particle is reused, it would

*Every gigabyte contains data for 30 million particles.
†1 terabyte = 10^{12} bytes = 10^3 gigabytes.

have the same initial position, energy and direction – but tracks a different trajectory due to random sampling of transport and interaction. Whenever a particle is reused, all tracks should be regarded as belonging to the same *independent history* [Walters et al. 2002]. This is to avoid any underestimation of uncertainties, so that when particles are heavily reused, the calculated uncertainty would not approach zero, but a finite value which reflects the *latent variance* [Sempau et al. 2001] of the phase space source. In BEAMnrc nomenclature, reusing particles by accounting for such correlation is called *recycling*; whereas reusing without accounting for such correlation is called *restarting* – which should generally be avoided.

The author has modified and recompiled the original DOSXYZnrc code so that the code automatically calculates the number of histories according to the desired number of recycles. This modification eliminates:

- potential undersampling of a phase space file; and

- accidental restarts

which happen e.g. when the number of histories requested by the user is not exact multiples of the number of particles in the phase space file.

This section sets out to investigate the effects on the tally (T) and the corresponding uncertainty (U) when 1) increasing number of phase space particles are used; and when 2) phase space particles are recycled. The irradiation setup was a beam incident on a scanning liquid ionisation chamber (SLIC) electronic portal imager (EPID)

positioned at *SDD** 140 cm. On the central axis, in the *active detection layer*†, a voxel of area 1.6 cm × 1.6 cm was defined as the tally.

The phase space for a 15 cm × 15 cm field produced in Section 4.2.4 (where the variance reduction techniques bremsstrahlung splitting and Russian roulette were exercised) was used as the incident beam. Simulations were performed for varying 1) N, phase space particles, ranging from 8 million to 255 million; and 2) R, repeat cycles, ranging from 0 to 128.

Investigation of the variation of T and U as a function of R was repeated: 1) without simulating charged particles from the phase space file; 2) with a phase space file regenerated without bremsstrahlung splitting; and 3) with a phase space file regenerated with bremsstrahlung splitting but without Russian roulette.

4.3 Results & Discussion

4.3.1 Migration from BEAM00 to BEAMnrc

Photon fluence produced with BEAM00 was found to differ from that produced with BEAMnrc by more than 5% (Figure 4.4). This suggests the need for recommissioning MC linac models when migrating to BEAMnrc. It, however, does not imply that previous simulations using BEAM00 were wrong – since the difference would have been accounted for in the model-tuning and calibration processes.

---

*The *SDD* has been defined in Figure 2.6.

†The *active detection layer* is the layer containing iso-octane, which has been introduced in Section 2.3.

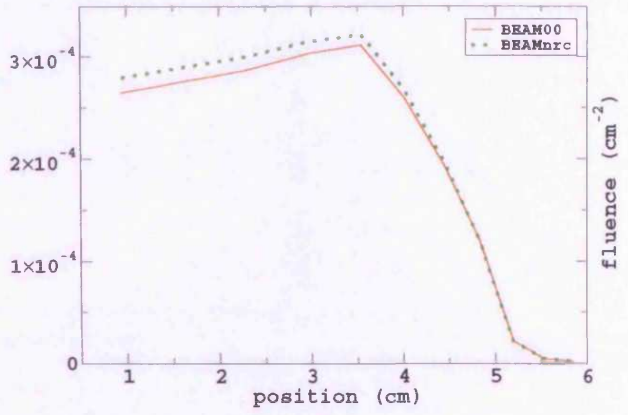

Figure 4.4: BEAM00 vs. BEAMnrc: fluence of phase space particles.

4.3.2 Selection of Transport Options

For BEAMnrc simulation of the linac and with the terminology defined in Section 4.2.2, configuration B (default) was found to differ significantly from configuration A (*first-class*). Configuration B over-estimated the energy fluence by 4%. It also over-estimated the energy spectrum by 7% at the peak (Figure 4.5). Configuration C (optimised) produced phase space characteristics in good agreement with configuration A (Figure 4.5), while increasing the efficiency over 200 times. Configuration C was therefore adopted for subsequent simulations in the sections which follow.

Furthermore, it was suspected that the difference between configurations A and B would diminish when each of the energy fluence and energy spectrum curves were normalised to its own central axis value. In that case, the difference would have been corrected by appropriate calibration for subsequent applications. *Self-normalisation* was thus carried out, as shown in the bottom panel of Figure 4.5. The difference

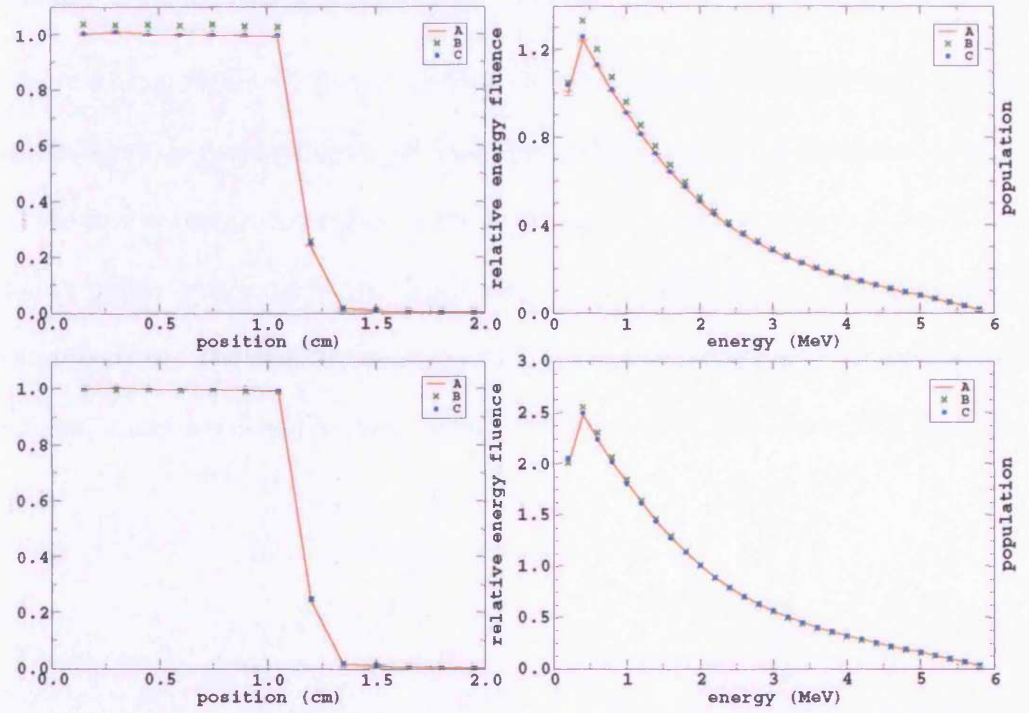

Figure 4.5: Energy fluence (left) and energy spectrum (right) of phase space particles scored for configurations A, B and C. Plots before (top) and after (bottom) self-normalisation are shown.

between configurations A and B was found to be smaller but remained significant by 3% at the peak of the energy spectrum.

From DOSXYZnrc simulations of dose deposition in a water phantom, however, radiation profiles exhibited no noticeable difference. This observation proves that direct analysis of phase space particles (e.g. fluence and spectrum, as done in this work) is a more sensitive test than dose deposition in a water phantom, which has been the reference conventionally adopted by the radiotherapy community.

4.3.3 Fine-tuning the Linac Model

Figure 4.6 and Figure 4.7 show the effects of varying source energy and source radius on the depth dose and radiation profile respectively. The depth dose is more sensitive to the source energy, compared to the profile. The profile is more sensitive to the source radius, compared to the depth dose, as one would expect from geometrical considerations. The smaller the source radius, the sharper the field penumbra. The optimal model was found to be a 1.0 mm radius parallel beam of 6.0 MeV electrons.

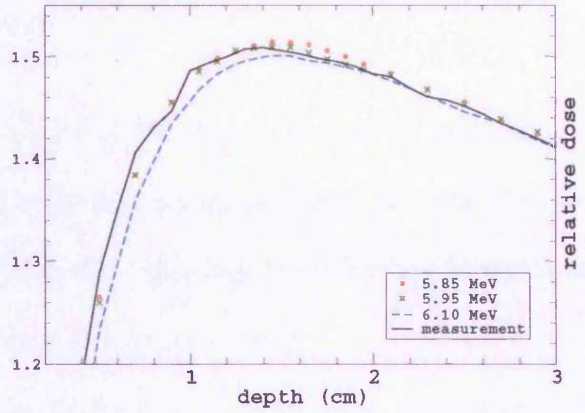

Figure 4.6: Influence of the incident electron energy on the water phantom depth dose. Data shown is from a simulation of a 5 cm × 5 cm field with 1.5 mm source radius.

4.3.4 Modelling Varying Field Sizes

For square field sizes of side 2 cm, 5 cm, 10 cm, 15 cm, 20 cm and 25 cm, depth doses and profiles of various field sizes were found to be in good agreement with measured beam data (Figure 4.8 to Figure 4.13). Except in regions of high dose gradient within the penumbra, differences between simulation results and measured

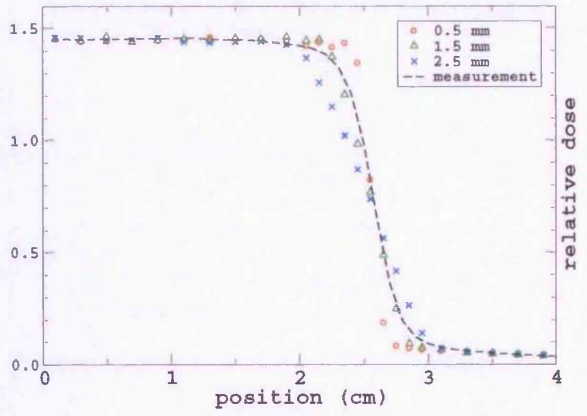

Figure 4.7: Influence of the radius of electron source on the radiation profile at 2.5 cm depth in water. Data shown is from a simulation of a 5 cm × 5 cm field with 5.95 MeV incident electron energy.

data were well within 2% of the central axis value of each radiation profile. Gamma analysis (explained in the next paragraph) found over 80% of all points fulfilling a 3%-or-3 mm criterion. Therefore, the single fine-tuned model was found to be universally applicable to the range of field sizes tested.

The gamma analysis [Low et al. 1998] unifies dose distribution comparisons of measured and calculated dose distributions. The measure of acceptability is the difference between the measurement and calculation points in both the dose and the physical distance, scaled as a fraction of the acceptance criterion.

4.3.5 Use of Phase Space Particles

Surprisingly, increasing R did not monotonically decrease the uncertainty. Figure 4.14a shows occurrences of such anomalies. The anomalies persisted even when the experiment was repeated with a much higher number (255 million) of phase space

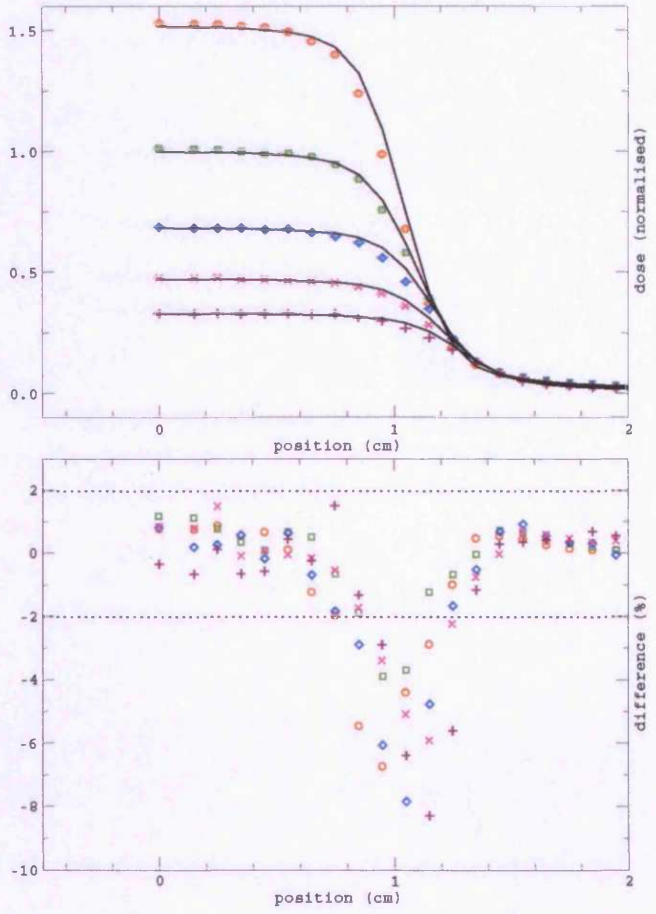

Figure 4.8: Dose profiles in a water tank for a 2 cm × 2 cm beam: measured beam data (lines) and MC simulation results (symbols).

particles* (Figure 4.14b). For all graphs presented under this section, T has been normalised to T_m, which is the value of T when N = 255 million and R = 128, which are maxima of the tested range.

The top left panel of Figure 4.15 shows the variation in T as a function of R and N. The bottom left panel displays the same data, but with a binary pass-fail criterion. The criterion was whether T differed from T_m above (exclusive) or below (inclusive)

*A phase space file containing 255 million particles occupies 8 gigabytes of disk space.

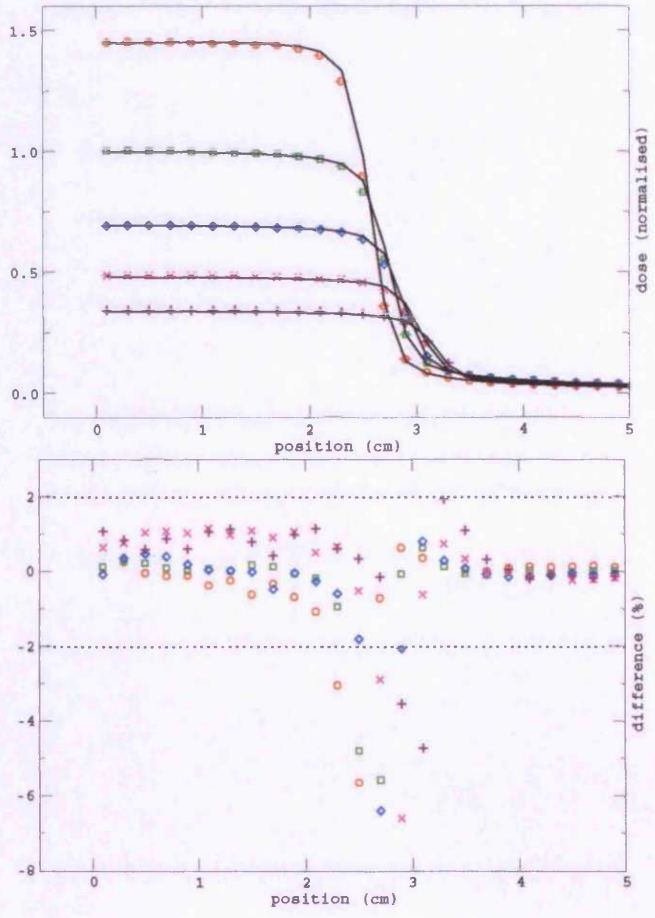

Figure 4.9: Dose profiles in a water tank for a 5 cm × 5 cm beam: measured beam data (lines) and MC simulation results (symbols).

the 0.5% threshold. The top right panel of Figure 4.15 shows the variation in U as a function of both R and N. The bottom right panel displays the same data, but with a binary pass-fail criterion. The criterion was whether U was over (exclusive) or under (inclusive) 0.5%.

In both vertical (R) and horizontal (N) directions, Figure 4.15 shows repeated occurrences of the anomalies. Although the bottom right corners (corresponding to high N and high R) of the 4 maps demonstrated a majority passing the pass-fail

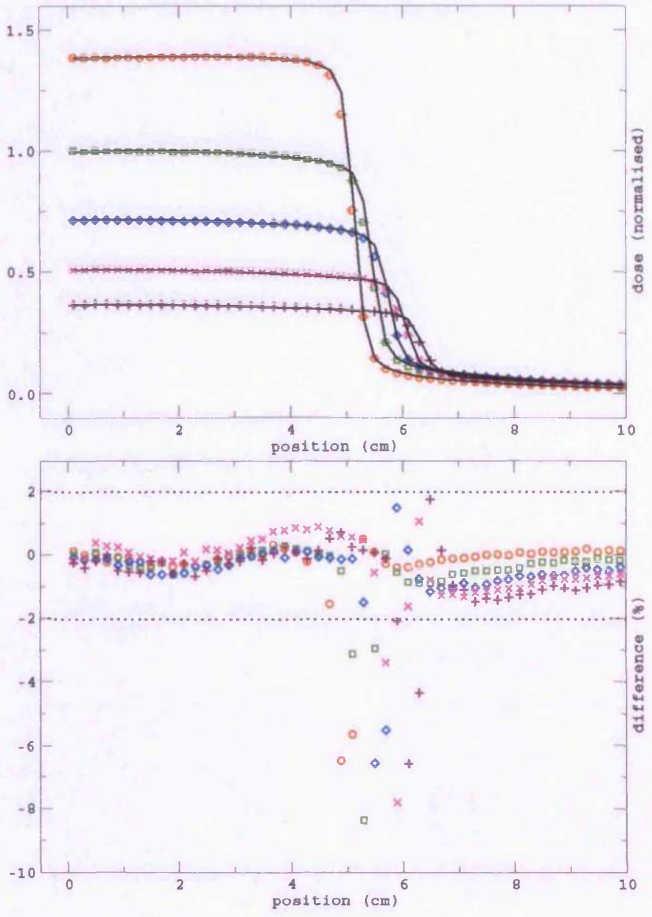

Figure 4.10: Dose profiles in a water tank for a 10 cm × 10 cm beam: measured beam data (lines) and MC simulation results (symbols).

criterion, fluctuations persisted. From the 4 maps, it is difficult to judge how large N and R should be, to be considered adequate for a particular calculation since the trend is not completely predictable. In theory, increasing R should decrease the numerator while maintaining the denominator in Equation (4.1); increasing N should increase the denominator in the same equation. Therefore, in statistical terms, provided the sample is representative of the population, increasing R and N should each 1) stabilise T; and 2) decrease U. The anomalies, therefore, required further investigation.

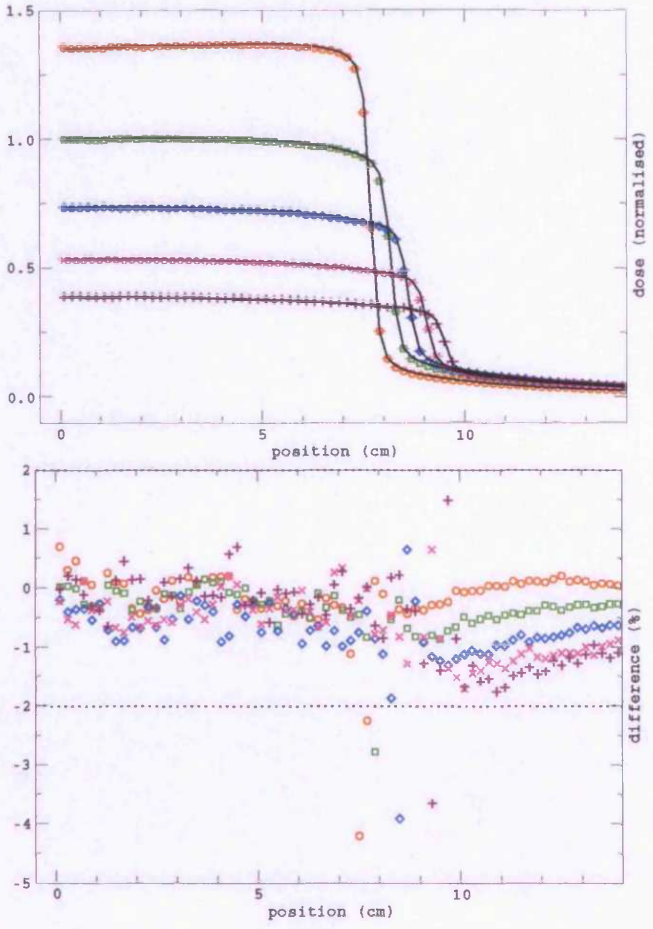

Figure 4.11: Dose profiles in a water tank for a 15 cm × 15 cm beam: measured beam data (lines) and MC simulation results (symbols).

When the experiment was repeated without simulating charged particles from the phase space file, the uncertainty decreased monotonically with increasing number of recycles (Figure 4.16a). In other words, the anomalies disappeared.

This led to the suspicion that the phase space file used somehow contained an inadequate representation of electrons. This prompted regeneration of a phase space file without using bremsstrahlung splitting. With the regenerated phase space file,

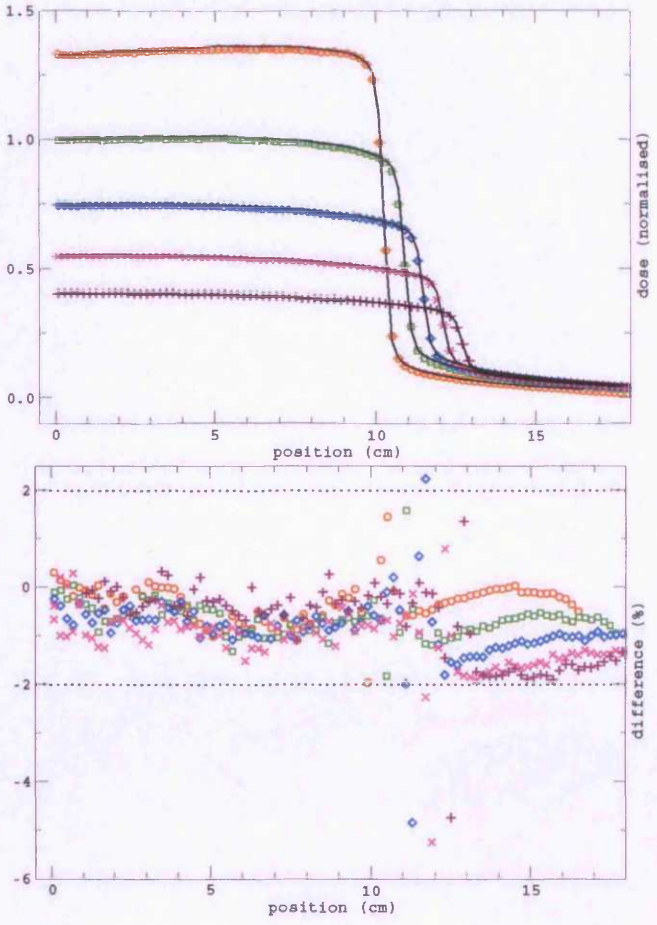

Figure 4.12: Dose profiles in a water tank for a 20 cm × 20 cm beam: measured beam data (lines) and MC simulation results (symbols).

repetition of the experiment showed monotonic decrease of U with increasing number of R, i.e. the anomalies disappeared (Figure 4.16b). The anomalies also disappeared in a further test using a phase space file regenerated using bremsstrahlung splitting but without Russian roulette (Figure 4.16c).

Additionally, it can be observed from Figure 4.16 that when bremsstrahlung splitting was used, U decreased slower with increasing R – which is expected since variance

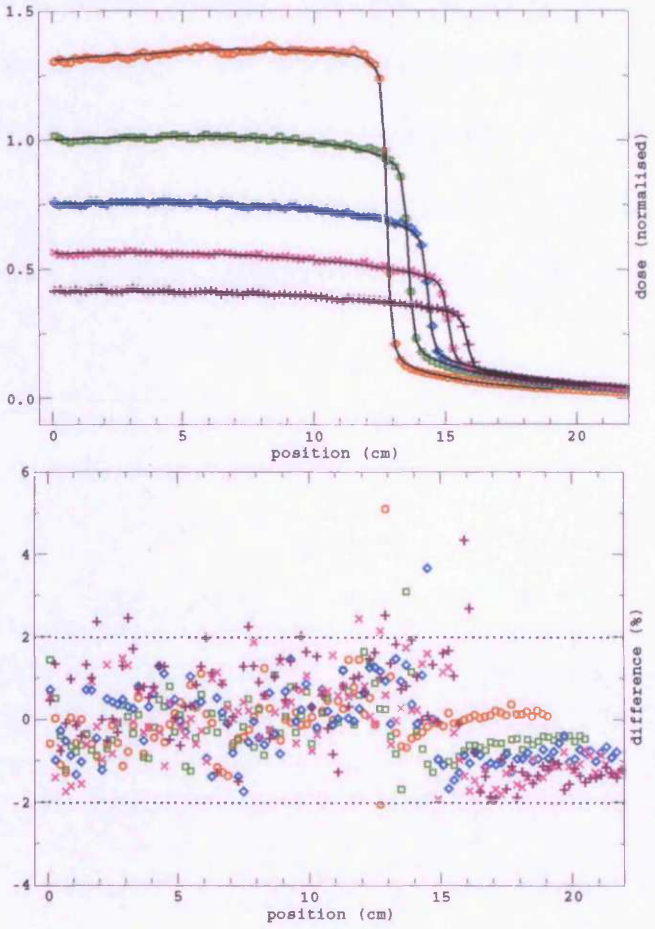

Figure 4.13: Dose profiles in a water tank for a 25 cm × 25 cm beam: measured beam data (lines) and MC simulation results (symbols).

reduction techniques create pseudo-particles, as opposed to truly, statistically, independent particles created using an analog transport.

Results confirmed that indeed the variance reduction regime combining bremsstrahlung splitting and Russian roulette produced inadequate representation of electrons. However, the difference it causes in T is no more than 2% (when 255 million particles were used), since the electron contribution to photon beams (which is of interest in

this thesis) is merely as a contaminant. That said, the combination of bremsstrahlung splitting and Russian roulette is not recommended for BEAMnrc simulations of the linac head. For future work, the recently implemented *directional bremsstrahlung splitting* [Kawrakow et al. 2004], which was designed not only to increase efficiency but also to overcome the under-representation of electrons, should instead be used.

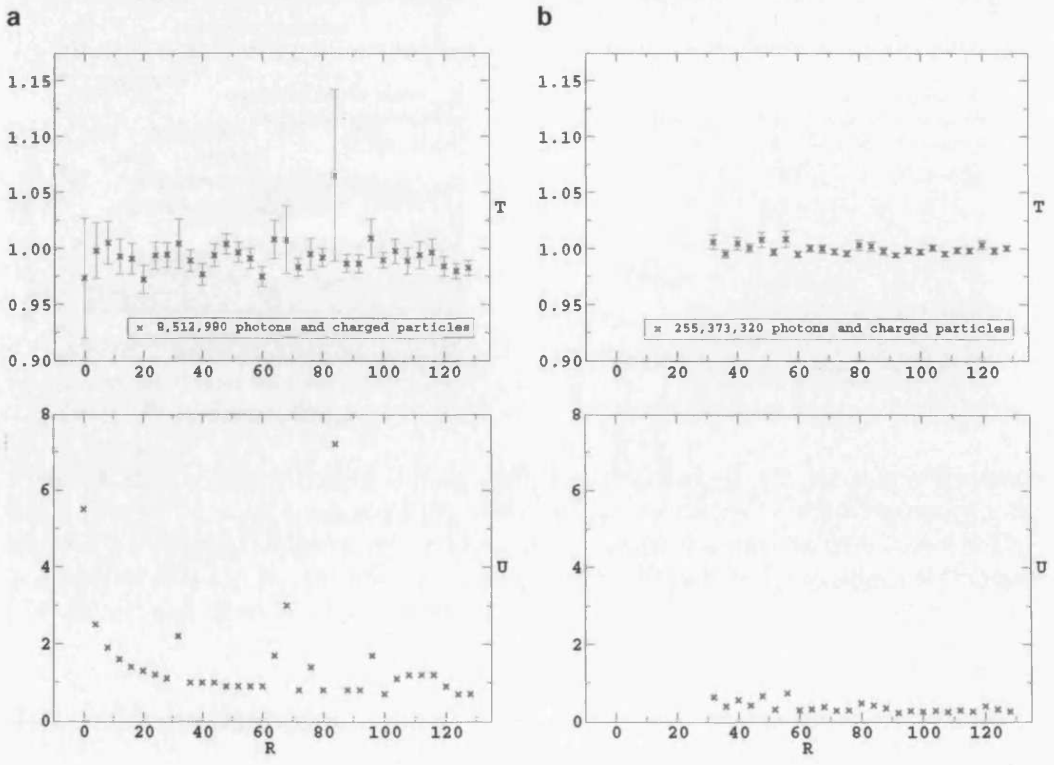

Figure 4.14: T (tally) and U (the corresponding percentage uncertainty) as a function of R (number of recycles) when a) 8,512,980; and b) 255,373,320 phase space photons and charged particles were simulated.

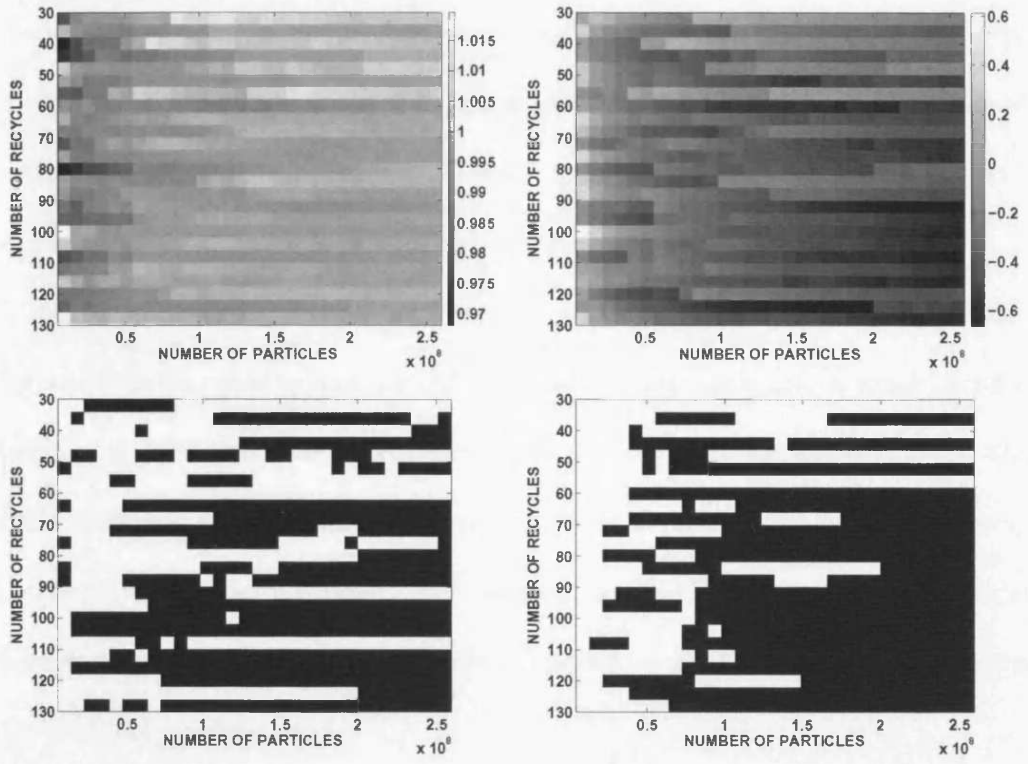

Figure 4.15: Top left: T (tally), normalised to T_m, as a function of R (number of recycles) and N (number of phase space particles). Bottom left: instances of T differing from T_m by less than 0.5% (black) and those over 0.5% (white). Top right: percentage of U (uncertainty) as a function of R and N, grayscale given in $\log_{10}$ scale. Bottom right: instances of U below 0.5% (black) and those over 0.5% (white).

4.4 Conclusions

The new BEAM version, BEAMnrc, was found to produce different simulation outcomes compared to its predecessor, BEAM00. The same input files produced photon fluences which differed by over 5% for the linac simulated here. Our investigations also indicated substantial differences when *first-class* transport made available by BEAMnrc was used in place of the default settings. Although no difference was noticeable in water phantom dose deposition, energy fluence and energy spectra of the phase

space particles differed up to 4% and 7% respectively. Our findings also confirmed insensitivity of water phantom dose deposition for analysing phase space particles, i.e. dose deposition in a water phantom is inadequate for benchmarking transport configurations for MC simulations. Instead, direct analysis of phase space particles (e.g. energy fluence and energy spectra) are recommended.

In BEAMnrc simulation of the linac, the combination of bremsstrahlung splitting and Russian roulette variance reduction techniques was found to cause peculiar statistical fluctuations, due to under-representation of contaminant electrons. The author proposes a new method for qualifying that a phase space is an adequately representative sample of a beam – by monitoring the uncertainty as a function of increasing number of particles and number of repeat cycles, as used to investigate the aforementioned anomalies.

The fine-tuned linac model was found to be a 1.0 mm radius parallel beam of 6.00 MeV electrons. The beam radius is in agreement with the range found from measurements by Jaffray et al. [1993], while the incident energy is in exact agreement with the definition of the linac energy mode, although this is only nominal.

The same linac model was found to be universally applicable for field sizes ranging from 2 cm × 2 cm to 25 cm × 25 cm. When simulated to tally dose deposition in a water tank, dose distributions were within 2% (of the central axis dose at each depth) agreement with measured beam data, except in the penumbra region of high dose gradients.

This outcome equips our data library with fully commissioned phase space files for 2 cm × 2 cm, 5 cm × 5 cm, 10 cm × 10 cm, 15 cm × 15 cm, 20 cm × 20 cm and 25

cm × 25 cm beams. These can be readily deployed for MC simulations of various dose calculations over a wide range of source-phantom-EPID setups e.g. various gantry angles, source-surface and source-detector distances. Repeated simulations of the linac head would not be necessary since 1) changing the source-phantom-EPID setup does not change the arrangement of the target, primary collimators, vacuum window, flattening filter, monitor ion chamber and mirror within the linac head; and 2) the phase space files were generated at a plane upstream from probable locations of the phantom/patient.

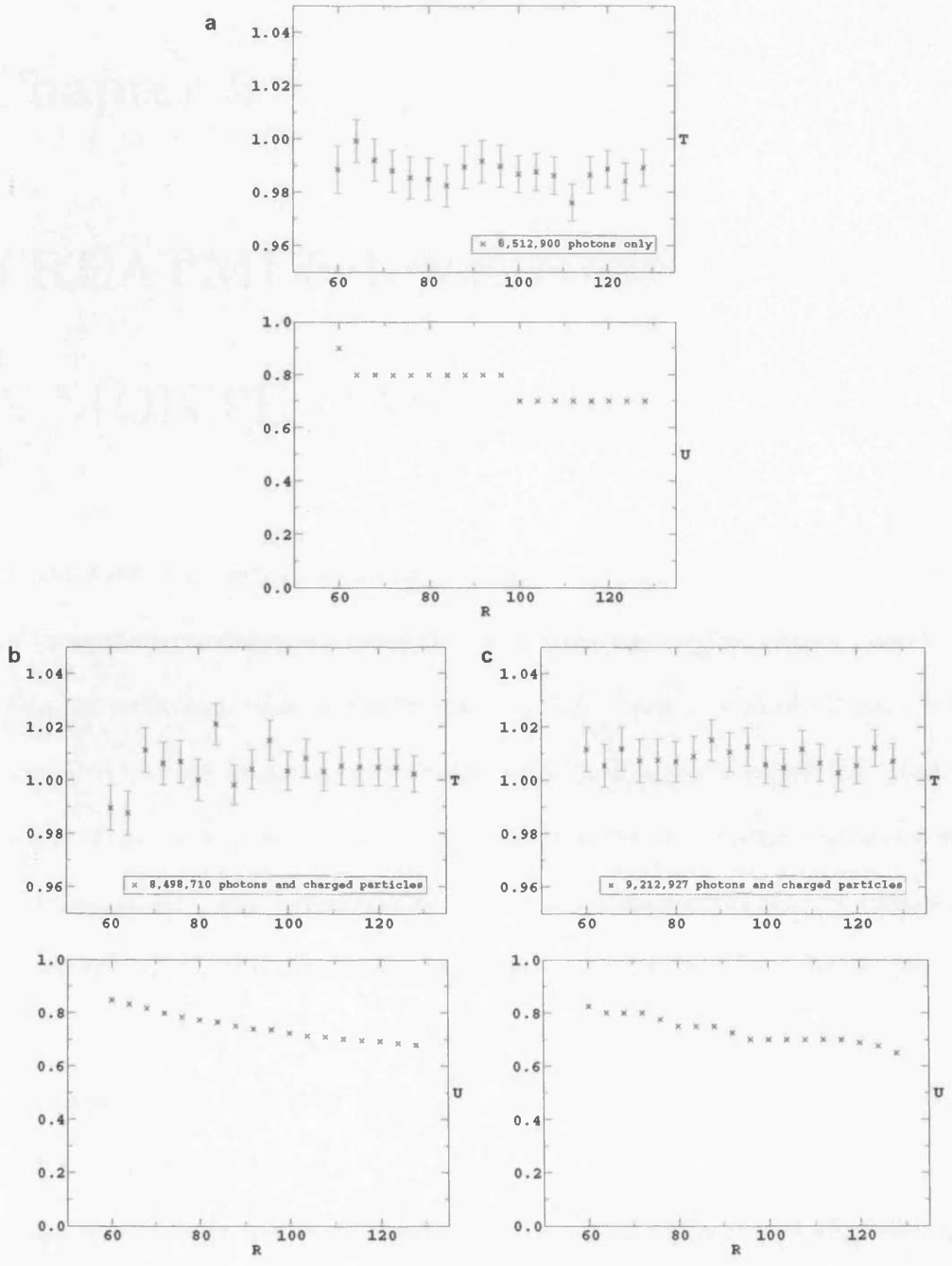

Figure 4.16: T (tally) and U (the corresponding percentage uncertainty) as a function of R (number of recycles) when a) only photons were simulated; b) phase space particles were re-simulated without bremsstrahlung splitting; and c) phase space particles were re-simulated with bremsstrahlung splitting but without Russian roulette.

Chapter 5

TREATMENT VERIFICATION: A MONTE CARLO SOLUTION

Advanced external beam radiotherapy techniques involving conformal field shaping and/or intensity modulation require thorough verification. This chapter reports a treatment verification solution which combines the accuracy of Monte Carlo (MC) simulations with the technology of electronic portal imaging devices (EPIDs). Here is the core of the thesis where the project achieved combined **versatility** and **accuracy** not known to be readily achievable by other verification techniques. The solution is **versatile** in that dose prediction has been tested over a wide range of clinical setups including high scatter conditions which complicate portal dose prediction. It is **accurate** in that agreement with measured dose profiles was consistently within 2% of the central axis value.

This was made possible by introducing a modified calibration method, a new way of simulating oblique beams using DOSXYZnrc, and a correction algorithm for gantry-dependent EPID response (which is implemented in this chapter but derivation will be given in Chapter 7).

5.1 Introduction

The clinical need for dosimetric treatment verification and the limitations of diodes and thermoluminescent dosimeters (TLDs) have been outlined in Section 1.1. The role of EPIDs is promising (Section 1.2, Chapter 2). However, existing EPID-based verification techniques lack versatility and accuracy due to assumptions made in dose calculations (Section 1.5). MC simulations are known to be the most accurate dose calculation technique because it makes no presumptions about the scatter condition in the problem at hand (Chapter 3). Combining the accuracy of MC simulations with the technology of EPIDs, this thesis developed a versatile and accurate solution for treatment verification.

The following explains how the solution works. By imaging during beam delivery, image pixel values were used to derive quantitative data on the dose delivery. This exercise converts the image to a dose map. This dose map was then compared against a dose map predicted using MC simulation based on parameters from the treatment planning system (TPS). A disagreement would indicate that beam delivery had not been according to plan.

This solution extends an existing MC verification framework developed within the same institution, which verifies TPS-calculated patient dose against MC simulations. The complete MC verification framework is outlined in Figure 5.1: *VERIFICATION 1* has been developed by Spezi ([Spezi 2003]), *VERIFICATIONS 2 & 3* are the author's contribution. Measured images are first calibrated for dose and corrected for off-axis variations (detailed in Section 5.2.1.2 and Section 5.2.1.3 respectively). Cor-

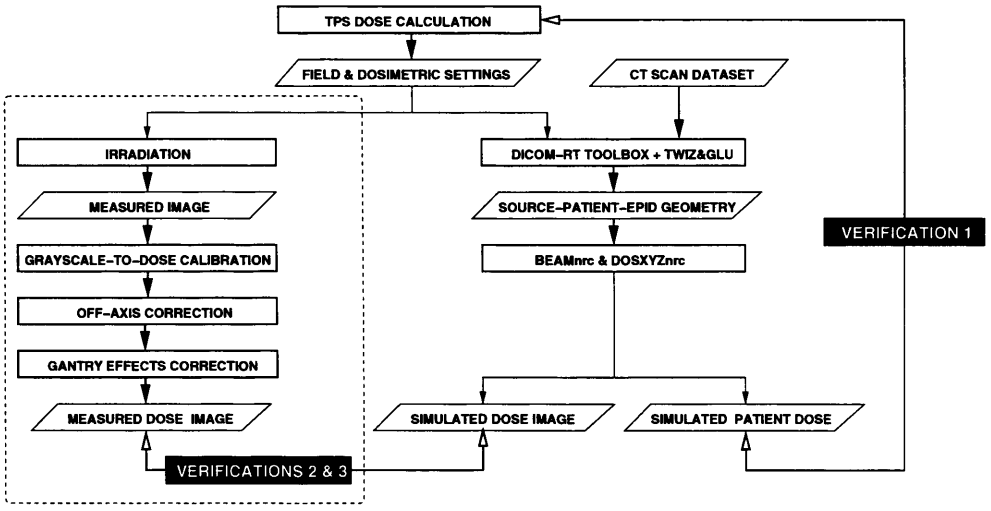

Figure 5.1: A MC verification framework: 1. verifying TPS dose calculation; 2. verifying implementation of TPS-generated parameters on treatment machine; 3. verifying patient dose delivery. Steps in the dashed box are repeated for subsequent treatment fractions.

rection for gantry effects is needed for SLIC-type EPIDs since its response varies with gantry angle, causing an artefact commonly known as the *bulging effect* (detailed in Section 7.2.1). An identical irradiation configuration would be MC-simulated. Section 5.2.3 demonstrates the use of this solution to predict portal images from a SLIC EPID over a wide range of clinical setups.

5.2 Materials and Methods

We used a Varian Clinac 2100CD linac installed with a PortalVision Mk2 SLIC EPID supported by a retractable arm (R-arm). It produces portal images of 256×256 pixels, where each square pixel is 1.27 mm in dimension, giving a 32.5 cm × 32.5 cm image area.

The SLIC detector measures dose rate but not cumulative dose [Essers et al. 1995].

Since the electronic portal images (EPIs) were acquired at approximately constant dose rates, the detector signal, and hence the image grayscale, may be assumed to be a measure of dose.

In sections where EPIs were predicted, the SLIC EPID was modelled in detail as specified by the manufacturer. DOSXYZnrc was used to predict dose deposition in each voxel on the EPID's *active detection layer**. The radiation source was provided by the phase space library produced in Chapter 4.

5.2.1 Calibrations

5.2.1.1 Image Calibration

For image calibration, standard dark field (DF) and flood field (FF) calibration was applied [Essers et al. 1995]. A dark field, acquired with beam off, accounts for chamber imperfections, electrical leakage and high-voltage switching artefacts. A flood field, acquired with an open radiation field covering the detector area, accounts for individual cell sensitivities and electrometer gains.

We performed the calibration at *SDD*† 140 cm and gantry angle 0° without placing any object in the beam. An image was acquired immediately after calibration using the same setup as that used for calibration. Uniformity of this image gave an indication of calibration validity. For this purpose, image matrix $\mathbf{I_0}$ was compared with the (scalar) central axis value C_0. The uniformity matrix was calculated as

$$\mathbf{M} = \frac{\mathbf{I_0} - C_0}{C_0} \tag{5.1}$$

*The *active detection layer* is the layer containing iso-octane.
†The *SDD* has been defined in Figure 2.6.

5.2.1.2 Grayscale-to-dose Calibration

Before an EPI could be interpreted as a dose map, a grayscale-to-dose calibration is needed. The calibration function, once established, can be used for converting subsequent EPIs into dose maps. To construct the calibration function, matching pairs of grayscale and dose values are required across the desired calibration range.

Our calibration function was constructed by relating physically-acquired grayscales to MC-simulated doses. EPIs were physically acquired for varying beam sizes (5 cm $\times$ 5 cm to 20 cm $\times$ 20 cm), perspex phantom thicknesses (0 cm to 20 cm) and SDDs (105 cm to 140 cm) so that a range of effective doses incident on the detector could be obtained. The gantry angle was kept at 0°. For each physically-acquired EPI, the same irradiation condition was simulated to produce a corresponding MC-simulated dose map.

Matching pairs of grayscale and dose values were extracted from the physically-acquired EPI and the corresponding MC-simulated dose map respectively. Values were averaged over a 1 cm $\times$ 1 cm area at the centre of the EPI and the dose map, which corresponds to the beam central axis.

The grayscale G (dimensionless) and dose D (in units of Gray per incident particle history) values obtained were curve-fitted using regression model I:

$$G = \alpha\sqrt{D} \tag{5.2}$$

and model II:

$$G = \alpha D + \beta\sqrt{D} + \gamma \tag{5.3}$$

where α, β and γ are the regression coefficients. Model I is the *square-root response function* commonly used (e.g. Spezi and Lewis [2002]) as an approximation to model II, which has been derived theoretically [Essers et al. 1995]. The models were evaluated for applicability across different dose levels.

5.2.1.3 Off-axis Calibration

As mentioned earlier, DF/FF calibration was performed without placing any object in the field. Consequently, images of the same setup calibrated this way would be uniform, therefore losing the unflatness or *horns* due to the flattening filter. To offset this effect, an off-axis calibration is needed. We *restore the horns* by analysing a dose map from MC-simulation of an irradiation condition identical to that during FF calibration, that is, a 25 cm square field incident on the EPID at SDD 140 cm.

From this MC-simulated dose map, an off-axis-ratio map was derived by dividing the value of each pixel by that of the central axis. This off-axis-ratio map was modelled in two ways:

1. the square-ring method [Spezi and Lewis 2002]. Starting from the central axis (CAX), pixels were grouped into concentric square rings of increasing distance from the CAX. Regression was done with the value at each pixel as the dependent variable, and the distance of the side of the square ring from the CAX as the independent variable.

2. the radial distance method, where regression was done with the value at each pixel as the dependent variable, and the distance of the pixel centre from the CAX as the independent variable.

The models were analysed by calculating the difference from the original off-axis-ratio map.

5.2.2 Phantom Packaging Using TWIZ&GLU

MC simulation of portal dosimetry requires both the phantom and the imager to be modelled. At gantry angles of 0° (Figure 5.2a), 90° and 270°, voxel boundaries directly correspond to phantom and imager surfaces. At an oblique angle, however, the voxel boundaries no longer directly correspond to imager surfaces (Figure 5.2b).

DOSXYZnrc [Walters and Rogers 2002] is frequently used for dose simulation in a phantom. The geometry is specified on a set of orthogonal planes. These planes form a 3D lattice of voxels where each voxel is assigned a material and a density. Consequently, accurate specification of voxel boundaries not directly corresponding to imager surfaces (as happens in portal dosimetry of oblique beams, explained in the previous paragraph) is problematic. Whereas DOSXYZnrc allows the beam to be directed onto the voxel grid from any gantry angle, it was not designed to model objects with planes oriented obliquely to each other within the voxel grid. We therefore developed a MATLAB* script for packaging an integrated phantom to serve as input for DOSXYZnrc simulations. With this, we present a variable angle solution

*A language of technical computing. The website is at www.mathworks.com.

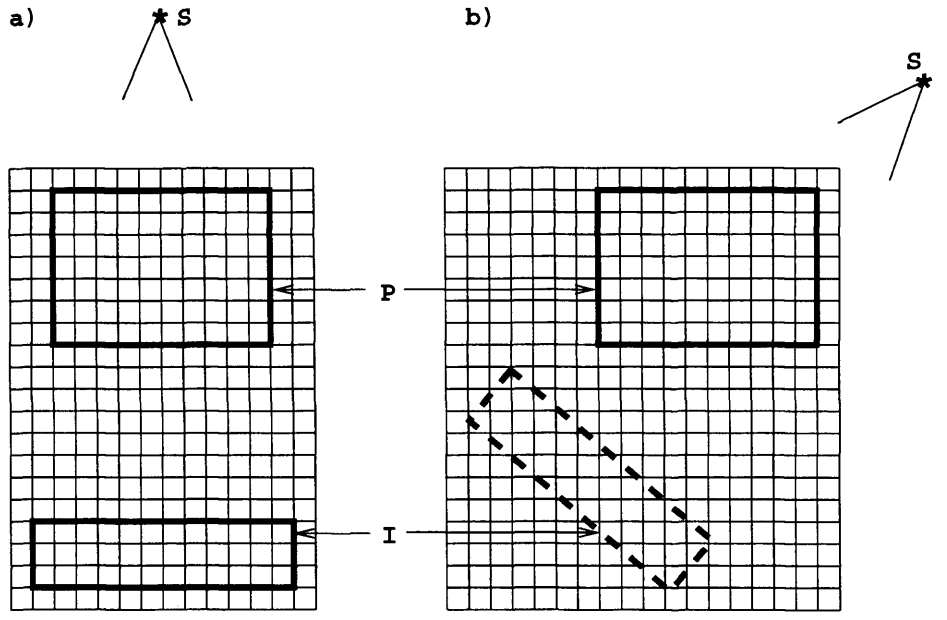

Figure 5.2: Defining a patient/phantom dataset (P) and an imager (I) on a common rectilinear grid. Beam direction from the source (S) is shown: a) irradiation from gantry angle of 0°; b) irradiation from an oblique angle, where the voxel boundaries no longer directly correspond to the imager surfaces (dashed box).

for MC simulation of phantom-imager geometries.

For simulation of portal dosimetry at gantry angle of $\theta°$ (Figure 5.3a), the script we developed (TWIZ&GLU) operated on the patient/phantom CT dataset in three steps: 1) rotating the phantom by -$\theta°$ around the isocentre (Figure 5.3b); 2) "padding" the exterior of the phantom with additional air-filled voxels to obtain a rectangular frame (Figure 5.3c); and 3) adding the EPID beneath the phantom at a specified SDD (Figure 5.3d). The integrated phantom was then ready to serve as input for a DOSXYZnrc run, in which the beam was directed as if the gantry was not rotated.

The phantom file was produced in ASCII format, similar to that used in DOSXYZ-nrc. However, the author introduced a new material indexing convention. In DOSXYZ-

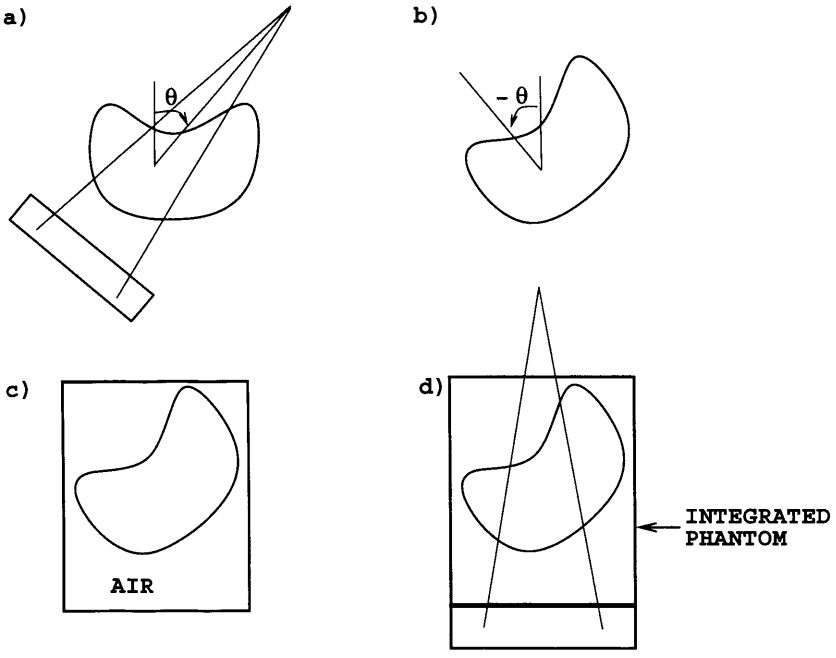

Figure 5.3: a) The task of modelling a phantom-imager geometry for irradiation at gantry angle of $\theta°$. TWIZ&GLU operated in three steps: b) rotating the phantom by -$\theta°$ around the isocentre; c) "padding" the exterior of the phantom with additional air-filled voxels; d) adding the EPID downstream from the phantom at a specified SDD. The beam direction is shown.

nrc, each material in a CT phantom is indexed using a single digit ranging from one to nine. This limits the phantom composition to a maximum of 9 materials, which is insufficient for the integrated phantoms developed in this work. By incorporating characters and symbols from the ASCII map, our new indexing convention extended the limit to over 200 materials. DOSXYZnrc was similarly modified for compatibility.

Rotation, resolution resampling and discretisation from continuous contours into pixel-defined contours may cause distortions, asymmetries and artefacts. Some of these are illustrated in Figure 5.4. S_1 is a result of rotation of a straight-sided square. The sides became stepped, demonstrating step artefacts. Also shown is S_2 which joins

the centres of each vertex pixel. S_3 is the location of S_2 after a 90° rotation. The non-overlapping of S_2 and S_3 shows that the right-angled corners were not faithfully reproduced. More extensive deviations will occur when a larger pixel size is used.

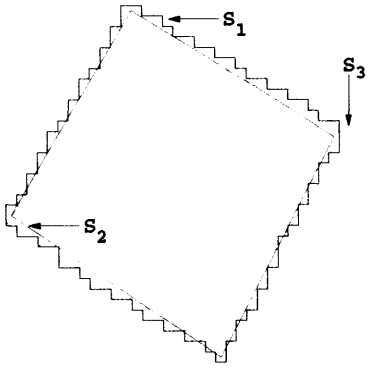

Figure 5.4: S_1 is a result of the rotation of a straight-sided square. The sides are stepped and the corners are not truly right angles. S_2 (solid line) joins the centre of each vertex pixel. S_3 (dashed line) is the location of S_2 after a 90° rotation.

With these concerns in mind, we tested the accuracy of geometric transformations by TWIZ&GLU. This was done using trigonometric calculations on the rotation of a 10 cm × 10 cm square. Reproducibility of the length of each side, reproducibility of the geometric centre, and the accuracy of rotation angles were tested for rotation angles in steps of 10° over the entire circle. The length of each side and the angle of rotation were calculated trigonometrically from the coordinates of the centre of each vertex pixel. Verification of the geometric transformation algorithm was repeated for pixel sizes 2 mm, 2.5 mm, 3 mm and 4 mm.

Upon completing technical tests on the geometric transformations, we investigated the implementation of the integrated phantom method for MC simulations. Two independent MC computations of portal dose were performed on a 10 cm × 10 cm

× 10 cm water phantom irradiated at gantry angle of 45°, source-axis distance 100 cm and SDD 140 cm: 1) a conventional BEAMnrc run on a cubic phantom followed by a DOSXYZnrc run for scoring portal dose (Figure 5.5a and c). Here, the CM* *pyramids* was used to generate two wedge shapes arranged to form a cubic phantom. 2) a DOSXYZnrc run on a TWIZ&GLU-generated phantom consisting of a cube rotated by 45° and an EPID (Figure 5.5b and c). Cubic phantoms in both cases were identical. Dose profiles were then compared.

All simulations in this section used a 6 MV, 10 cm × 10 cm accelerator source phase space file, as detailed in Chapter 4.

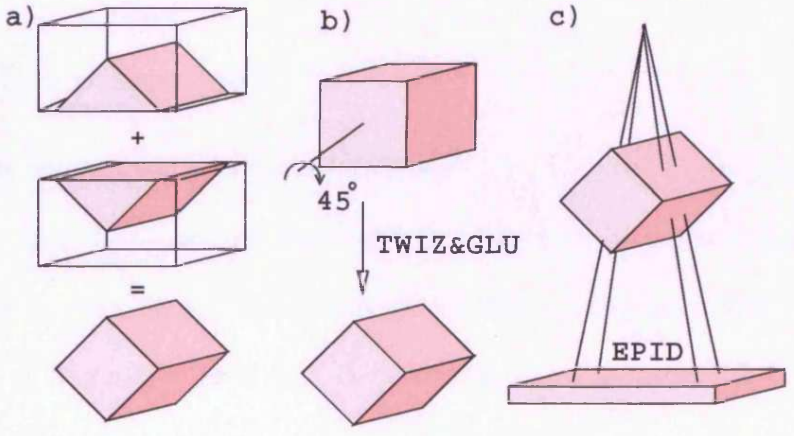

Figure 5.5: Identical phantoms generated using a) *pyramids* CM from BEAMnrc; b) TWIZ&GLU by rotating a cube over 45°; c) MC simulation of phantom irradiation for portal dosimetry.

Finally, we demonstrated an application of the newly developed solution for portal dose prediction. An EPI was taken for oblique beam irradiation of an inhomogeneous solid water phantom. This was compared with a MC simulation performed under

*Component modules (CMs) have been introduced in Section 3.4.

identical conditions. Shown in Figure 5.6, the 30 cm × 30 cm × 18 cm water phantom with an embedded 4 cm × 30 cm × 2 cm air gap was irradiated at gantry angle of 20° by a 10 cm × 10 cm 6 MV photon beam, *SSD** 90 cm and SDD 140 cm.

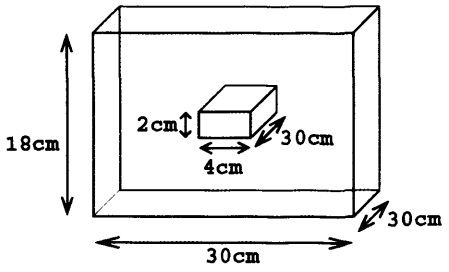

Figure 5.6: A solid water phantom with an air gap at the centre.

5.2.3 Demonstrations

To test the verification chain developed (Figure 5.1), 15 cm × 15 cm perspex slabs of 1 cm, 2 cm and 2.5 cm thick were constructed in-house by the physics workshop. Additionally, some slabs were constructed with a 5 cm × 5 cm cutout at the centre. A base plate of the same material extends beyond the couch to support the slabs. This way, the couch could be kept out of the imaged beam. EPIs were physically-acquired and MC-predicted for varying:

- field sizes (5 cm, 10 cm, 15 cm and 20 cm square fields)

- phantom-EPID air gap distance† (4 cm, 28 cm and 38 cm)

*The *SSD* has been defined in Figure 2.6.
†The *air gap distance* has been defined in Figure 2.6.

- gantry angles (20°, 140°, 240° and 280° as representative samples across all 4 quadrants at varying tilt from the vertical)

The 4 cm gap value was the minimum phantom-EPID separation achievable without collision between the EPID and the couch. This minimum separation was close to provide a high radiation scatter component as a stringent test condition.

Using the calibration function of model II and the radial distance method for off-axis calibration, dose profiles were extracted from the EPIs and the dose maps.

5.3 Results & Discussion

5.3.1 Calibrations

5.3.1.1 Image Calibration

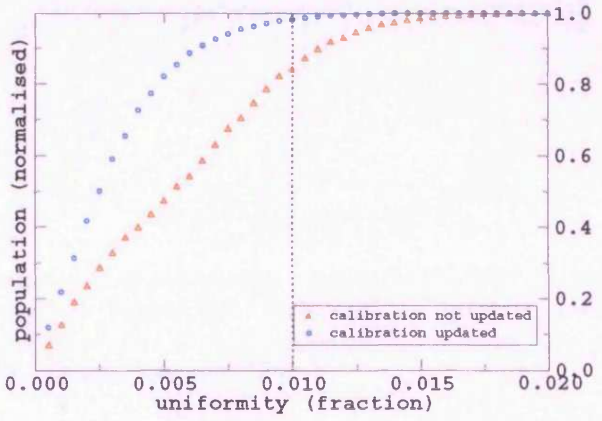

Figure 5.7: Cumulative histograms for image uniformity of two images: one acquired during a session which began with a calibration update; another acquired on a day when the most recent calibration update was a fortnight earlier.

To check the validity of DF/FF calibration, each pixel of $\mathbf{I}_0$ was compared with

C_0. A cumulative histogram of uniformity as defined in Equation (5.1) is shown in Figure 5.7 for two images: one acquired during a session which began with a calibration update; another acquired on a day when the most recent calibration update was a fortnight earlier. Results indicated the importance of calibration updates in dosimetric work. When the calibration was not updated during the same session, only 87% of the pixels achieved 1% uniformity. However, when the calibration was updated at the start of the session, uniformity was very good, with 99% of the pixels uniform within 1%.

5.3.1.2 Grayscale-to-dose Calibration

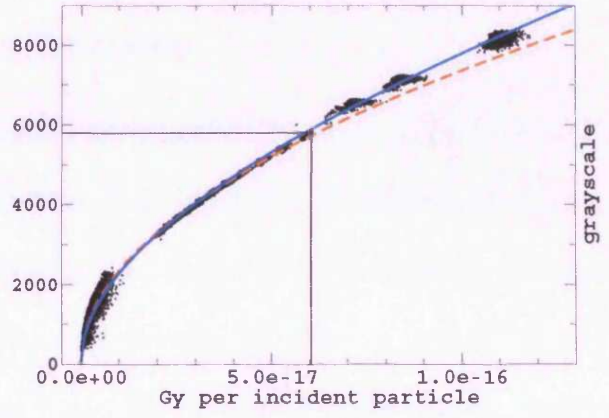

Figure 5.8: Grayscale-to-dose calibration: physically-acquired grayscales on the vertical axis and MC-simulated dose values on the horizontal axis (dots). Also shown are the regression models I (dashed curve) and II (continuous curve), and the data point corresponding to the previously tested limit (straight lines).

Curve-fitting results for grayscale-to-dose calibration are shown in Figure 5.8. Model I fits well up to the previously tested limit (marked on figure), which is a 10 cm square field without any object placed in the beam at SDD 140 cm [Spezi and

Lewis 2002]. It, however, overestimates the dose at regions of higher dose. Model II fits better over the entire tested range. The coefficients found for model II were $\alpha = 100.5$, $\beta = 2136$ and $\gamma = 25.79$. Our findings confirm the increasing significance of α as the dose increases [Essers et al. 1995].

This calibration method, where dose values for the horizontal axis of the calibration curve (Figure 5.8) are derived from MC simulations, is more accurate than other methods [Boellaard et al. 1996, McNutt et al. 1996, van Esch et al. 2001, 2004, Vieira et al. 2004], where dose values are obtained from ion chamber measurements in a water phantom. A comparison of these two calibration methods will be given in Chapter 6.

5.3.1.3 Off-axis Calibration

From the MC-simulated dose map for a 25 cm square field at SDD 140 cm, the off-axis-ratio map was calculated (Figure 5.9 A) and modelled using the square-ring and the radial distance methods. Off-axis-ratio maps produced from the models (Figure 5.9 B and C) were analysed by calculating the difference from the original (Figure 5.9 D and E). The square-ring method produced an X-shape artefact, particularly noticeable at large field sizes. The radial distance model is more accurate since the flattening filter has circular, not square, symmetry. And it is the flattening filter which shapes the off-axis effects that we are trying to model. The radial distance model produced the following relation for off-axis calibration:

$$OAR = 1.298 \times 10^{-5} r^3 - 5.536 \times 10^{-4} r^2 + 0.0098r + 0.9937 \quad (5.4)$$

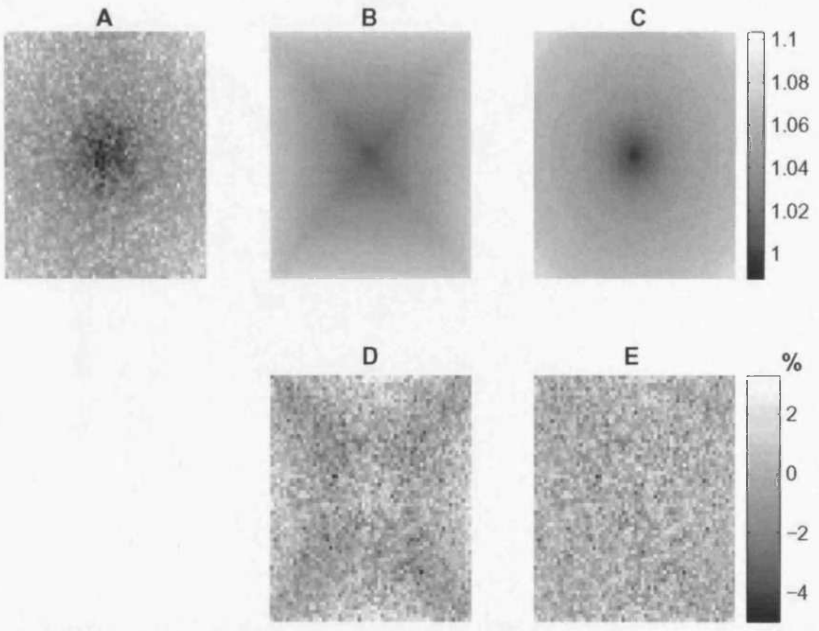

Figure 5.9: Off-axis calibration: off-axis-ratio maps from (A) the original dose map; (B) the square-ring model; and (C) the radial distance model. (D) difference between A and B, where an X-shape artefact is visible. (E) difference between A and C.

where OAR is the off-axis-ratio and r is the distance from the central axis in centimetres.

5.3.2 Phantom Packaging Using TWIZ&GLU

As illustrated in Figure 5.4, TWIZ&GLU was tested for spatial shift and angular deviation. The length of each side of the rotated square was found to deviate from that calculated trigonometrically by less than a single pixel size. A similar degree of uncertainty was observed for the reproducibility of the geometric centre. The rotation angle measured deviated from its true value by less than 1° for a 2 mm pixel size,

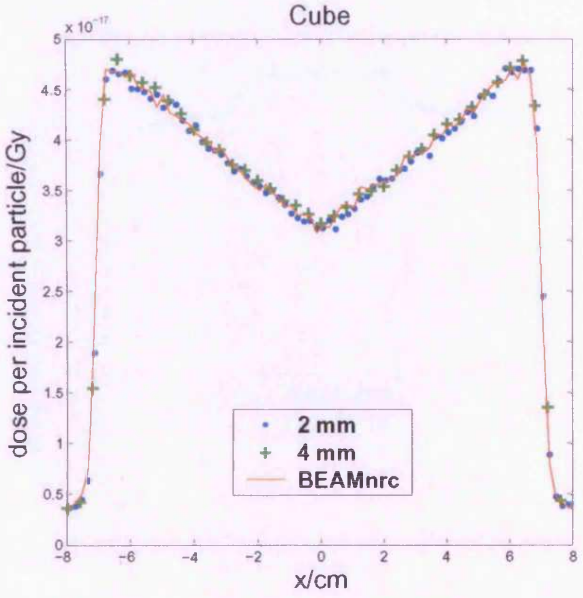

Figure 5.10: Crossplane profiles of cubes irradiated at gantry angle of 20°, for comparing integrated phantoms of pixel sizes 2 mm and 4 mm with *pyramids* CMs of BEAMnrc.

and less than 2° for a 4 mm pixel size.

These findings confirmed successful implementation of the integrated phantom method for MC simulations. As shown in Figure 5.10, good agreement was found between dose profiles of two identical geometries produced independently (Figure 5.5): one using the CMs from BEAMnrc, another using the integrated phantom from TWIZ&GLU. Figure 5.10 also shows that step artefacts caused no detrimental impact. No significant loss of accuracy was observed from 4 mm pixel size.

Finally, portal dose prediction of a solid water slab embedded with an air gap irradiated at gantry angle of 20° was compared with measurements. The agreement was good throughout (Figure 5.11) with a root-mean-square of the difference below 2% within the field, confirming the geometry transformation has not compromised

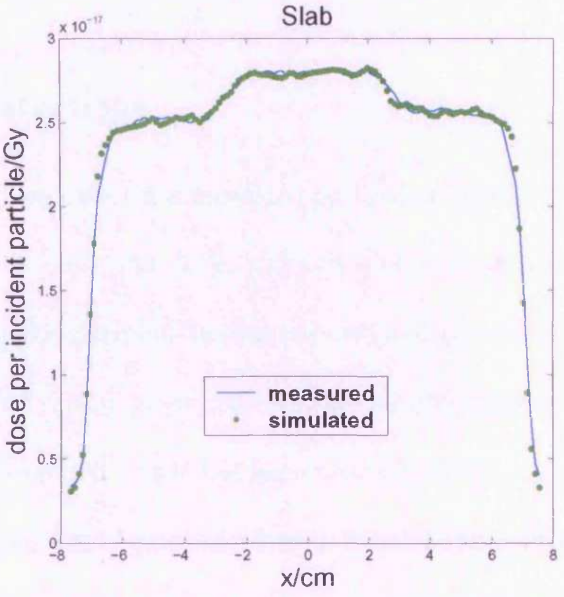

Figure 5.11: Crossplane profiles of a solid water phantom embedded with an air gap, irradiated at gantry angle of 20°.

the accuracy of the simulations.

In constructing an integrated phantom of objects oriented obliquely to each other, in our case the phantom and the imager, objects were put into a common rectilinear grid. Our implementation rotated and resampled the phantom in order to correspond to the orientation of the imager. Alternatively, the imager could be rotated and resampled into the grid defining the phantom. However, this alternative approach would lead to inaccurate projection of the different thicknesses of the detector layers on the grid.

Another alternative to using an integrated phantom would be to simulate each stage of the process (Figure 5.3) successively. This would require a phase space output from simulation of the CT phantom, which requires additional disk space and

is not supported by the current version of DOSXYZnrc.

5.3.3 Demonstrations

Agreement between simulated and measured portal dose profiles was generally within 2% of the central axis dose (Fig. 5.12, 5.13 and 5.14), except in regions of high dose gradient which are particularly susceptible to positional uncertainties of the measuring devices and linac jaws during measurements. For all comparisons shown in Fig. 5.12, 5.13 and 5.14, the measured profile has been normalised to the measured portal dose at SDD 140 cm on the central axis of a 10 cm × 10 cm beam; the predicted profile has been normalised to the predicted portal dose at the same beam-EPID setup. This allows absolute dose verification. It should be emphasised that the measured and predicted profiles were never normalised to each other, as practised elsewhere (e.g. McCurdy et al. [2001]).

No field size dependence was observed. There was no loss of accuracy 1) in high scatter conditions when the phantom-to-EPID separation was only 4 cm; 2) with the presence of a 20 cm cubic perspex phantom, even when a 4 cm-thick, 5 cm × 5 cm air cavity was introduced at its centre; 3) when the gantry was rotated for delivery of oblique beams; and 4) in the absence of additional buildup on the EPID. Such inclusive versatility is known to be unachievable in non-MC portal dosimetry [Boellaard et al. 1997, van Esch et al. 2001, Vieira et al. 2004] as explained in Section 1.5.

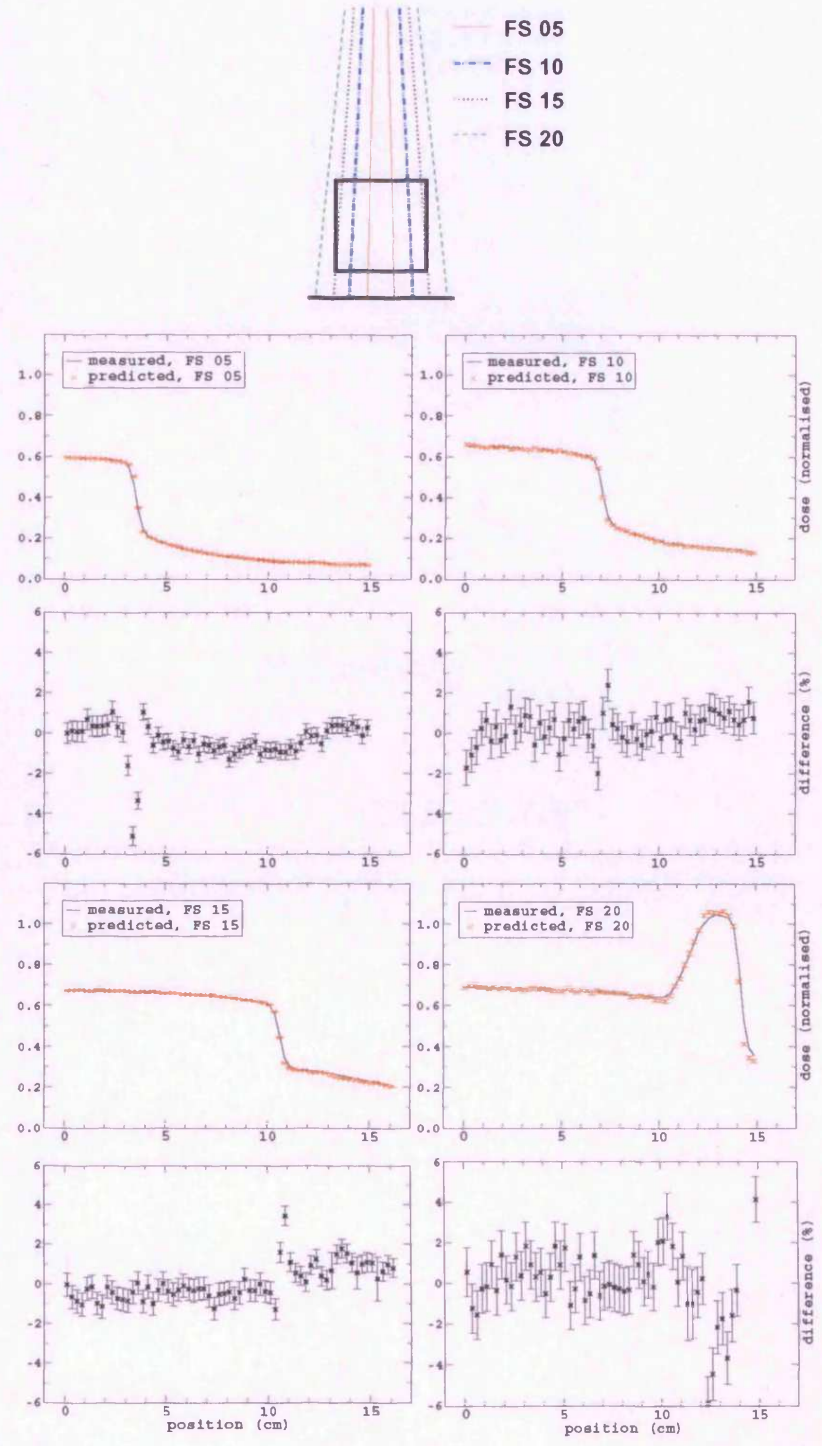

Figure 5.12: Irradiation of a homogeneous phantom at 5 cm, 10 cm, 15 cm and 20 cm square field sizes: the beam-phantom-EPID setup, the predicted and measured portal dose profiles, and the corresponding differences. The air gap distance and the gantry angle were fixed at 13 cm and 0° respectively.

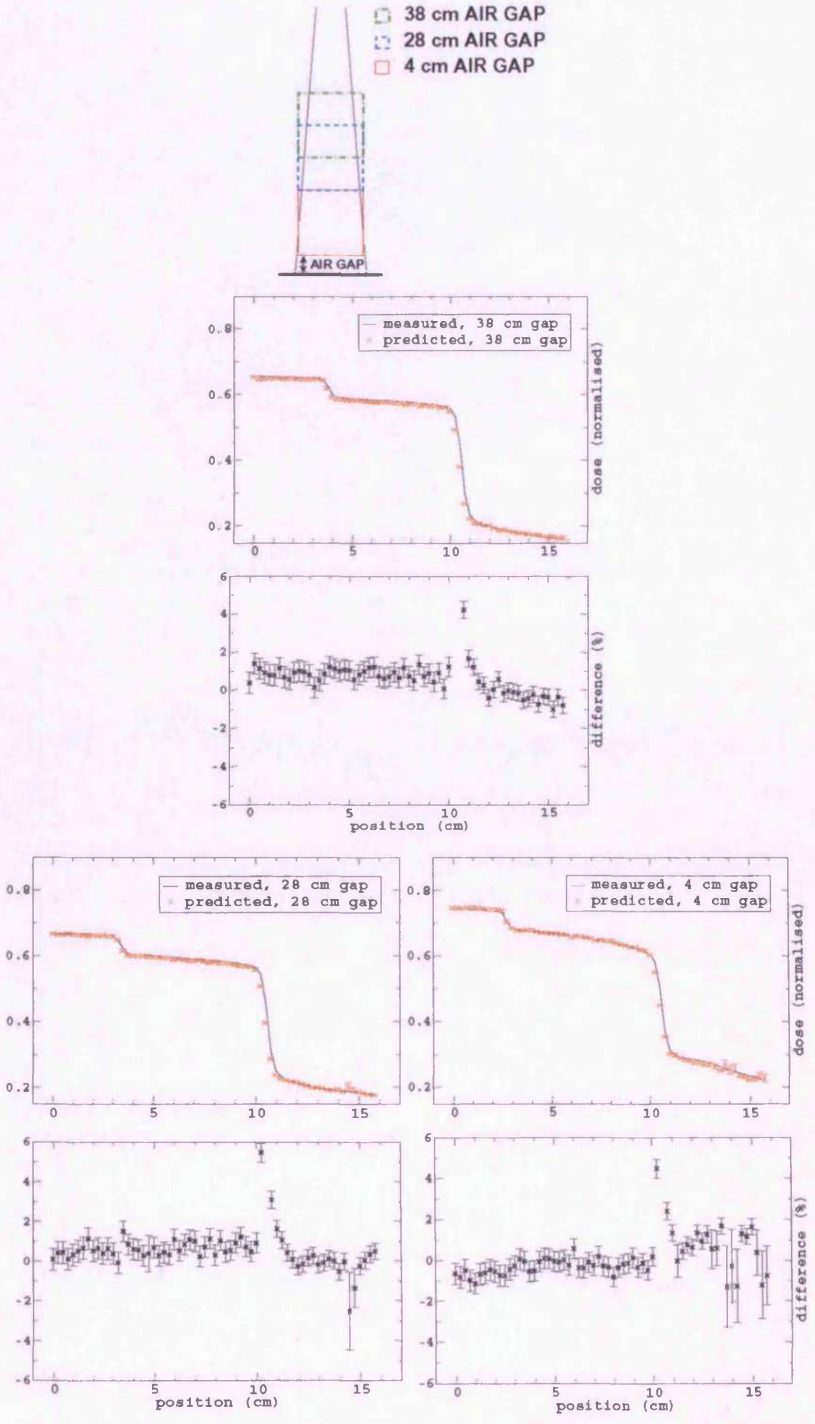

Figure 5.13: Irradiation of an inhomogeneous phantom (Figure 5.6) at air gap distances 38 cm, 28 cm and 4 cm: the beam-phantom-EPID setup, the predicted and measured portal dose profiles, and the corresponding differences. The field size and the gantry angle were fixed at 15 cm × 15 cm and 0° respectively.

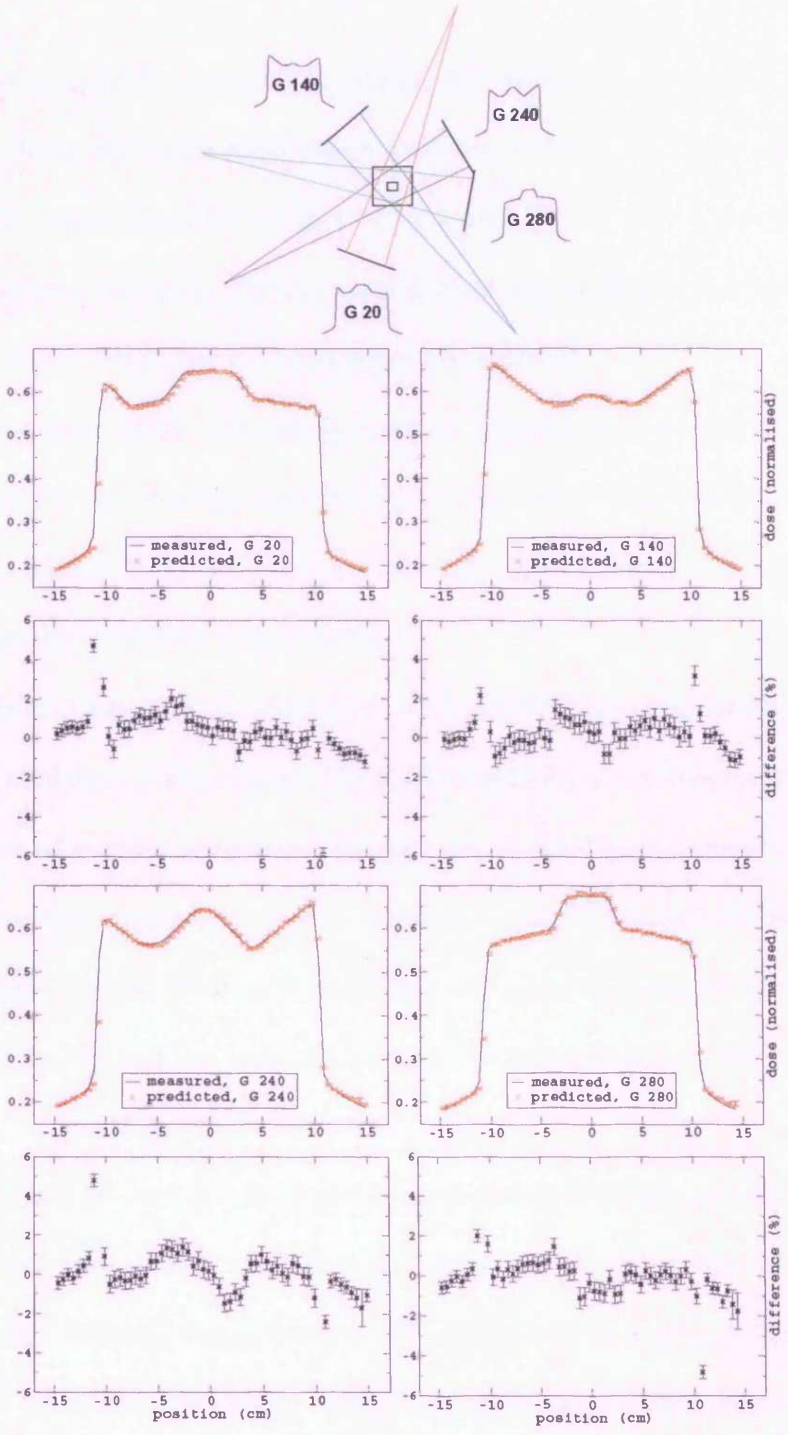

Figure 5.14: Isocentric irradiation of an inhomogeneous phantom (Figure 5.6) at gantry angles 20°, 140°, 240° and 280°: the beam-phantom-EPID setup, the predicted and measured portal dose profiles, and the corresponding differences. The field size and the SDD were fixed at 15 cm × 15 cm and 140 cm respectively.

5.4 Conclusions

This project successfully extended an existing MC calibration method for predicting SLIC EPIs [Spezi and Lewis 2002], which had been limited to 0° gantry angle and 10 cm × 10 cm beams. Now, EPI prediction for beams from 5 cm × 5 cm up to 20 cm × 20 cm has been validated. The improved method also allows portal dose prediction of oblique beams, which has not been previously reported.

This was achieved by introducing modified grayscale-to-dose and off-axis calibration methods, a correction algorithm for gantry-dependent artefacts in the SLIC (detailed in Section 7.2.1), and a novel solution to enable DOSXYZnrc simulations of portal dosimetry at oblique gantry angles.

TWIZ&GLU has been developed to enable DOSXYZnrc simulations of portal dosimetry at oblique gantry angles. The solution is based on an integrated phantom, whereby the effect of incident beam obliquity was included using geometric transformations. Geometric transformations are accurate within ±1 mm and ±1° with respect to exact values calculated using trigonometry. As a process independent of the MC code itself, the TWIZ&GLU solution is compatible across evolving code generations, e.g. DOSXYZ and DOSXYZnrc.

The versatile MC solution for external beam photon radiotherapy verification has been validated under a wide range of clinical setups, including high scatter conditions which complicate portal dose prediction. Off-axis agreement with portal dose profiles was within 2% of the central axis value. This combined versatility and accuracy is not readily achievable by other techniques.

Whereas the examples shown here were based on the SLIC EPID, the MC solution shown in Figure 5.1 can be readily adapted for the a-Si EPID as follows:

1. replacing the quadratic function in Section 5.2.1.2 with a linear grayscale-to-dose calibration function (details in Chapter 6), which would be even simpler;

2. employing a similar off-axis calibration method, by deriving new coefficients based on actual and predicted EPIs of an a-Si EPID;

3. ignoring the corrections for bulging effect (Section 7.2.1), which are irrelevant for the a-Si EPID as it does not contain liquid;

4. employing the same TWIZ&GLU solution.

Chapter 6

OPTIMISATION OF MONTE CARLO SIMULATIONS

The radiation source, the geometry and the transport parameters are important user inputs to a Monte Carlo (MC) simulation (Figure 1.4). The reliability of simulation output depends largely on these inputs, i.e. "garbage in, garbage out". This thesis includes optimisation of each of these inputs, in order to achieve a high calculation accuracy and a high run time efficiency. Optimisation of the radiation source has been presented in Chapter 4. Optimisation of the geometry and the transport parameters in electronic portal imaging device (EPID) simulation will be presented in this chapter.

Practically useful and scientifically interesting MC studies of EPIDs will be reported. Beginning with dosimetrically verified amorphous silicon (a-Si) and scanning liquid ionisation chamber (SLIC) EPID models, simplified models were designed by first studying, layer-by-layer, the interaction types and energy depositions in the EPIDs. The simplified models not only reduce MC simulation run times, but are also potentially applicable to non-MC dose computation techniques. Effects of various MC transport options on portal dose prediction in both EPIDs will also be reported.

6.1 Introduction

In introducing the stages of radiation detection in EPIDs, Section 2.3 described the *converter* and the *detector* as the two components forming "the heart" of the EPID (Figure 2.6). For the a-Si EPID, the converter is a combination of a 1 mm copper plate and a Gd_2O_2S:Tb screen; the detector is a glass substrate containing an array of photodiodes. For the SLIC EPID, the converter is a 1 mm plastoferrite plate and the detector is a layer of iso-octane, an organic liquid.

Various MC studies of megavoltage portal imaging have been reported. By MC modelling the SLIC EPID, Keller et al. [1998] simulated dose spread kernels in units of absolute dose per incident energy fluence. von Wittenau et al. [2002] investigated dose components contributing to, and energy dependence of, image blurring on a hypothetical a-Si imager. Using an algorithm by Radcliffe et al. [1993], both Kausch et al. [1999] and Cremers et al. [2004], in their study of metal/phosphor imager performance, included simulation of optical transport in the phosphor. Munro and Mulligan [2002] investigated the effects of metal plate type and thickness on the signal, subject contrast, signal contrast and detective quantum efficiency (DQE) of EC-L portal film cassettes; a modified design was proposed. Ko et al. [2004] showed that backscatter causes asymmetry in dosimetric images from an a-Si EPID; the maximum thickness of backscatter material was theorised. Bissonnette et al. [1997, 2003] used the *quantum accounting diagram* (QAD) theory* and studied the optimal phosphor thickness for portal imaging.

*The QAD theory models a linear imaging system as a serial cascade of blur and gain stages.

This work did not explore alternative constructions for manufacturing EPIDs, but developed alternative models for computation of radiation quantities (e.g. dose) in EPIDs. Formulation was therefore not subjected to the many constraints and approximations in physical phantom fabrication [White et al. 1988]. Based on studies of radiation transport through complete detector models, simplified models were designed and tested for the a-Si and the SLIC EPIDs respectively. The effects of transport settings on MC simulation of both EPID types were also investigated. Additionally, water-equivalence of both EPID types, which is pertinent in most non-MC portal dosimetry techniques, was studied.

6.2 Materials and Methods

6.2.1 Radiation Transport Studies

This work began with dosimetrically working MC models of the a-Si [Siebers et al. 2004] and the SLIC [Spezi and Lewis 2002] EPIDs, which have been successfully verified against measurements. The a-Si model contains 24 layers (Figure 6.1), while the SLIC model contains 15 layers (Figure 6.4), of different materials according to details provided by the manufacturer. In addition to the skeleton of a typical portal imaging cassette given in Figure 2.6, both EPIDs contain internal support structures and protective housing, where interleaving materials such as rohacell*, FR4† and

*The rohacell is a hard foam material.
†The FR4 is a printed circuit board material.

copper foils* can be commonly found.

To facilitate our understanding of radiation transport in the EPID, EGSnrc codes were written to tally the interaction type, energy deposition and backscatter contribution in each layer of the a-Si and the SLIC EPIDs respectively. The EPIDs were irradiated by a 6 MV 10 cm × 10 cm beam, using a phase space file previously generated from a BEAMnrc simulation (Chapter 4). The relevance of this MC study will become evident in Section 6.3.1, as interaction types and energy deposition in each layer may not be directly intuitive (e.g. from lookup tables) since each layer is of varying thickness and many are compounds of different elements in different proportions.

6.2.2 Design of Simplified EPID Models

A fully detailed, multi-layered model entails frequent boundary crossing during MC simulations (causing long run times) and cannot be readily implemented for non-MC calculations (e.g. conventional TPSs, convolution/superposition techniques.) Simplified models could therefore be useful as alternatives for dosimetric computation. Aided by the results from Section 6.2.1, we designed simplified models for the a-Si (detailed in Section 6.2.2.1) and the SLIC (detailed in Section 6.2.2.2) respectively.

Each simplified EPID model was tested against the respective complete model by comparing portal dose profiles under 4 irradiation setups:

1. a 2 cm × 2 cm *open field*†;

*The copper foils are cladding on the FR4 layers to isolate/ground electrically the materials surrounding the EPID.

†An *open field* is a radiation field without any object placed in the beam.

2. a 10 cm × 10 cm open field;

3. a 20 cm × 20 cm open field; and

4. a 20 cm × 20 cm open field, with a 20 cm-thick, 32.5 cm × 32.5 cm water phantom positioned at *SSD* 114 cm, which resulted in the minimum phantom-to-EPID air gap distance for a *SDD* of 140 cm.* The minimum air gap distance was to provide high scatter as a stringent test condition. The centre of the water phantom was aligned to the isocentre in longitudinal and lateral directions.

In each test, to reduce statistical noise, a portal dose profile was tallied over a 4 cm-wide band centred on the central axis – for all cases except when the beam was 2 cm × 2 cm, where a 1.6 cm-wide band was used instead. The number of histories per hour and the standard error of the tallies were observed. Where a portal dose profile is tallied, simulations in this work assumed 100% pixel *fill factor*† i.e. that the entire area of each pixel is radiation sensitive.

Where a profile B is compared against a profile A, each profile was first normalised to its value at the central axis. D_{loc}, the local point-to-point difference, and D_{cax}, the difference with respect to the central axis value, were calculated:

$$D_{loc} = \frac{A_i - B_i}{\frac{A_i + B_i}{2}} \tag{6.1}$$

$$D_{cax} = \frac{A_i - B_i}{A_o} \tag{6.2}$$

*SSD, SDD and the phantom-EPID air gap distance have been defined in Figure 2.6.

†The *fill factor* is the percentage of radiation sensitive area, which is usually less than 100% due to the electronics circuitry around each pixel.

where subscript i denotes the ith point on the profile, and A_o denotes the value at central axis of the reference profile A. The purpose of calculating both D_{loc} and D_{cax} was to provide information for two criteria, decided upon according to the circumstances. The former is more conservative, e.g. at the field umbra in Figure 6.7a, A_i and B_i are less than 5% of A_o. Therefore, D_{cax} would be lower than D_{loc}. At the practical level, a high D_{loc} in the field umbra could be insignificant compared to the dose prescribed to point A_o.

6.2.2.1 A Simplified a-Si EPID Model

Two simplified a-Si EPID models were tested and compared with the original model. Models are labelled as follows:

A. the original, full 28-layered model as specified by the manufacturer;

B. a model simplified from model A, consisting of 11 layers, 3 of which were vacuum; and

C. a model simplified from model A, consisting of 16 layers, 3 of which were vacuum.

6.2.2.2 A Simplified SLIC EPID Model

A 4-layer simplified SLIC EPID model was designed. The 4 layers are:

1. the top cover of a medium composed of elements from the polystyrene, air, rohacell and two FR4 layers of the original model. By specifying the summed proportion-by-weight of each element, cross section data for the medium were generated using pre-processor PEGS4 [Kawrakow and Rogers 2002]. To main-

tain the beam divergence incident on the *active detection layer**, the thickness of the top cover was set equal to the total thickness of the layers it replaced. The density was calculated so that the total weight remained unchanged.

2. the *buildup* or photon-to-electron converter (plastoferrite) is kept but relocated immediately upstream from the active detection layer.

3. the active detection layer is left unchanged.

4. the back cover is reduced to a 0.8 mm-thick FR4 layer.

All copper layers (each 1.6 μm-thick) were not included in the simplified SLIC EPID model.

6.2.3 Selection of Transport Options

With the release of the *nrc* versions of EGS, BEAM and DOSXYZ, various transport options became user-selectable. While there is a default setting which should be adequate for most radiotherapy applications, it should not be taken for granted to produce accurate results for all problems. We investigated the following transport options in DOSXYZnrc simulations for the a-Si and the SLIC portal dose predictions respectively:

1. bound Compton scattering ON or OFF (the default). ON is more accurate but the difference is expected to be insignificant except at very low energies [Johns and Cunningham 1983].

*The *active detection layer* is the layer containing iso-octane.

2. electron boundary crossing algorithm EXACT or PRESTA-I (the default). EXACT is more accurate but the difference is usually negligible at high energies. It switches into single elastic scattering mode near boundaries. PRESTA-I is more efficient.

3. pair production angular sampling SIMPLE (the default) or Koch-Motz.

4. photoelectron angular sampling OFF (the default) or ON.

5. bremsstrahlung angular sampling SIMPLE (the default) or Koch-Motz.

6. atomic relaxation ON or OFF (the default). ON is more accurate although simulations take longer.

7. spin effects ON (the default) or OFF. ON is more accurate although simulations take longer.

8. global electron cutoffs 0.521 MeV or 0.7 MeV (rest mass included). When an electron's energy falls below this cutoff, its track its terminated with all its remaining energy deposited locally. A higher cutoff is more efficient but may bias simulation results.

Further details of the transport options are described in the literature [Kawrakow and Rogers 2002, Kawrakow 2000a]. The full, original EPID models (not the simplified models designed in Section 6.2.2) were used for this section. A 6 MV 15 cm $\times$ 15 cm beam was directed from 45° gantry angle on a 20 cm perspex cube embedded with a 5 cm $\times$ 5 cm $\times$ 4 cm air gap at the centre. For each of the transport options listed

above, simulations were run with the default and non-default selections in a paired test. Portal dose profiles were compared.

6.2.4 Comparison with Other Techniques

Most non-MC portal dose predictions [Boellaard et al. 1996, McNutt et al. 1996, van Esch et al. 2001, 2004, Vieira et al. 2004] 1) employ convolution/superposition calculation algorithms; and 2) calibrate image pixel values against ion chamber readings, thereby intrinsically assume water-equivalence of the EPID in terms of dosimetric properties. Effects of calculation algorithms on calculation outcome and the superiority of MC over convolution/superposition techniques have been widely demonstrated (see Ahnesjö and Aspradakis [1999] and references therein). This work investigated the inaccuracies due to the assumption of EPID water-equivalence, by simulating a water slab (with sufficient buildup and backscatter) of the same area and extracting dose profiles at the depth of maximum dose under 4 irradiation conditions similar to those in Section 6.2.2. These profiles were compared against profiles from the complete a-Si and SLIC models.

6.3 Results & Discussion

Figure 6.1 shows the count for each interaction type in the a-Si model. Figure 6.2 shows the energy deposition in each layer, by particles which eventually contributed to the signal, and those which did not. The copper converter layer situated 3 layers above the screen recorded the highest event count: 20% out of the total. It recorded

5 times as many Compton events as photoelectric events. Here, the bremsstrahlung event count was the highest of all layers. The function of this copper converter layer is distinct from the other, much thinner, copper foils. It is not only to convert photons into electrons (which are to form image signal), but also to absorb low-energy scattered particles (to reduce noise contribution to the signal). The former is evident from Figure 6.2, where signal-contributing energy deposition was higher in this copper layer than any of the layers above the screen. The latter is evident from the same figure, where, among the layers above the screen, non-signal-contributing energy deposition was only second to that of the top cover.

6.3.1 Radiation Transport Studies

6.3.1.1 The a-Si

Event count in the Gd_2O_2S:Tb (gadolinium oxysulphide terbium activated) screen was 12% of the total. The ratio of photoelectric, Compton and pair production event counts was 39:24:1. In real-life operation, the screen would convert electrons (mostly generated from the copper buildup layer) into light, which would be detected by the photodiodes in the glass substrate downstream to the screen; detection of photodiode signals form the portal image. In MC simulations, however, interactions are not explicitly simulated below 10 keV (explained in Section 3.1). Consequently, the following processes are not simulated explicitly: conversion into light, transport of optical photons from the scintillator to the photodiode, direct interactions of photons and electrons with the photodiodes, and generation of photodiode signals. Instead,

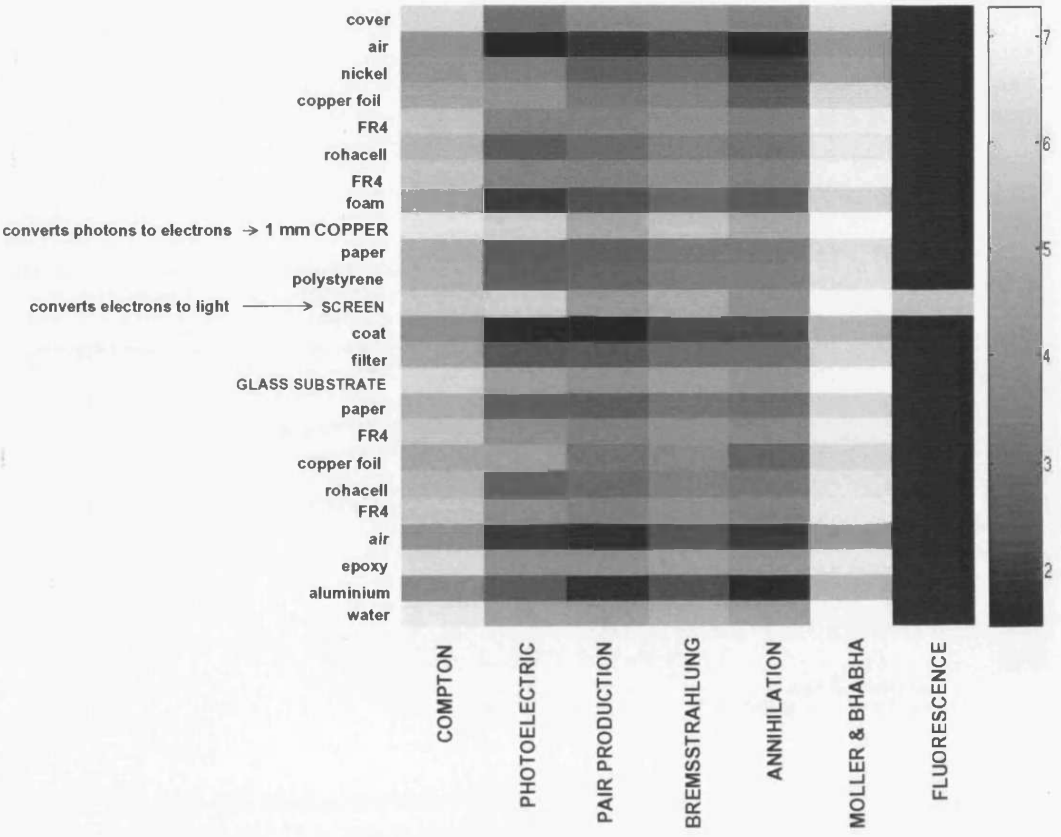

Figure 6.1: Count of each interaction type in each layer of the a-Si EPID. Grayscale is in $\log_{10}$. Thicknesses do not reflect true layer thicknesses.

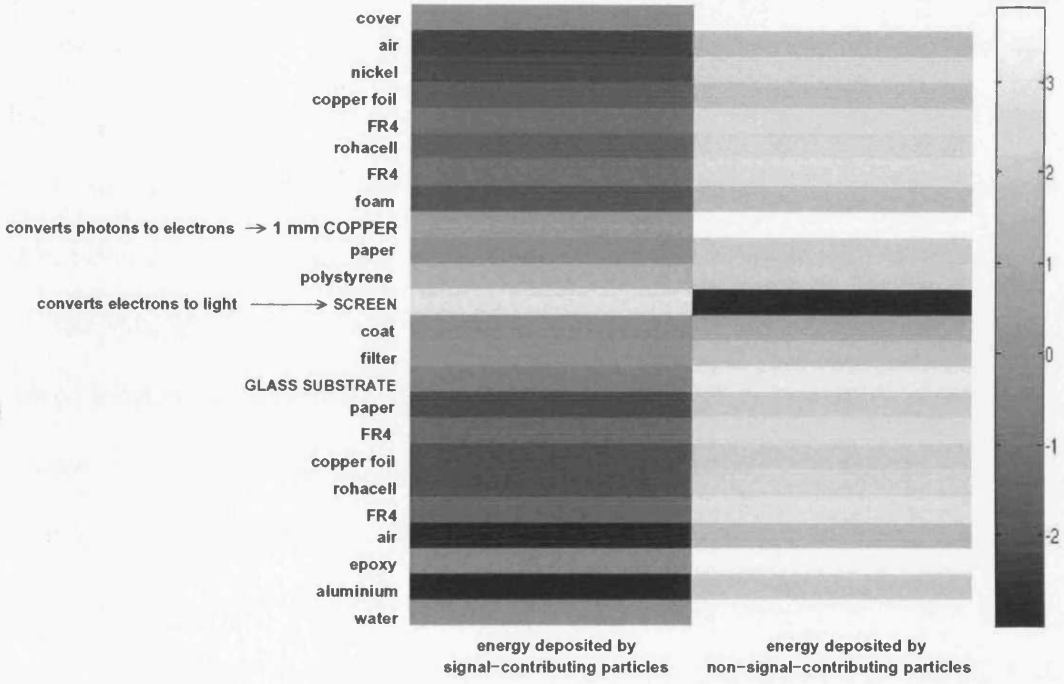

Figure 6.2: Energy deposition (MeV) in each layer of the a-Si EPID, by particles which deposited energy in the Gd_2O_2S:Tb layer, and those which did not. Grayscale is given in $\log_{10}$. Thicknesses do not reflect true layer thicknesses.

energy deposition in the screen is tallied to form the predicted portal image, as commonly practised and has been found to successfully predict portal dose [Siebers et al. 2004]. This may be explained by our understanding that direct interactions of photons and electrons with the photodiodes make sub-percent contribution to the total signal, and that photodiode response is proportional to the energy deposited in the phosphor [Munro and Bouius 1998].

The screen contains gadolinium, which has an absorption edge at 50.2 keV, explaining the fluorescence (Figure 6.1). Fluorescence was not recorded in any other layers because no other element in the a-Si model has an absorption edge above 10 keV, below which electron interactions were not simulated explicitly.

The glass layer below the screen recorded 15% of the total event count. This is where, in an actual a-Si EPID, the glass substrate containing an array of photodiodes resides. Photodiodes were not modelled in our simulations.

The nickel and aluminium layers, due to their micron-scale thickness, recorded less than 0.1% of the total event count. The FR4 layers each contributed 4 to 6% to the events count; whereas the rohacell layers each contributed 2 to 3%. Out of all signal-contributing energy deposition (Figure 6.2), only 0.04% and 0.005% were from the FR4 and rohacell layers respectively. Out of all non-signal-contributing energy deposition, 0.9% and 0.2% were in the FR4 and rohacell layers respectively. In Section 6.2.2, FR4 and rohacell layers are to be excluded from the simplified a-Si models.

Figure 6.3 shows energy deposition by particles backscattered from layers below the screen (left) and that by particles which were never backscattered from any of

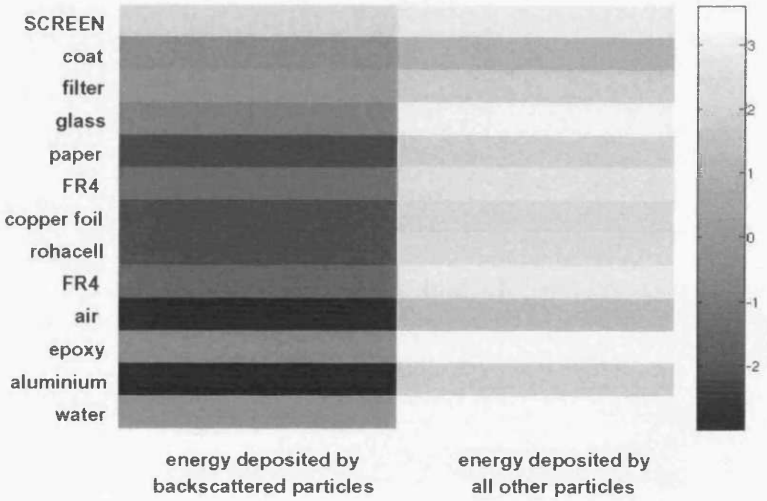

Figure 6.3: Energy deposition (MeV) in the a-Si EPID by particles backscattered from layers below the screen (left) and that by particles which were never backscattered from any of the layers below the screen (right). Grayscale is given in $\log_{10}$. Thicknesses do not reflect true layer thicknesses.

the layers below the screen (right). 18% of the total energy deposited in the screen was by backscattered particles.

6.3.1.2 The SLIC

Figure 6.4 shows the count for each interaction type in the SLIC model. Figure 6.5 shows the energy deposition in each layer, by particles which deposited energy in the iso-octane layer, and those which did not. 40% of the events took place in the plastoferrite layer, 10% in each FR4 layer and 1% in each copper layer (1.6 μm-thick). It follows that these copper layers can be excluded from the simplified SLIC model in Section 6.2.2 without affecting the results unduly.

The plastoferrite layer exhibited its distinctive role analogous to the copper buildup

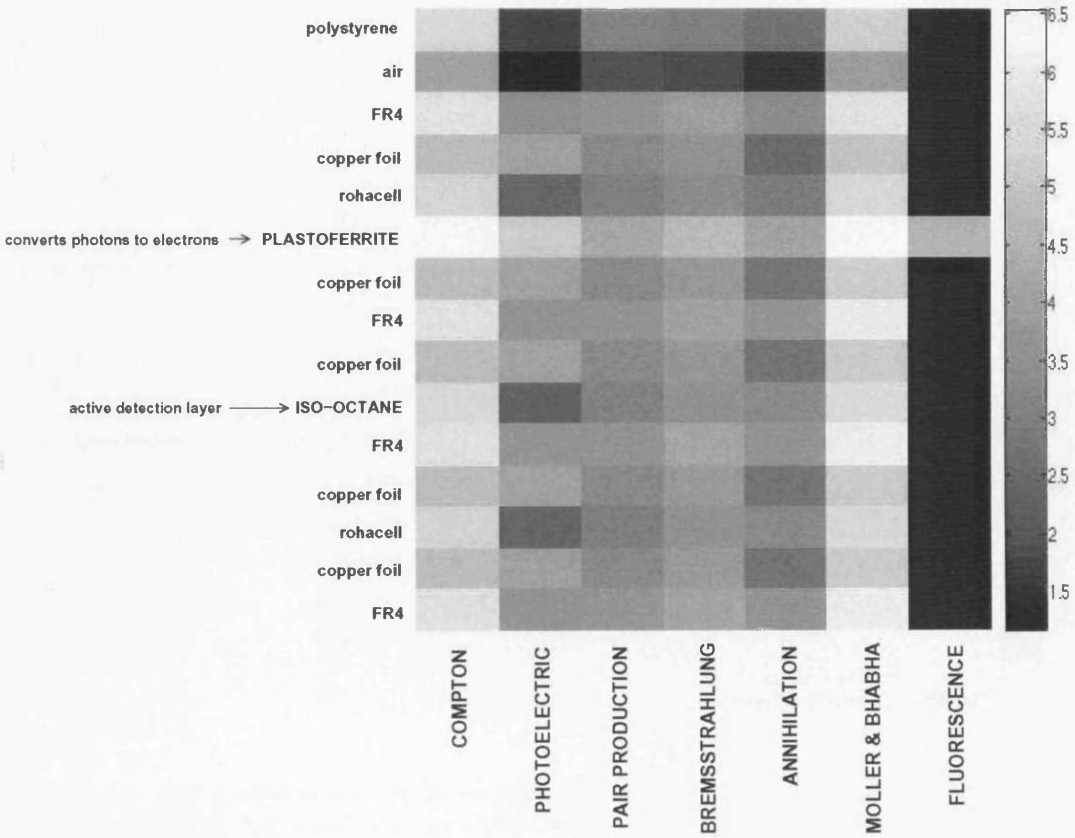

Figure 6.4: Count of each interaction type in each layer of the SLIC EPID. Grayscale is in $\log_{10}$. Thicknesses do not reflect true layer thicknesses.

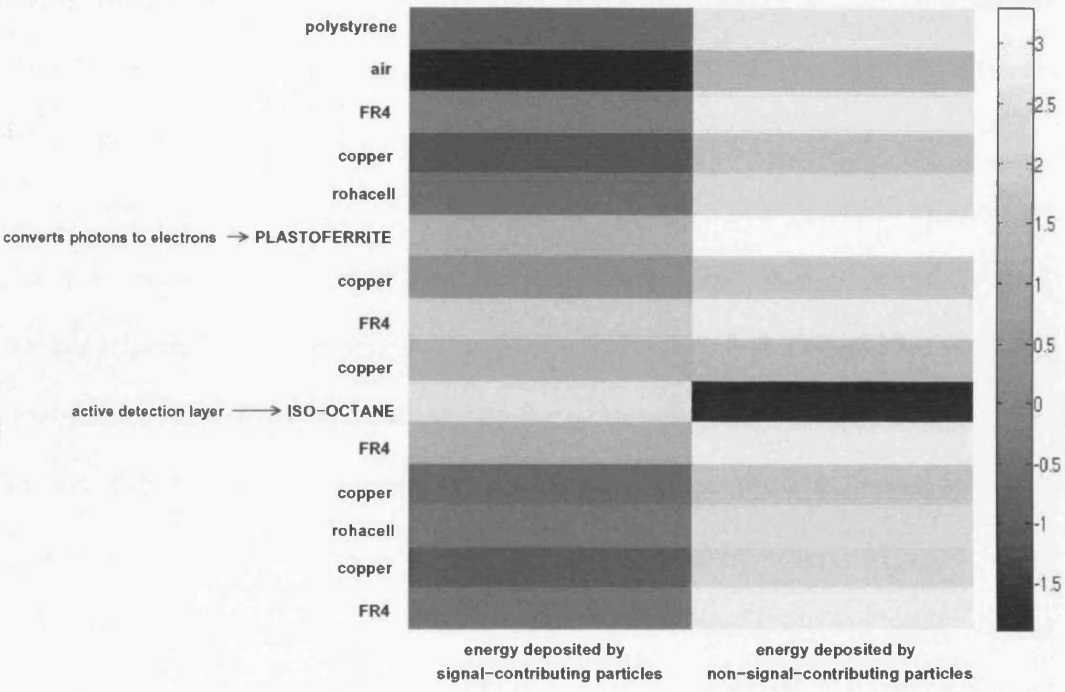

Figure 6.5: Energy deposition (MeV) in each layer of the SLIC EPID, by particles which deposited energy in the iso-octane layer (left), and those which did not deposit energy in the iso-octane layer (right). Grayscale is given in $\log_{10}$. Thicknesses do not reflect true layer thicknesses.

layer in the a-Si EPID – it not only converts photons to electrons to produce ionisation for detection, but also stops low energy particles, as evident from the high energy deposition by non-signal-contributing particles (Figure 6.5). The relative proportion of Compton, photoelectric and pair production event count was 120:6:1. Plastoferrite contains strontium, which has an absorption edge at 16.1 keV. This explains the fluorescence. Fluorescence was not recorded in any other layers because no other element in the SLIC model has an absorption edge above 10 keV, below which electron interactions were not simulated explicitly.

The iso-octane (2,2,4 trimethylpentane) layer is the active detection layer where signal is read out for image formation. In this layer, 33% were Compton events, while photoelectric events were 3 orders of magnitude lower. In real-life operation, detection of ionising radiation depends not on free electrons but on heavy ion (e.g. ionised trimethylpentane, ionised water or oxygen) transport – free electron transport does not occur because free electrons quickly bind to water, oxygen or other electronegative contaminants [van Herk 1991, Holroyd and Anderson 1985]. In our MC simulations, however, heavy ion transport was not simulated. Instead, energy deposition by charged particles in the iso-octane layer was tallied to form the predicted portal image. This approximation has been found to be valid over a wide range of source-phantom-detector setups [Chin et al. 2005].

Event counts, however, may not reflect the amount of energy absorbed. Although the bottom-most 4 layers recorded considerable event counts (Figure 6.4), signal-contributing energy depositions were minimal (Figure 6.5). It follows that in Section 6.2.2, these 4 layers are to be excluded from the simplified model.

Figure 6.6 shows energy deposition by particles backscattered from layers below the iso-octane layer and that by particles which were never backscattered from any of the layers below the iso-octane layer. 15% of the total energy deposited in the iso-octane layer was by backscattered particles. Among all layers below the iso-octane layer, signal-contributing backscattered particles deposited most energy (93%) in the FR4 layer immediately below the iso-octane layer. It follows that in Section 6.2.2, this FR4 layer is to represent the backscatter material – all other layers below it are to be excluded from the simplified model.

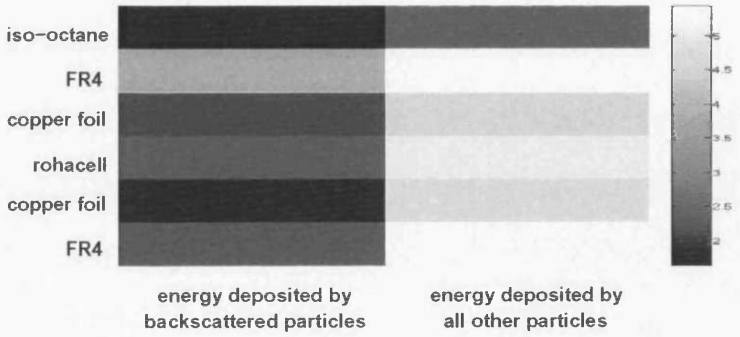

Figure 6.6: Energy deposition (MeV) in the SLIC EPID by particles backscattered from layers below the iso-octane layer (left) and that by particles which were never backscattered from any of the layers below the iso-octane layer (right). Grayscale is given in $\log_{10}$. Thicknesses do not reflect true layer thicknesses.

6.3.2 Design of Simplified EPID Models

Figure 6.7 compares portal dose profiles from a-Si models A and B. (In this work, where profiles are symmetrical about their central axis, values at symmetrical points have been averaged and plotted as a single point.) In the order of irradiation conditions listed in Section 6.2.2, D_{cax} was within 1.0%, 1.0%, 1.5% and 1.5% respectively,

while D_{loc} was within 19%, 29%, 14% and 5.2% respectively. Figure 6.8 compares portal dose profiles from a-Si models A and C: D_{cax} was always within 1.0%, while D_{loc} was within 12%, 23% 11% and 3.7% respectively.

Whether models B and C are valid approximations of model A is at the user's discretion according to the desired agreement. Simulations of models B and C reduced the number of histories simulated per unit time by 46% and 36% respectively. For a given number of histories, standard errors of the tallies were found to be independent of the model used.

Figure 6.9 compares portal dose profiles from the simplified SLIC model against that from the complete model. Except for outliers due to statistical noise, D_{cax} was within 1% for all 4 irradiation configurations tested; whereas D_{loc} was 18%, 105%, 25% and 1.4% respectively. The simplified model halved the MC run time in open field portal dose prediction.

Results of tests on the simplified a-Si and SLIC EPID models are summarised in Figure 6.10, where the root-mean-square of the difference (from the respective full models) with respect to the central axis value is plotted. Among the irradiation conditions tested, simplified EPID models were found to be most accurate for irradiation condition 1 (square field of 2 cm side); least accurate for irradiation condition 3 (20 cm square field without a water phantom in the beam).

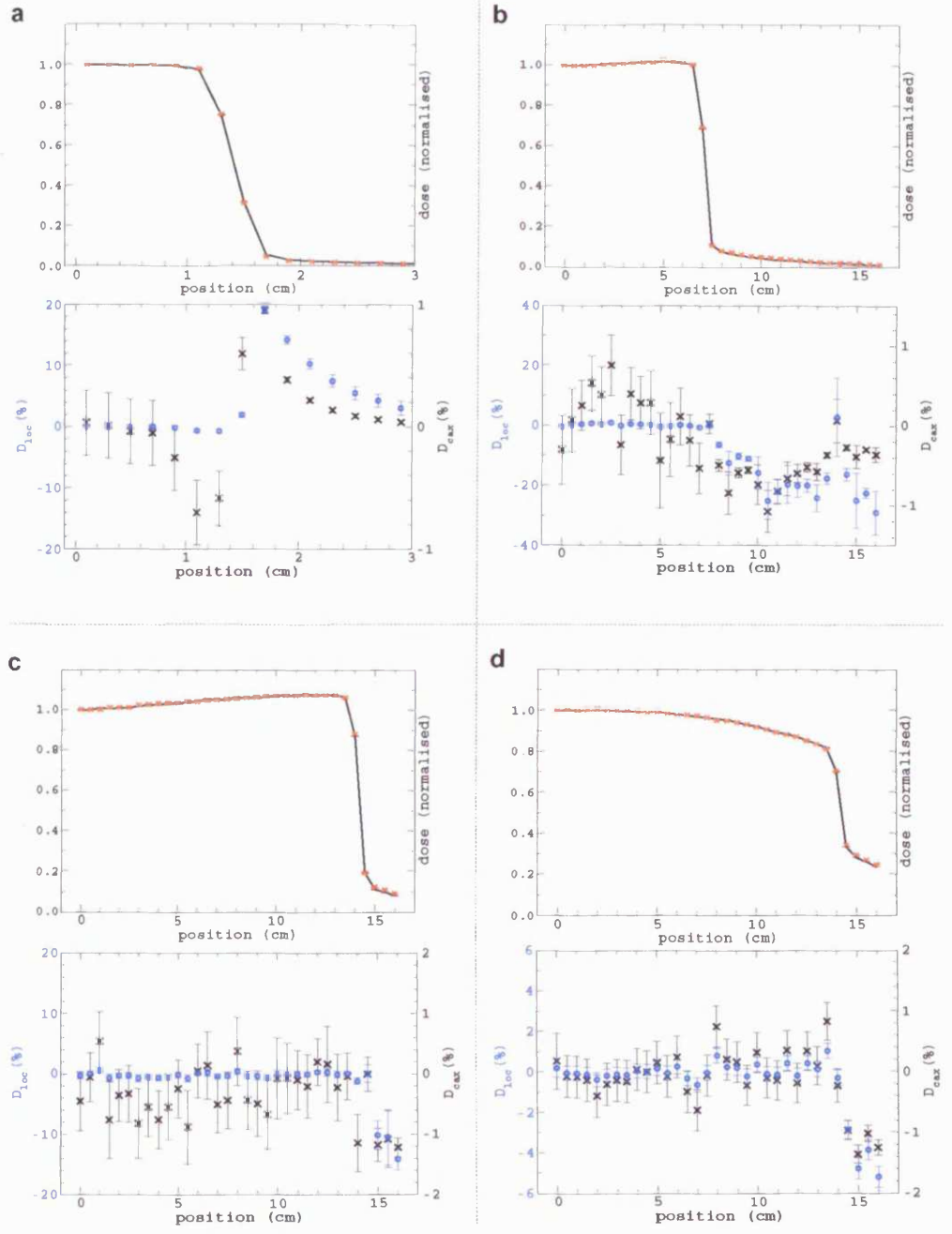

Figure 6.7: a-Si models A (black lines) versus B (red crosses): dose profiles and corresponding differences when each EPID model was irradiated by a a) 2 cm × 2 cm open field; b) 10 cm × 10 cm open field; c) 20 cm × 20 cm open field; and d) 20 cm × 20 cm field, water phantom in the field.

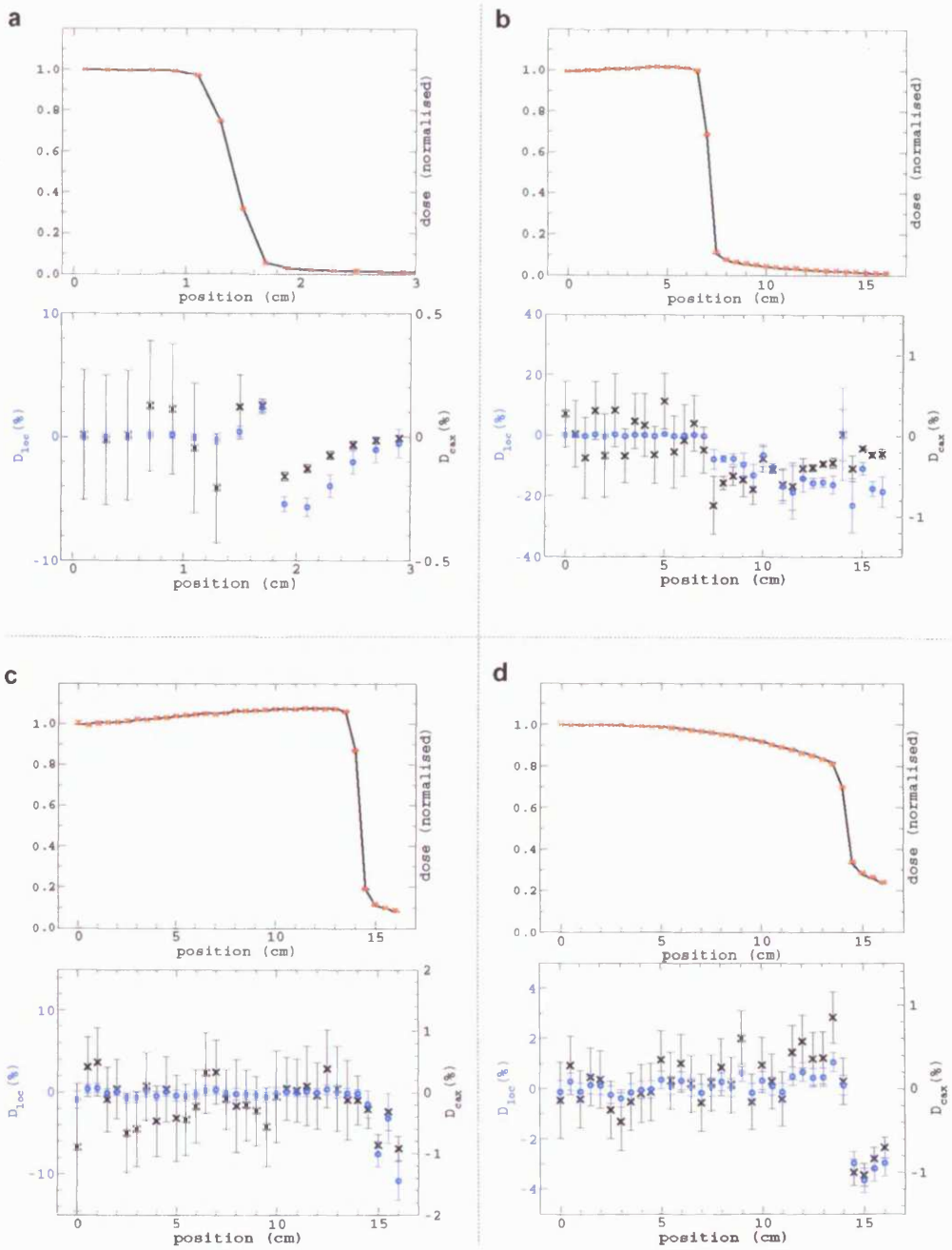

Figure 6.8: a-Si models A (black lines) versus C (red crosses): dose profiles and corresponding differences when each EPID model was irradiated by a a) 2 cm × 2 cm open field; b) 10 cm × 10 cm open field; c) 20 cm × 20 cm open field; and d) 20 cm × 20 cm field, water phantom in the field.

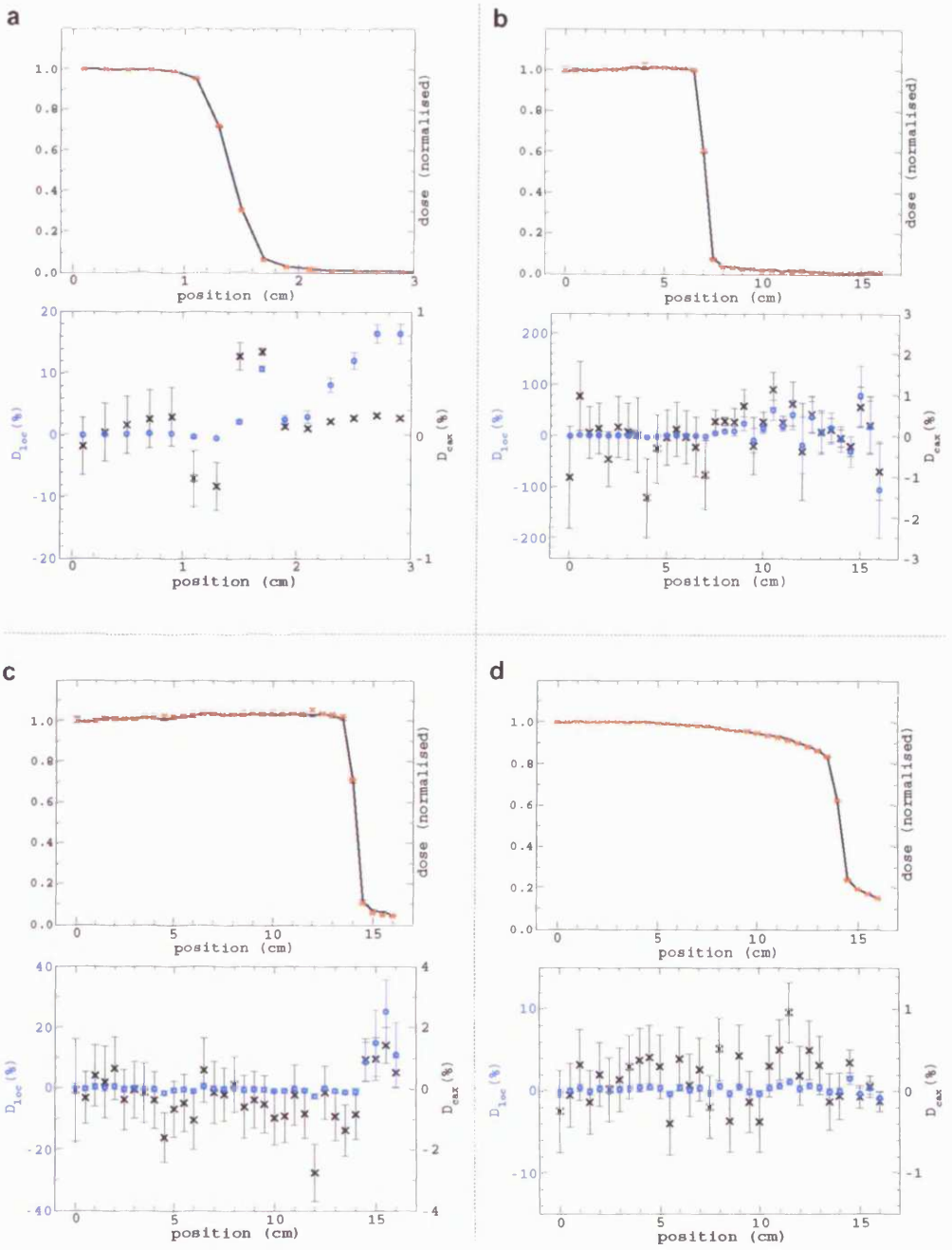

Figure 6.9: The full SLIC model (black lines) versus the simplified SLIC model (red crosses): dose profiles and corresponding differences when each EPID model was irradiated by a a) 2 cm × 2 cm open field; b) 10 cm × 10 cm open field; c) 20 cm × 20 cm open field; and d) 20 cm × 20 cm field, water phantom in the field.

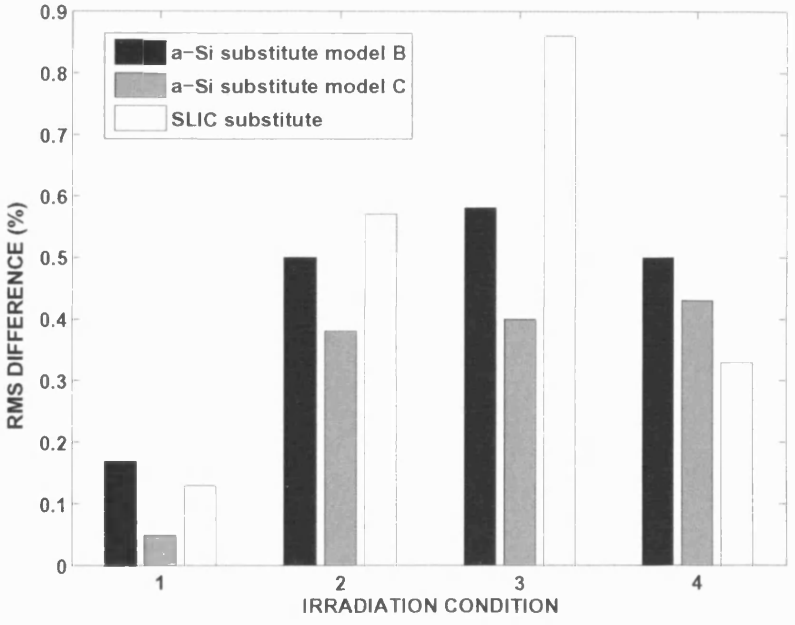

Figure 6.10: The simplified a-Si EPID models (B and C) and the simplified SLIC EPID model compared to the full a-Si and SLIC models respectively: root-mean-square of the differences under irradiation conditions 1 (2 cm-side square field), 2 (10 cm-side square field), 3 (20 cm-side square field) and 4 (20 cm-side square field with a water phantom in the beam).

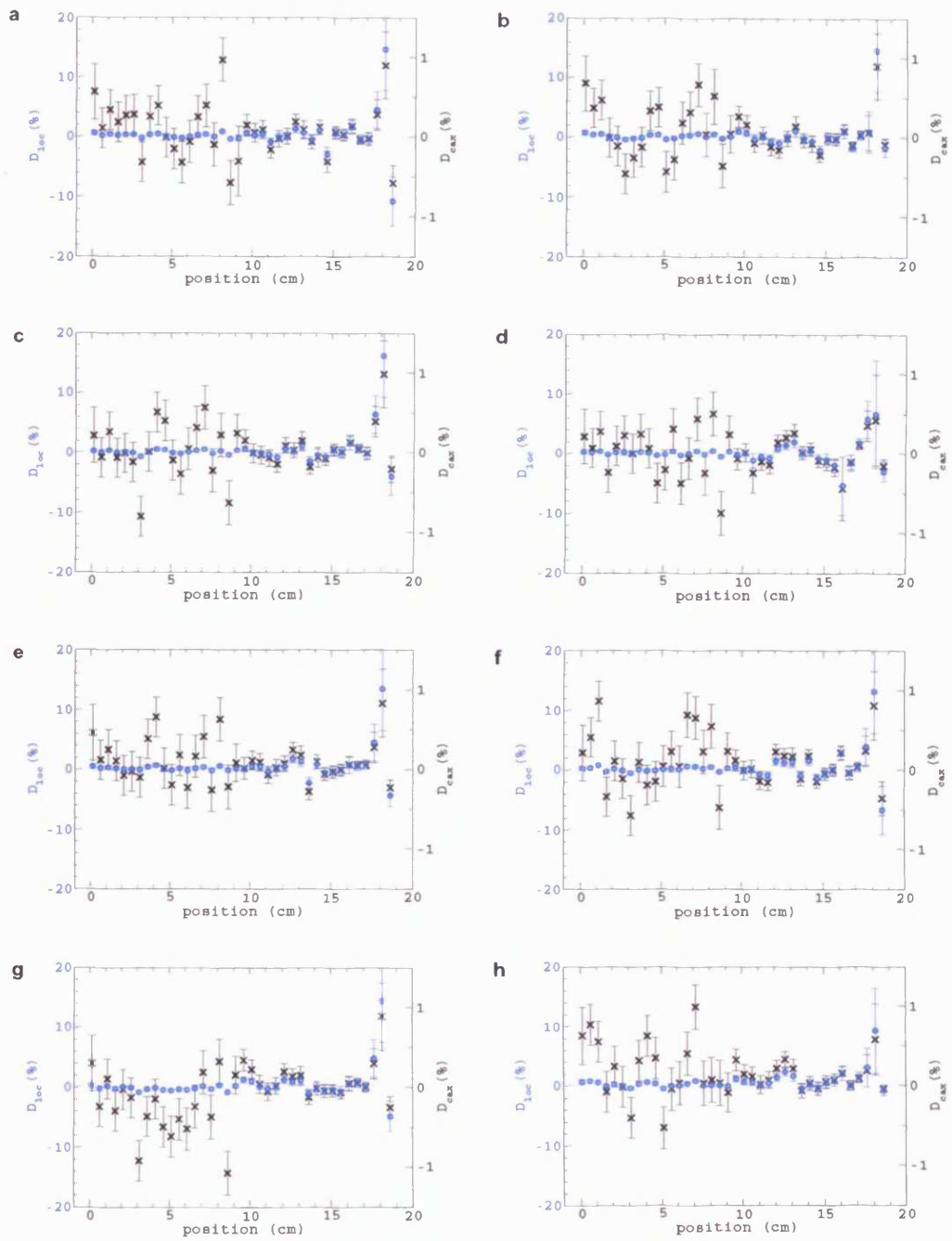

Figure 6.11: Effects of transport options on the SLIC EPID calculated as D_{loc} (blue circles) and D_{cax} (black crosses): a) bound Compton scattering; b) electron boundary crossing; c) pair production angular sampling; d) photoelectron angular sampling; e) bremsstrahlung angular sampling; f) atomic relaxation; g) spin effects and h) global electron cutoff.

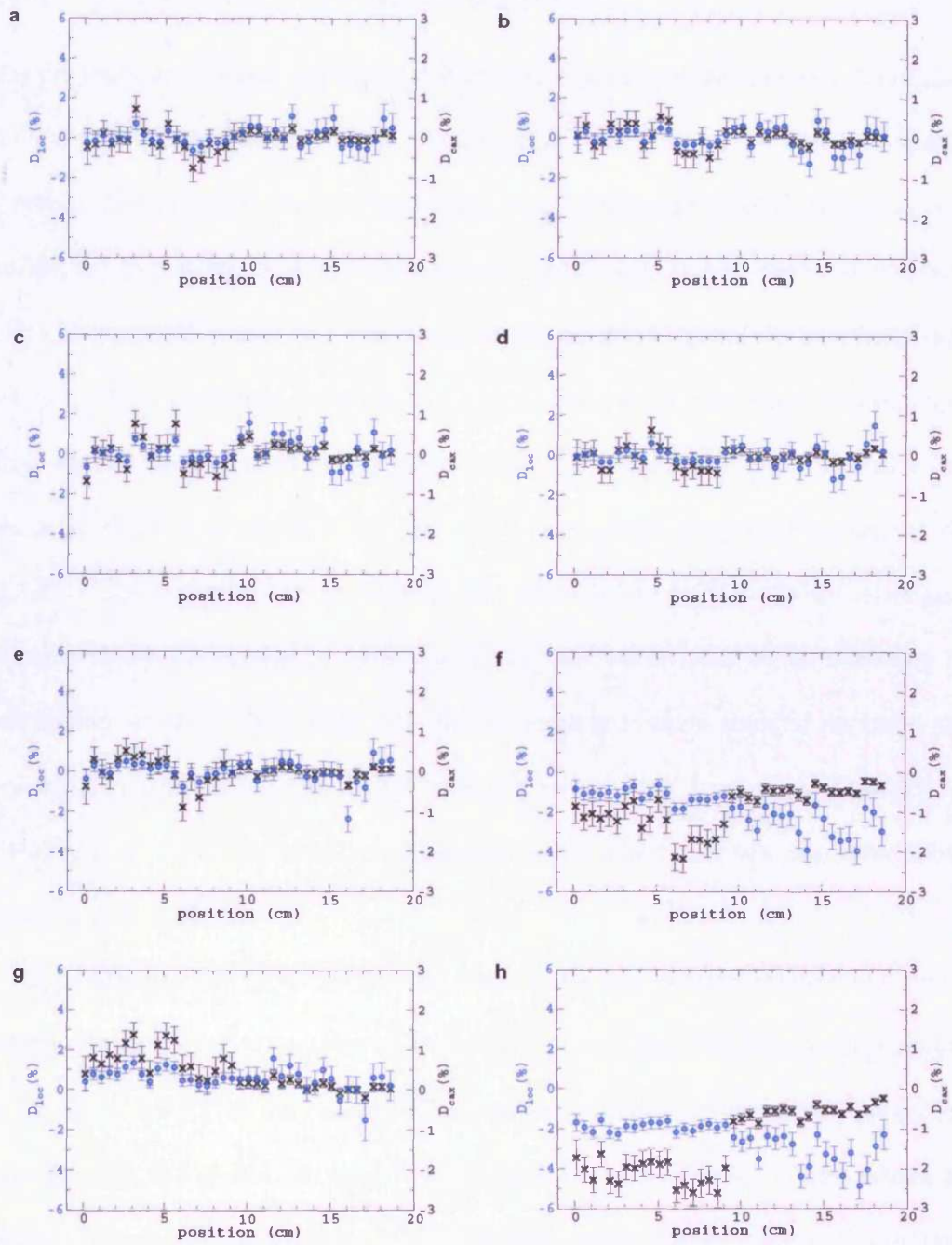

Figure 6.12: Effects of transport options on the a-Si EPID calculated as D_{loc} (blue circles) and D_{cax} (black crosses): a) bound Compton scattering; b) electron boundary crossing; c) pair production angular sampling; d) photoelectron angular sampling; e) bremsstrahlung angular sampling; f) atomic relaxation; g) spin effects and h) global electron cutoff.

6.3.3 Selection of Transport Options

For the transport options tested, no statistically significant difference was discernible for the SLIC model (Figure 6.11). Overall, D_{cax} was within 1%. The a-Si model, however, demonstrated obvious bias (Figure 6.12) when 1) atomic relaxation was turned on: D_{loc} up to 4%, portal dose was over-estimated; 2) spin effects were turned off D_{loc}: over 1.5%, portal dose was under-estimated; and 3) global electron cutoff was set to 0.7 MeV (rest mass included): D_{loc} up to 5%, portal dose was over-estimated. D_{cax} nonetheless remained consistently within 3% in all cases. For simulations of the a-Si EPID, it is therefore recommended that atomic relaxation be turned on (DOSXYZnrc turns this off by default) and that caution be taken when exercising electron cutoffs. Interestingly, Munro and Mulligan [2002] reported no reduction in calculation accuracy when both AE (below which secondary charged particles are not explicitly simulated) and ECUT were set to 0.7 MeV (rest mass included) in simulation of the EC-L cassette. Conditions under which this test was done were, however, not reported.

For both a-Si and SLIC EPIDs, no statistically significant difference was found whether or not Koch-Motz angular sampling was switched ON. This is understood to be partly due to the insignificant contribution of bremsstrahlung events to energy deposition in the EPIDs. In theory, Koch-Motz angular sampling is understood to be more accurate at energies above radiotherapy range; however, since it is derived from extreme relativistic approximations, its relevance at the radiotherapy range of energies is unclear [Kawrakow and Rogers 2002].

6.3.4 Comparison with Other Techniques

Figure 6.13 compares dose profiles from the a-Si EPID and those from a water-slab EPID. D_{cax} up to 10% were found. For square fields of side 20 cm, the water-slab EPID 1) underestimated off-axis portal dose for open fields; 2) overestimated off-axis portal dose in the field, but underestimated portal dose in the umbra, when a water phantom was place in the beam. No improvement was found even when an extra buildup layer was added to the cassette cover of the complete a-Si model. Our MC investigation confirms results from ion chamber measurements that the a-Si is not water-equivalent [El-Mohri et al. 1999]. Discrepancies were found to be worse at large field sizes (Figure 6.13) – which might explain the 'field size dependency' reported in work assuming water equivalence of the EPID [Grein et al. 2002, Greer and Popescu 2003].

Figure 6.14 compares dose profiles from a SLIC EPID and those from a water-slab EPID. D_{loc} was high (in some cases exceeding 80%) except for irradiation condition 4, where a water phantom was placed in the beam. Departure of the SLIC EPID from water-equivalence has also been suggested from measurements by Essers et al. [1996] and Chang et al. [2001]. Keller et al. [1998] found large absolute differences when comparing dose spread kernels (integrated over the entire portal dose plane) calculated for the SLIC EPID and for water. However, Figure 6.14 also shows that D_{cax} was within 3%. Depending on the tolerance, it is thus the choice of the informed user whether the representation of the SLIC EPID by a water slab is acceptable.

Results of tests on water-slab EPID models are summarised in Figure 6.15, where

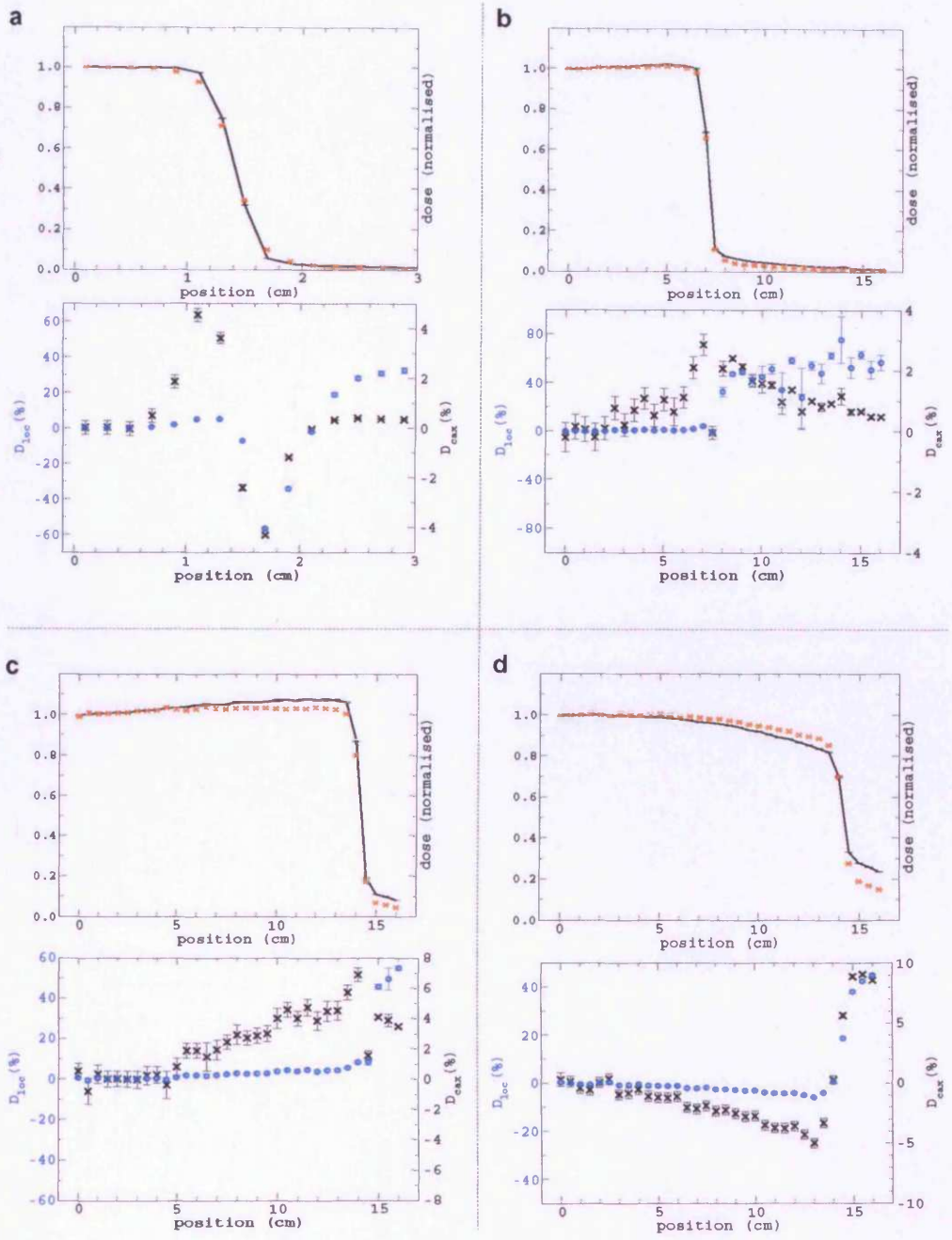

Figure 6.13: a-Si EPID (black lines) versus water-slab EPID (red crosses): dose profiles and corresponding differences when the EPID was irradiated by a a) 2 cm × 2 cm open field; b) 10 cm × 10 cm open field; c) 20 cm × 20 cm open field; and d) 20 cm × 20 cm field, water phantom in the field.

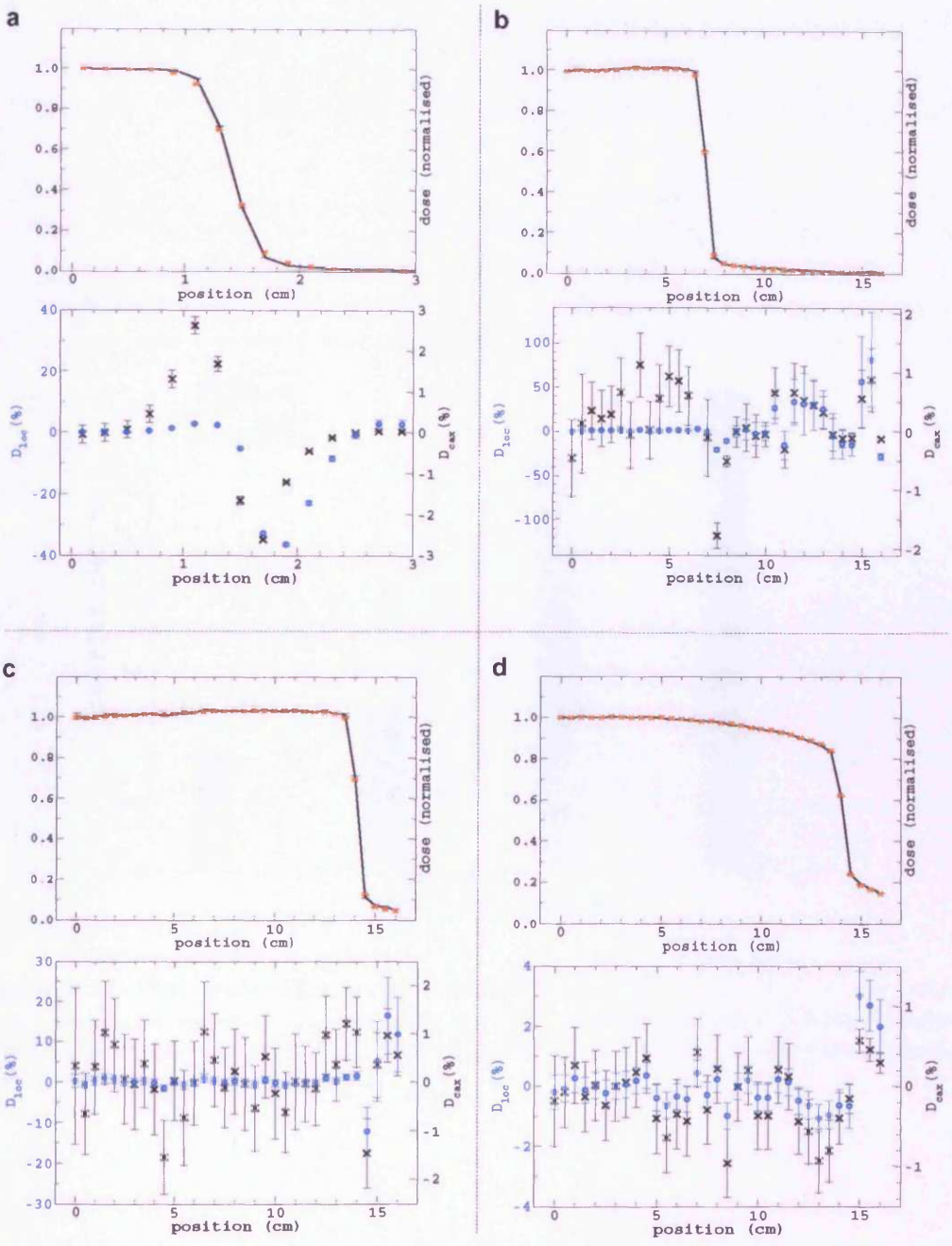

Figure 6.14: SLIC EPID (black lines) versus water-slab EPID (red crosses): dose profiles and corresponding differences when each EPID model was irradiated by a a) 2 cm × 2 cm open field; b) 10 cm × 10 cm open field; c) 20 cm × 20 cm open field; and d) 20 cm × 20 cm field, water phantom in the field.

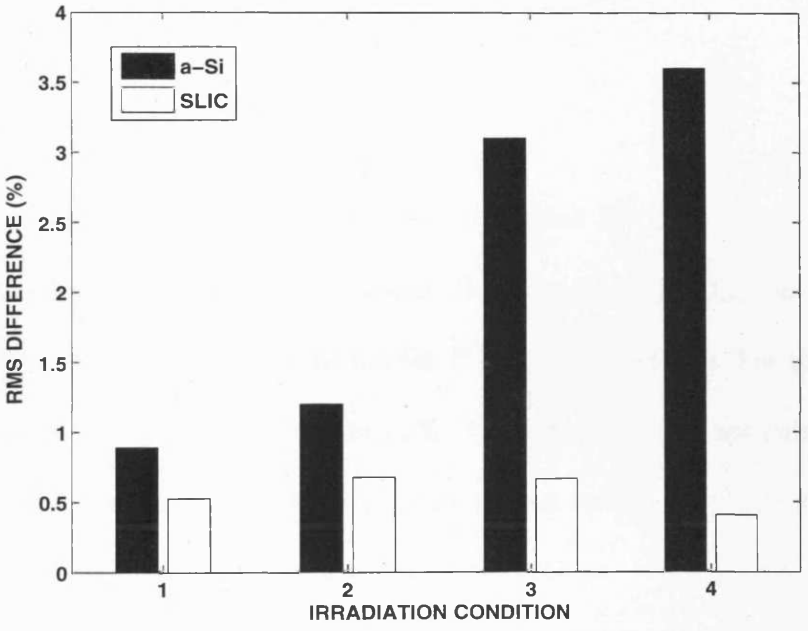

Figure 6.15: Water-slab EPID models compared to the full a-Si and SLIC models respectively: root-mean-square of the differences under irradiation conditions 1 (2 cm-side square field), 2 (10 cm-side square field), 3 (20 cm-side square field) and 4 (20 cm-side square field with a water phantom in the beam).

the root-mean-square of the difference (from the full models) with respect to the central axis value is plotted. Compared to the SLIC EPID, radiation properties of the a-Si EPID are less water-equivalent – as expected due to the presence of phosphor, a high-atomic-number material. For the SLIC and a-Si EPIDs, the highest-Z element present are strontium (Z = 38, in plastoferrite) and gadolinium (Z = 64, in phosphor screen) respectively.

6.4 Conclusions

For each of the a-Si and the SLIC EPIDs, simplified EPID models for dosimetric computation have been designed and tested. For the a-Si EPID, D_{cax} was consistently within 1.5% and 1.0% for simplified models B and C respectively. For the simplified SLIC model, D_{cax} was generally within 1.5%. The simpler models not only reduce MC simulation run time, but may be adopted as a more realistic model (e.g. compared to a homogeneous water slab) for non-MC computations.

The effects of transport settings on portal image prediction have been investigated for both the a-Si and the SLIC EPIDs. Whereas the SLIC EPID was found to be insensitive to such effects under the irradiation conditions tested, the a-Si EPID showed 4%, 1.5% and 5% of D_{loc} respectively when simulation of atomic relaxation was turned on, when simulation of spin effects was turned off, and when electron cutoff energy was set to 0.7 MeV (rest mass included). It should be noted that DOSXYZnrc turns off atomic relaxation by default.

The assumption of water-equivalence of EPIDs, characteristic of many non-MC

portal dosimetry techniques, was found to produce D_{cax} up to 10% and 3% for the a-Si and SLIC EPIDs respectively. Our findings underscore the role of, and the need for, MC radiation transport in radiotherapy portal dosimetric calculation.

Chapter 7

PRACTICAL ASPECTS OF PORTAL IMAGE ACQUISITION

The treatment verification solution presented in Chapter 5 works by comparing dose maps obtained from Monte Carlo (MC) simulations with dose maps derived from physically acquired portal images. Chapter 4 has already reported the optimisation of the former. This chapter focuses on the optimisation of the latter.

Accurate derivation of dose information from image pixel values relies on the detector (e.g. dose response and discharge characteristics) as well as the acquisition system (e.g. readout and sequencing with respect to the beam.) Problems, solutions and alternatives in the practical aspects of portal image acquisition for IMRT dose verification will be reported. An alternative imaging sequence which overcomes the problems identified will be proposed. A new way of interpreting portal images, incorporating both spatial and temporal information, will also be proposed. The idea takes advantage of features commonly seen as limitations: *ghosting** (often seen as unwanted signals), and row-by-row image scanning (often seen as a delay).

* *Ghosting* will be explained in Section 7.2.4.2.

7.1 Introduction

As mentioned in Chapter 5, the response of scanning liquid ionisation chamber (SLIC) electronic portal imaging devices (EPIDs) varies with gantry angle, causing an artefact commonly known as the *bulging effect*. A comprehensive study of this effect will be presented, along with a rigorously tested correction algorithm developed by the author.

This chapter also investigates the prospects of the Varian aS500 amorphous silicon (a-Si) EPID as a dosemeter. Some unexpected problems suggest that the use of this device for IMRT dose verification should await further developments from the manufacturer (Section 7.2.2 and Section 7.2.3).

By proposing an alternative imaging sequence which overcomes the present limitations, Section 7.2.4 attempts to address the clinical need for verifying IMRT beams. Section 7.3.4.2 suggests that since it is hard to avoid ghosting in portal images, we might as well make use of it, by incorporating both spatial and temporal information in image interpretation. Illustrative examples will be given.

7.2 Materials & Methods

We used a Varian PortalVision Mk2 SLIC EPID installed locally at Velindre Cancer Centre. It produces portal images of 256×256 pixels, where each square pixel has dimension 1.27 mm, giving a 32.5 cm × 32.5 cm imaging area.

Since an a-Si EPID was not available at Velindre Cancer Centre during the ma-

jority of this project,* experiments on the a-Si EPID were carried out on the Varian PortalVision aS500 model at two of our collaborating institutions: Virginia Commonwealth University (USA) and the Institute of Cancer Research / Royal Marsden Hospital (UK). The aS500 produces portal images of 512×384 pixels. Each square pixel has dimension 0.78 mm, giving a 40.0 cm × 30.0 cm imaging area.

7.2.1 The SLIC: Variation with Gantry Angles

The gantry of a linear accelerator (linac) is rotated when various beam delivery angles are required. As the linac head rotates around the isocentre, so does the diametrically opposed EPID. When attenuation and scatter conditions are unchanged, fluence incident on the EPID and therefore the EPID's response should ideally be invariant with gantry angle. In practice, however, images taken at various gantry angles are not identical due to several gantry-dependent factors as detailed below:

1. **Change in radiation output exiting the linac head.** This contributes little effect. Whereas the recommended tolerance is 2% [Mayles et al. 1999], local quality control experience indicates that linac output changes by no more than 1% with gantry angle [Gray 2003].

2. **Imperfect mechanical rigidity of the support arm.** This may cause vertical, longitudinal and lateral shifts of the imager with respect to the isocentre. The inverse square relation indicates that at *SDD*† 140 cm, a 1.2 cm decrease in vertical position may cause a 1.7% increase in fluence incident on the detector.

*Three a-Si EPIDs were installed and commissioned at Velindre Cancer Centre in March 2005.
†The *SDD* has been defined in Figure 2.6.

3. **Change in response of the EPID.** This factor, known colloquially as the bulging effect, is the dominant factor. Change in detector response due to cassette orientation is a known behaviour of the SLIC EPID [van Herk and Meertens 1988, Roback and Gerbi 1995]. The image detector unit contains an ionisation chamber filled with iso-octane*. Since the cassette which contains the liquid is not entirely rigid, the two plates of the ionisation chamber flex as the gantry rotates, causing non-uniform thickness of the liquid film. This artefact, visible as alternately dark and bright oval areas on *open field*† images (Figure 7.1), introduces asymmetry to an otherwise flat radiation profile.

4. **Scatter from surrounding structures such as floor, walls and ceiling.** At gantry angles of 0° and 180°, the separation between the imager and the floor/ceiling can be very small, potentially allowing backscattered radiation to reach the detector. The extent of the effect also depends on the construction materials used.

The latter three factors will be considered in this work.

Image acquisition was carried out in multiple sessions at 2-week intervals. The dataset of images from each session was labelled as follows:

- Dataset $\triangle_{10}$: images acquired at every 10° gantry angle. Image calibration was updated at the start of the session.

- Dataset $\triangle_{30}$: images acquired at every 30° gantry angle. Image calibration was

*The iso-octane has been introduced in Section 2.3.
†The *open field* has been defined in Section 6.2.2.

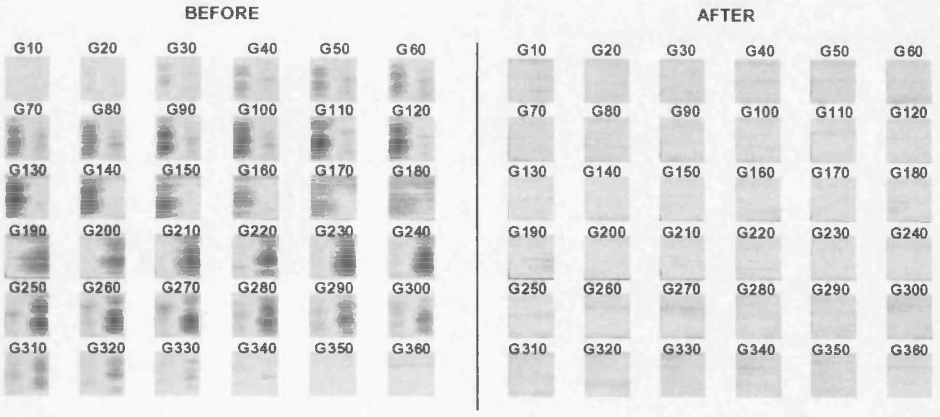

Figure 7.1: Images, acquired at various gantry angles, before and after correction using the technique devised in Section 7.2.1.4. Corresponding gantry angles are labelled. A common grayscale window has been used for all images.

updated at the start of the session.

- Dataset $\triangle_{90}$: images acquired at gantry angles of 0°, 90°, 180° and 270°. Image calibration specific to each gantry angle was obtained by updating the calibration each time the gantry was rotated.

For all datasets, the EPID, irradiated by a 6 MV 25 cm × 25 cm open field, was positioned at SDD 140 cm. To protect radiation-sensitive electronics on the imager, this was deemed the maximum field size at SDD 140 cm. The centre of the imaging area was aligned to the isocentre in longitudinal and lateral directions. Dose-rate was allowed to stabilise before acquisition began. Dataset $\triangle_{10}$ was used to describe gantry dependence of images and to derive a new correction function, whose applicability was demonstrated using dataset $\triangle_{30}$. Dataset $\triangle_{90}$ was used to investigate image calibration specific to cardinal gantry angle.

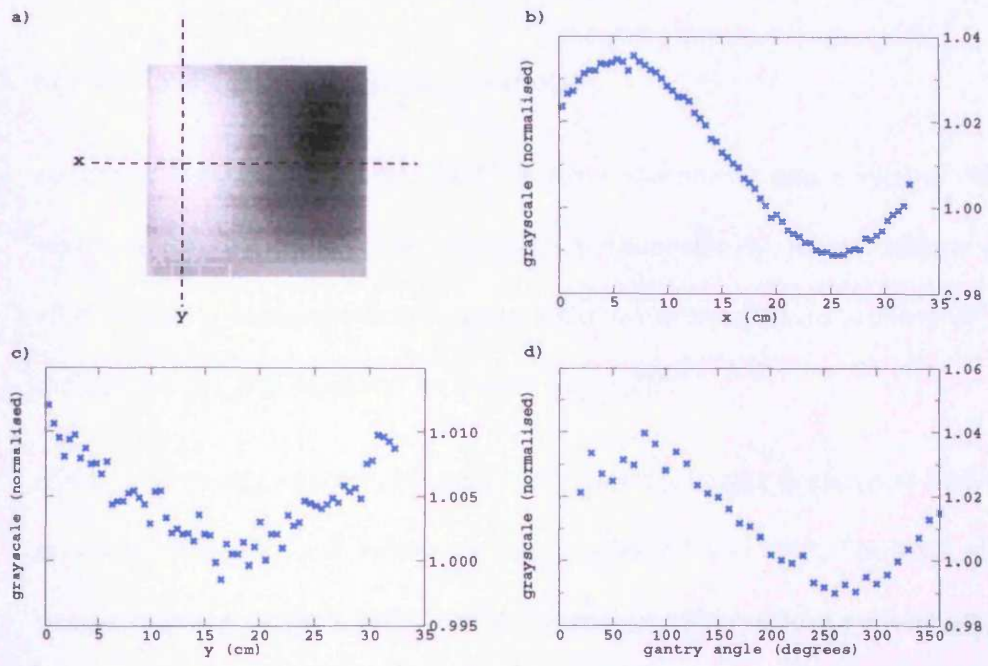

Figure 7.2: a) A portal image with x and y axes defined; b) pixel values along the central x axis; c) pixel values along the central y axis; d) pixel values of a fixed point at various gantry angles. Pixel values have been normalised to C_0.

Each image of 256 x 256 pixels will be denoted $\mathbf{I}_\gamma$ where γ is the gantry angle at which the image was acquired. Value on each pixel is denoted $P_{\gamma,x,y}$, and the pixel value averaged over 10×10 pixels around the central axis (CAX) is denoted C_γ. C_0 is the C_γ value when γ is zero. x and y are the coordinates of the pixel in the *LR* and *GT* directions* as defined in Figure 7.2a.

7.2.1.1 Angular Dependence of Images

$\mathbf{I}_\gamma$ from the datasets were analysed for:

1. variation of central axis pixel value (C_γ) with gantry angle.

LR for "Left-Right", also known as *crossplane*. *GT* for "Gun-Target", also known as *inplane*.

2. 2D variation of images ($\mathbf{I}_\gamma$) with gantry angle.

3. reproducibility of $\mathbf{I}_0$ after gantry rotation(s).

4. settling of the liquid once the SLIC cassette was moved into a vertical orientation, by comparing $\mathbf{I}_{90}$ taken successively (immediately, after $\frac{1}{2}$ minute and after another $\frac{1}{2}$ minute) once the gantry had been rotated into position 90°. A similar exercise was repeated for gantry angle 270°.

5. effects from gantry rotation, by comparing three $\mathbf{I}_{90}$ images acquired at repeated rotations back and forth between gantry angles 90° and 270°. Similarly, three images at gantry angle of 270° acquired after repeated rotations were compared.

Where images were compared, each local pixel value from the first image ($\mathbf{A}$) and its counterpart from the second image ($\mathbf{B}$) were used for element-by-element calculation of the expression

$$\mathbf{D} = \frac{\mathbf{A} - \mathbf{B}}{\frac{1}{2}(\mathbf{A} + \mathbf{B})} \tag{7.1}$$

7.2.1.2 Backscatter from Surroundings

To check effects due to backscatter from surrounding structures, a MC model was built, using manufacturer-specified and directly measured data, to represent the turntable on the floor of a linac installation. The SLIC EPID was modelled as previously reported [Spezi and Lewis 2002]. Irradiation of a 6 MV 25 cm × 25 cm beam was simulated with DOSXYZnrc using default transport parameters. This was followed by another simulation without the floor structures. Doses deposited on the

*active detection layer** from the two simulations were compared.

7.2.1.3 Reproducibility

Reproducibility of the EPID signal over time was monitored in two ways:

1. reproducibility of $\mathbf{I}_0$, by inter-comparison from four different sessions at approximately monthly intervals.

2. reproducibility of images acquired at every 30° gantry angle. Images from $\triangle_{10}$ and $\triangle_{30}$ were compared. Each image was normalised to C_0 of the respective dataset.

Monitoring of reproducibility was to ensure that the same angular correction can be applied over different sessions. It was not of interest to find out how long a calibration could last before significant deviation. This has already been thoroughly studied elsewhere [Essers et al. 1996, Louwe et al. 2004]. For accurate dosimetry (as demonstrated in Section 5.3.1.1), it is our practice to perform image calibration at the start of each session.

7.2.1.4 Angular Correction Function

If left uncorrected, image dependence on gantry angle can potentially lead to significant errors in dosimetric verification. Our aim was to correct not only for variation along the x direction [Evans et al. 1999], but also variation along the y direction (not accounted for in previous work). x and y are as defined in Section 5.2 and Figure 7.2a.

*The *active detection layer* is the layer containing iso-octane.

Images from the datasets indicated that a simple sinusoidal trend could not fully characterise the angular variation. A model providing a better fit to the data was found to be:

$$Q(x, y, \gamma) = I \sin(Ax + B) \sin(Cy + D) \sin(E\gamma) + J \sin(F\gamma + H) + K \qquad (7.2)$$

where γ is the gantry angle at which the image was acquired, A, B, C, D, E, F, H, J and K are coefficients to be derived empirically. Whereas the first term on the right-hand side of Equation (7.2) describes the pixel-by-pixel variation with gantry angle, the second accounts for sag due to non-rigidity of the support arm. The third is an offset term.

Based on $\mathbf{I}_\gamma$ of dataset $\triangle_{10}$, images were downsampled from 256×256 pixels to 64×64 pixels. The downsampled images formed a dataset of 4 variables: x, y, γ and $\mathrm{P}_{\gamma,x,y}$. This dataset served as input for nonlinear regression. Three *independent variables** were assigned: x, y and γ. The aim of the correction function was to return C_0, which is typically used for central-axis grayscale-to-dose calibration in portal dosimetry [Spezi and Lewis 2002]. Therefore, the *dependent variable*† for the regression was assigned the ratio of C_0 to $\mathrm{P}_{\gamma,x,y}$. By applying the modified Levenberg-Marquardt algorithm proposed by More [1977], the SPSS‡ nonlinear regression module was used to produce least square estimates of the coefficients. Regression produced coefficients required by the function $Q(x, y, \gamma)$. An image requiring correction would have its grayscale values multiplied by the corresponding value from $Q(x, y, \gamma)$, producing the

**Independent variables* are sometimes known as the *explanatory variables*.
†*Dependent variables* are sometimes known as the *outcome variables*.
‡Statistical analysis software. The website is at www.spss.com.

corrected image.

7.2.1.5 Comparison with Existing Techniques

Correction using the sinusoidal modulation technique devised herein (Equation (7.2)) was compared with two existing techniques:

1. gantry-dependent *flood field** (FF) correction [van Esch et al. 2001], where the *FF* in the standard calibration protocol is replaced by one which is gantry-dependent:

$$FF(\gamma) = \frac{FF_0 + FF_{90} + FF_{180} + FF_{270}}{4} + \sin(\gamma)\frac{FF_{90} - FF_{270}}{2} \tag{7.3}$$

where γ is the gantry angle and the subscripts indicate the gantry angle at which the FF was acquired. *FF(γ)*, derived from dataset $\triangle_{90}$, replaces *FF* in the standard image calibration such that

$$J = \frac{J_o - DF}{FF(\gamma)}\, k \tag{7.4}$$

where J_o and J are the images before and after calibration, k is the scalar mean of all values in *FF(γ)*. Division is element-by-element.

2. correction based on profile averaging [Evans et al. 1999]. For each image in dataset $\triangle_{10}$, x-profiles were averaged to obtain an x-profile representative of the respective gantry angle. The ratio of the representative x-profile for $\mathbf{I}_\gamma$ to that of $\mathbf{I}_0$ is applied as the correction factor.

*The *flood field* has been defined in Section 5.2.1.1.

In the text that follows, the gantry-dependent FF, profile averaging and sinusoidal modulation techniques will be referred to as the first, second and third techniques respectively.

Each technique was used to correct images from dataset $\triangle_{30}$, which was not used to derive any of the correction coefficients. The intent was to test the techniques on images of a different session, since a technique that does not require frequent regeneration of correction coefficients was desired.

Correction coefficients of the latter two techniques were derived using images at every 10°. Additionally, to investigate the sensitivity of correction coefficients to angular resolution, coefficients were also generated using images at every 30°.

7.2.1.6 Application of the New Technique

Next, the sinusoidal correction technique was used to correct images of a 10 cm × 10 cm open field as an alternative to the 25 cm × 25 cm field described earlier, at various gantry angles. A scaling factor was applied to account for the change in output factor due to field size. This would not be required in MC portal dosimetry where the change in output would have been intrinsically accounted for (Chapter 5).

Images before and after correction were analysed for symmetry along the x-direction. The region of interest was defined as 80% of the beam size. Profiles were averaged over 10 pixels in the y direction. Difference of each pixel value P_x from its counterpart P_{-x} on the opposite side of the CAX was calculated as

$$d = \frac{P_x - P_{-x}}{\frac{1}{2}(P_x + P_{-x})} \tag{7.5}$$

7.2.2 The a-Si: an Artefact in the IMRT Acquisition Mode

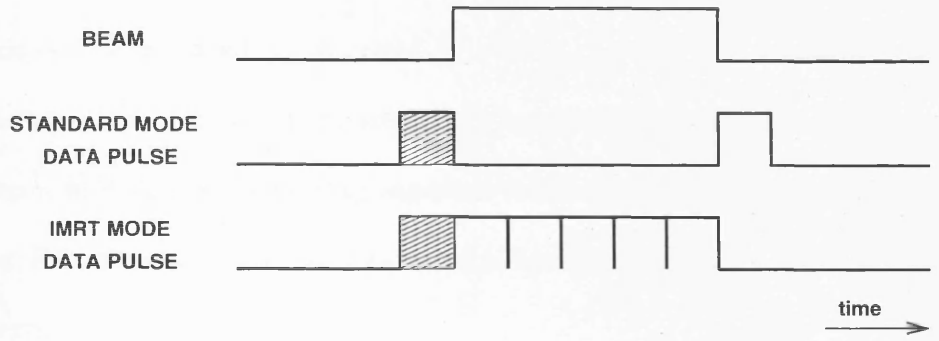

Figure 7.3: The *standard* and the *IMRT* image acquisition modes: timing of data pulses with respect to the beam. Shaded pulse is the *refresh cycle*.

Figure 7.3 shows the two imaging modes available in the PortalVision aS500 system: the *standard* and the *IMRT* modes. For both modes, a few frames are read out before the start of irradiation to eliminate any dark current or residual data. This process is sometimes called *refresh cycle*, *reset*, *forced discharge* or *blanking*. In the standard mode, no readout occurs during beam-on. Readout occurs only after irradiation. By not capturing image frames between/during linac pulses, this mode avoids linac pulsing artefacts. It is, however, not suitable for imaging over the entire duration of a beam because the frame buffer would saturate. Imaging over the entire duration of a beam attempts to use the EPID as an integrating dosemeter – which is commonly accepted by the EPID community as the way to verify IMRT beams. (The author proposes an alternative method in Section 7.2.4.1.)

To overcome the problem due to frame buffer saturation, the manufacturer introduced the IMRT mode. By allowing periodic transfer of data from the frame buffer to another storage, readout can occur continuously during irradiation without saturat-

ing the buffer. To minimise pulsing artefacts, multiple frames are averaged to form a final image. A point to note is that on the current Varian PortalVision system, individual frames cannot be recovered.

As a first step in testing the usability of the aS500 EPID as an integrating dosemeter, open field images for varying exposure duration were acquired using the IMRT mode. Prior to that, DF/FF calibration* had been updated at the same SDD without any extra buildup.

7.2.3 The a-Si: Variation with Gantry Angles

Whereas SLIC EPIDs are known to produce gantry-dependent artefacts (Section 7.2.1), a-Si EPIDs are generally believed to be gantry-invariant. Putting aside such presumptions, this section subjected the aS500 EPID to tests similar to those done for the SLIC EPID (Section 7.2.1). Open field images were acquired at various gantry angles. These images were later examined for any systematic difference.

7.2.4 Ideas for IMRT Verification

7.2.4.1 An Alternative Imaging Sequence

Of the two modes available in the Varian PortalVision acquisition system (Section 7.2.2), neither is suitable for verifying IMRT beams. Whereas the standard mode saturates before the beam finishes, the IMRT mode leads to the artefacts described in Section 7.3.2. Additionally, assuming and using the EPID as an integrating or cu-

*The DF/FF calibration has been introduced in Section 5.2.1.1.

mulative dosemeter tends to result in ghosting (Section 7.3.4.2) and missing frames* [Chang and Ling 2003] problems, which overestimate and underestimate dose delivery respectively. Such limitations are not surprising since EPIDs are generally designed to measure transient dose distributions, not cumulative doses.

The author therefore proposes an alternative imaging sequence, where strategically-timed image acquisition verifies both the multileaf collimator (MLC) leaf positioning as well as the exposure duration (thereby accomplishing both geometric and dosimetric verifications), while avoiding the problems discussed in the previous paragraph.

7.2.4.2 Rethinking Ghosts

Ghosting, *memory effect* and *after-glow* are among the terms commonly used, somewhat interchangeably, to describe increased pixel values due to a previous irradiation. In fact this effect may be categorised into two types:

- a temporary increase in sensitivity due to a prior irradiation; or
- incomplete discharge where a reading already counted for the previous frame/ image gets counted again.

The extent of ghosting on the Elekta a-Si EPID has been thoroughly studied by McDermott et al. [2004]. Section 7.3.4.2 will show:

- a quantitative example of ghosting on the Varian a-Si EPID, where a maximum open field was imaged 75 seconds after imaging a 5 cm $\times$ 5 cm field. A shorter

*Frame acquisition is temporarily suspended each time data transfer for clearing the buffer occurs.

delay was difficult to obtain since time was required for changing the field size; and

- a qualitative example of ghosting on the Varian SLIC EPID, where successive images were acquired during a *step-and-shoot** IMRT beam.

Whereas ghosting is often regarded as a problem, the author proposes a rethink. In fact, images may be interpreted by incorporating both spatial and temporal information, based on the fact that:

- a portal image contains information about both the past and the present; and
- each image is formed by row-by-row readout or scanning, as opposed to instantaneous snapshots in film-based cameras.

These ideas will be expanded in detail in Section 7.3.4.2.

7.3 Results & Discussion

7.3.1 The SLIC: Variation with Gantry Angles

7.3.1.1 Angular Dependence of Images

When we examined the variation of the central axis pixel value (C_γ) with gantry angle, a steady increase up to 1.5% was found as the gantry angle approached 180° (Figure 7.4). 2D images ($\mathbf{I}_\gamma$) varied significantly with gantry angle. Such artefacts

*In a *step-and-shoot* radiation delivery, leaves do not move while the beam is on. Beamlets or segments depicted in Figure 1.2 are delivered discontinuously; the beam is switched off during transition from one beamlet to the next to allow rearrangement of leaves.

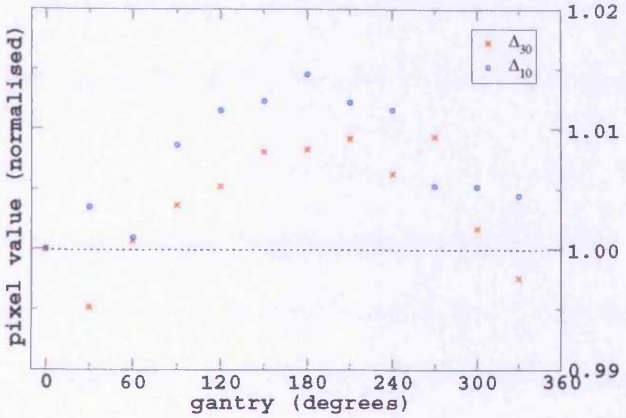

Figure 7.4: Variation of C_γ (normalised to C_0) with gantry angle, shown for datasets $\triangle_{10}$ and $\triangle_{30}$ (as defined in Section 7.2.1).

were most evident around regions of gantry angles 90° and 270°. Pixel values differed from C_0 by up to 5%. The artefacts were visible as alternate dark and bright oval areas on an image (Figure 7.1). Location of the dark and bright oval areas was reversed on images between 90° and 270°.

When compared pixel-to-pixel using Equation (7.1), $\mathbf{I}_0$ was reproducible within 2% when returned to position after gantry rotation(s). Effects from liquid settling were well below 2%. $\mathbf{I}_{90}$ and $\mathbf{I}_{270}$ were reproducible within 2% after successive gantry rotations.

7.3.1.2 Backscatter from Surroundings

Results from MC simulation with and without the floor structure differed by a maximum of 3% within the field. These differences were wholly attributable to statistical uncertainty in the simulations.

7.3.1.3 Reproducibility

Figure 7.5 shows the cumulative histograms for **D** calculated using Equation (7.1):

1. $\mathbf{I}_0$ data from four sessions were compared pixel to pixel. Direct comparison found differences up to 5%. Temperature dependence could be a contributing factor, since a 1% change in detector response per °C may be expected [Louwe et al. 2004]. When each image was normalised to C_0 of the respective session, reproducibility was well within 2%.

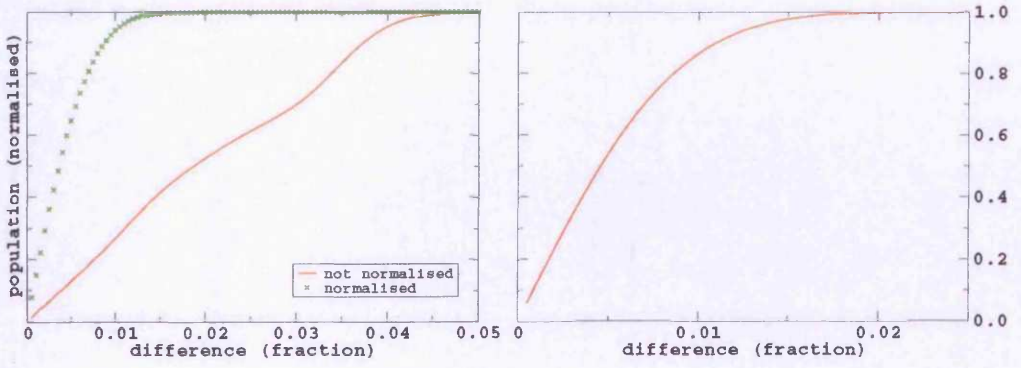

Figure 7.5: Cumulative histograms of **D**. Left: reproducibility of $\mathbf{I}_0$ with and without normalisation to C_0 of the respective session. Right: reproducibility of images at every 30° gantry angle.

2. Reproducibility of images at every 30° gantry angle was checked by comparing respective images from $\triangle_{10}$ and $\triangle_{30}$. Agreement was within 2% (Figure 7.5).

7.3.1.4 Angular Correction Function

Nonlinear regression using SPSS yielded the coefficients A=-0.1603 cm^{-1}, B=2.640, C=-0.07938 cm^{-1}, D=3.041, E=0.01767 degrees^{-1}, F=.01942 degrees^{-1}, H=1.239,

I=-0.01973, J=.005706 and K=0.9921. The square of the correlation coefficient was 0.8 i.e. the regression model successfully described 80% of the variation in the *dependent variable*.

7.3.1.5 Comparison with Existing Techniques

Images corrected using independent techniques (gantry-dependent FF, profile averaging and sinusoidal modulation) were calculated for uniformity using Equation (5.1). Standard deviations of uniformity were 0.0081, 0.0061 and 0.0054 respectively. The sinusoidal modulation technique developed herein was found to be the most effective (Figure 7.6).

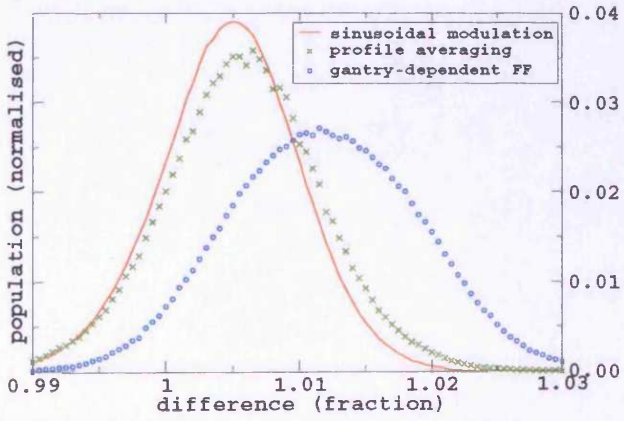

Figure 7.6: Histograms of uniformity to compare results of the sinusoidal modulation technique developed herein with existing techniques.

Image correction was repeated with reduced angular sampling of input images for coefficient derivation. For 30° sampling, standard deviations of uniformity remained unchanged. For 90° sampling, the standard deviations deteriorated to 0.0064 and 0.0059 for the second and third techniques respectively.

7.3.1.6 Application of the New Technique

Analysis of profiles before and after applying the sinusoidal modulation correction showed successful application on images of a 10 cm × 10 cm beam. Figure 7.7 shows the root-mean-square of the difference between each pixel value and its counterpart over the opposite side of the CAX. The difference for corrected images was under 0.5%.

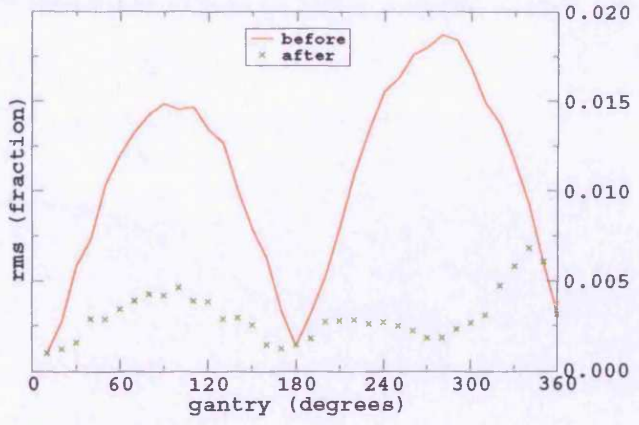

Figure 7.7: Root-mean-square of the difference between pixels from opposing sides of the profile.

7.3.2 The a-Si: an Artefact in the IMRT Acquisition Mode

Figure 7.8 shows an image with the associated profiles of a large open field acquired with the a-Si EPID. Systematic grayscale non-uniformity is obvious in both vertical and horizontal directions, where grayscale values differed by 2% – this is clearly not an image one would expect from a uniform beam. The anomaly was similarly observed at both Virginia Commonwealth University and Royal Marsden Hospital, ruling out

installation-dependent factors.

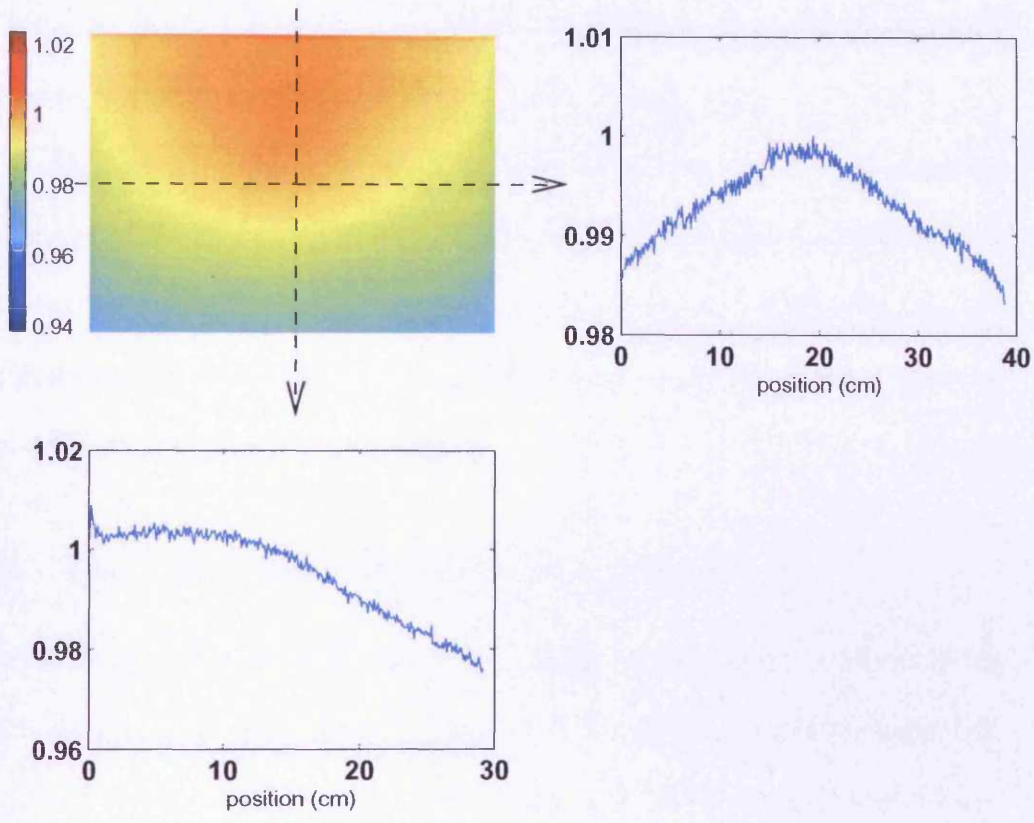

Figure 7.8: The IMRT mode on the aS500: an image and corresponding profiles of a large, uniform, open field. Pixel values (normalised to the value at CAX) differ by over 2%. DF/FF calibration was done with 60 frames; the image was acquired with 835 frames, corresponding to 400 MU.

Except when the same exposure duration was used for both DF/FF calibration and image acquisition, the anomaly was found in all the acquired images. Therefore, the use of the aS500 as an integrating dosemeter failed a basic test. If the device can't handle a square, uniform, static open field – there is no reason to believe it to be capable of handling irregular, intensity-modulated, dynamic fields. Although

there have been reports claiming success in the latter (without testing the former), e.g. van Esch et al. [2004], the author's understanding is that the anomalies must have been lost in the complexity tested, hence undetected. This problem has been reported to the EPID community [Chin and Lewis 2004].

The anomaly, which disappeared when the standard mode was used, is suspected to be effects of interplaying factors from processes such as readout, blanking and synchronisation. Private communication with the manufacturer suggested that the non-instantaneous, transistor-like discharge characteristics of the detector could be the cause.

7.3.3 The a-Si: Variation with Gantry Angles

When the images acquired at rotated gantry angles were examined, artefacts in the form of circular rings were visible. This was most evident at gantry angle 180° (Figure 7.9), where grayscale values on the "peaks" and "valleys" in the image differed by over 2%. This was once again observed at both Virginia Commonwealth University and Royal Marsden Hospital, ruling out individual installation-dependent factors.

After returning the gantry to angle 0° after the rotations, the image at gantry angle 0° could not be reproduced. Circular rings similar to that shown in Figure 7.9 were again visible. This raises concerns because it implies that for dosimetric work, one should not only avoid interpreting images acquired at non-zero gantry angles, but also images acquired at gantry angle 0° after gantry rotation(s). This is difficult in practice since almost all treatments involve gantry rotation(s).

The variation is not believed to be due to changes in detector response. It is believed to be due to displacements from calibration-time alignment of the EPID to the beam, causing the fluence incident on the detector to change. Circular features on Figure 7.9, which correspond to the profile of a *flattening filter**, suggest that the apparent position of the flattening filter (with respect to the EPID) during imaging has been shifted from that during flood field calibration.

The shift is believed to be due to non-rigidity of the EPID support arm. As the gantry was rotated, the EPID was found to shift in vertical, longitudinal and latitudinal directions. An image acquired after a deliberate shift was found to resemble Figure 7.9 qualitatively and quantitatively.

7.3.4 Ideas for IMRT Verification

7.3.4.1 An Alternative Imaging Sequence

The alternative imaging sequence proposed by the author is explained in Figure 7.10. Prior to irradiation and image acquisition, a sequence template would be programmed according to the treatment plan. The sequence template would then trigger an image acquisition at expected start and end of each segment. These are the vulnerable points where leaf transition takes place and where errors are likely to occur. Placement of checkpoints in this way would detect any premature or delayed transition.

For each segment, if we denote M_{TPS}, I_α and I_ω respectively as the dose map expected based on data from the treatment planning system, the image at the begin-

*The *flattening filter* has been introduced in Section 3.4.

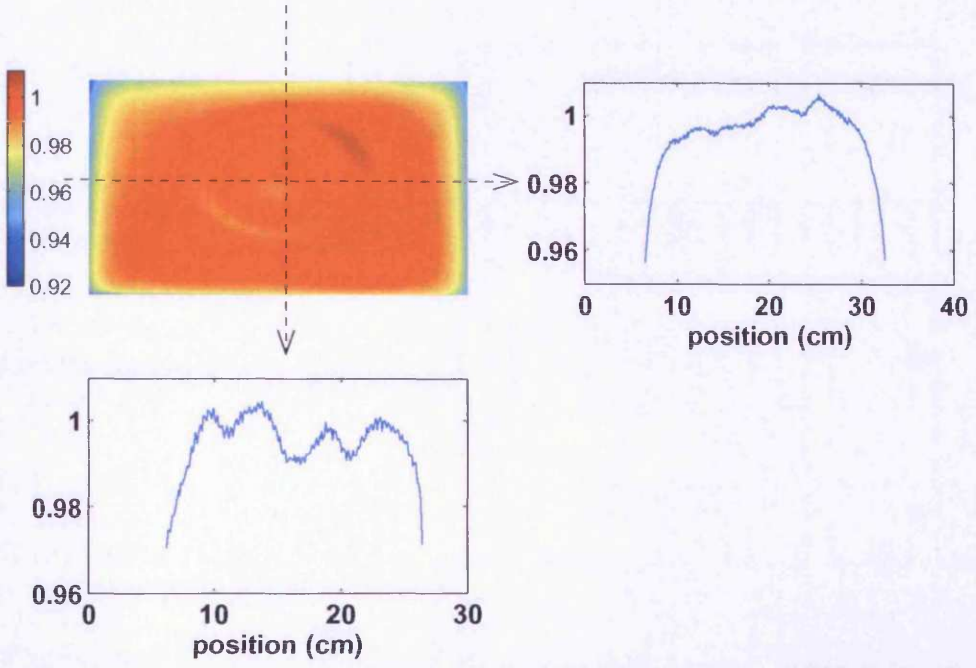

Figure 7.9: An a-Si portal image, and corresponding profiles, acquired at gantry angle 180°. Pixel values have been normalised to the value at CAX.

ning of the segment and the image at the end of the segment; T_α and T_ω respectively as the time at the beginning and the time at the end of the segment, the logic for analysis would be:

- if $I_\alpha = I_\omega = M_{TPS}$, delivery of the segment was correct geometrically between T_α and T_ω.

- else, if $I_\alpha = M_{TPS}$ but $I_\omega \neq M_{TPS}$, the segment finished too early;

- else, if $I_\alpha \neq M_{TPS}$ but $I_\omega = M_{TPS}$, the segment started too late;

- else, if $I_\alpha \neq M_{TPS}$ and $I_\omega \neq M_{TPS}$, the segment fails both geometric and dosimetric verifications.

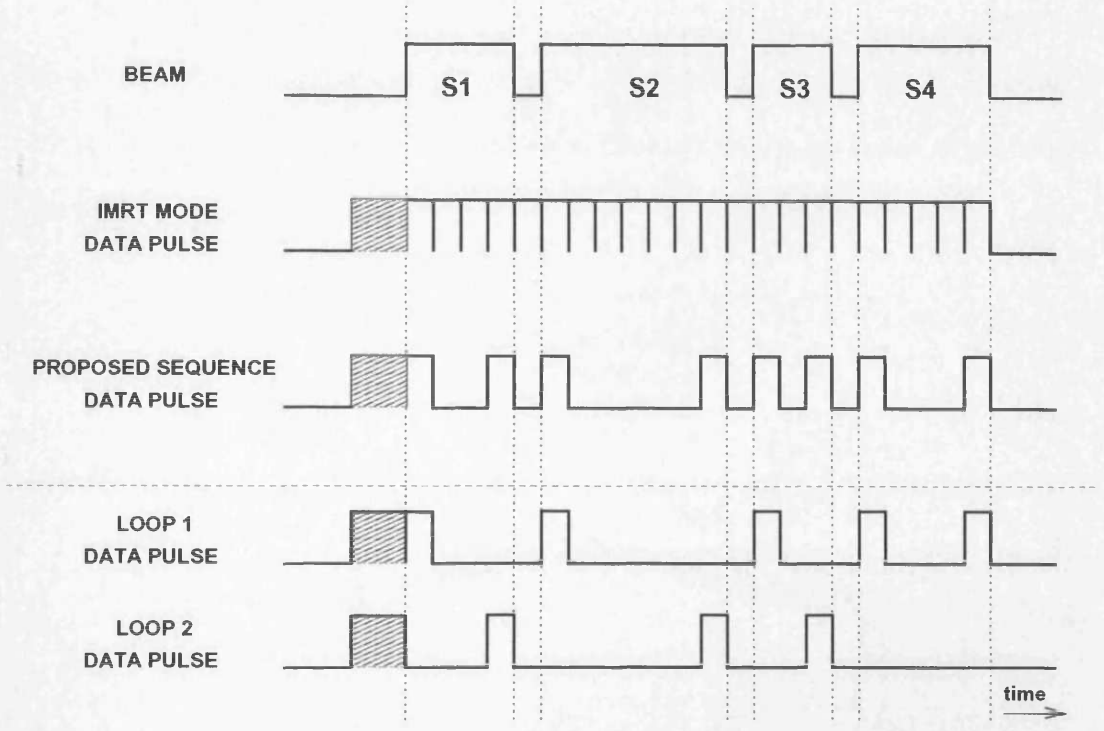

Figure 7.10: Proposed imaging sequence for verifying a step-and-shoot beam. Shown is a beam consisting 4 segments (S1 to S4).

The analysis assumes constant linac output and static leaves during each segment. For pre-treatment verification, to avoid successive image acquisition being timed too closely together (shorter than the EPID frame-rate or shorter than the ghost recovery period), beam irradiation may be repeated over several loops of image acquisition. In other words, to avoid the frame-rate limit or ghosting, whenever there are two closely-timed images, they may be separated into different loops. An example is shown in the lower panel of Figure 7.10, where 2 loops, adding up to the complete proposed sequence, were suggested.

7.3.4.2 Rethinking Ghosts

Figure 7.11 shows a quantitative example of ghosting from an a-Si EPID. Ghosting caused less than 0.3% increase in grayscale value compared to an image of the same field but without recent irradiation.

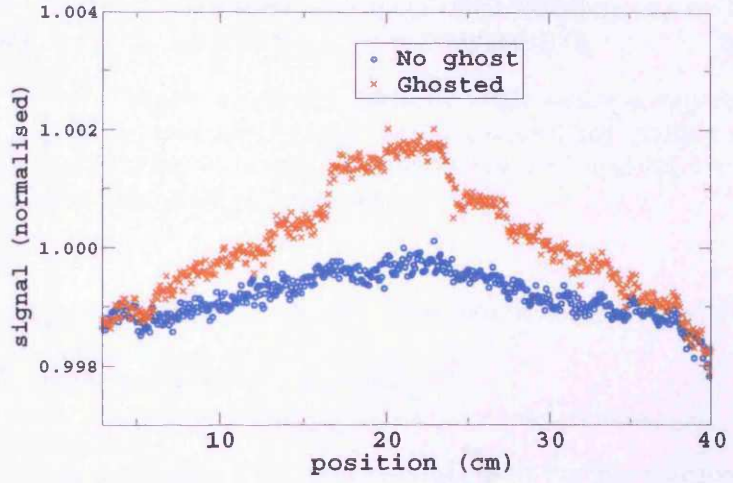

Figure 7.11: Profiles from a-Si portal images: with and without ghosting.

Figure 7.12 shows some images acquired with a SLIC EPID during a step-and-shoot beam. Generally, these are the 4 categories of images one can expect from repeated image acquisitions during a step-and-shoot beam:

1. during segment: the beam was on throughout image acquisition;
2. end of segment: the beam was on when image acquisition started, but went off before image acquisition completes;
3. between segments: the beam was off (to allow rearrangement of leaves) throughout image acquisition;

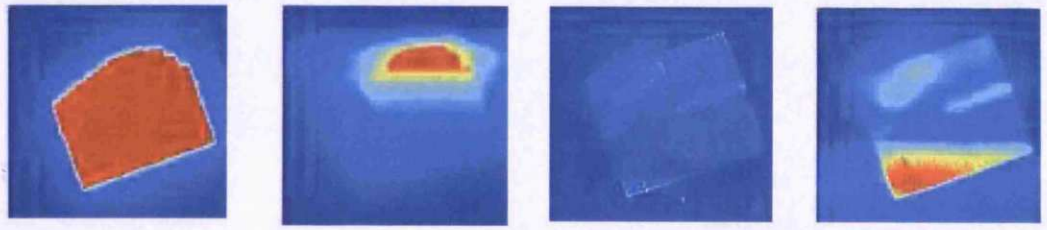

Figure 7.12: Series of images acquired on a SLIC EPID during a step-and-shoot IMRT beam. Images may be grouped into 4 categories: images acquired during beam-on, images acquired during the finishing of a segment, images acquired between two segments and images acquired during the start of a segment.

4. start of segment: the beam was off when image acquisition started, but went on before image acquisition completes.

The portal image on Figure 7.13 is an example from the last category. While such an image could conveniently be dismissed as "spoilt", it is worth a closer look. If we interpret a portal image as consecutive rows scanned one after another (Figure 7.14), it would be obvious that it is possible to reconstruct each row as a function of time. Every portal image, therefore, contains not only 2D spatial information, but also temporal information. Applying this consideration to Figure 7.13 and looking at the rows on the image as a function of time, it can be seen that:

- during the time when the top rows were read out, the beam for the first segment had gone off.

- at the time when the row marked "as readout reaches this row" was read out, the beam for the 2nd segment came on. This beam was still on at the time when the final row was read out.

Let us name the rows above the row marked "as readout reaches this row" as part A; and the rows below it as part B of the image. Now, looking at the rows as a function of space, it can be seen that:

- in part A, the field shape of the 1st segment is still visible although the beam for this segment had finished – this is a ghost.

- in part B, the grayscale indicates leaf leakage, but this location is not where the field of the 2nd segment is. The field of the 2nd segment could not be seen on the image because it was, in fact, located at the upper portion of the image.

7.4 Conclusion

Gantry-dependent artefacts in the SLIC EPID can compromise accurate dosimetry. The correction technique based on sinusoidal modulation detailed herein was able to correct for artefacts

- in both dimensions of an image.

- over a continuous range of gantry angles.

- over time, without having to regenerate correction coefficients.

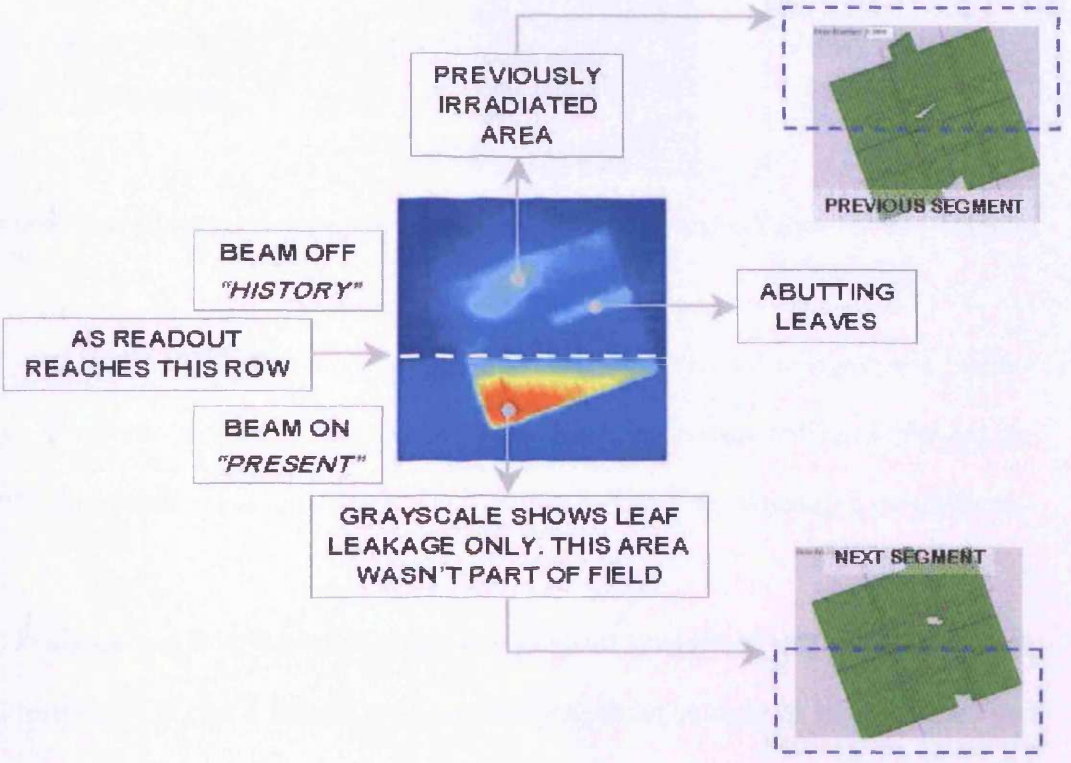

Figure 7.13: An image acquired on a SLIC EPID during transition from a segment to the next. The single image registered information about the preceding segment, the transition, and also the next segment. Ghosting is visible in the *history* area of the image.

- without intervening in image acquisition protocols, *e.g.* extra image calibration.

It is a post-acquisition process independent of image acquisition.

It restores flatness to well within 2%, comparing favourably to two existing correction techniques which are based on gantry-dependent flood field and profile averaging respectively. Overcoming these artefacts should improve usage of the EPID in general, not only in dosimetric applications but also in imaging, where an image free of low frequency variations can be "windowed" more readily.

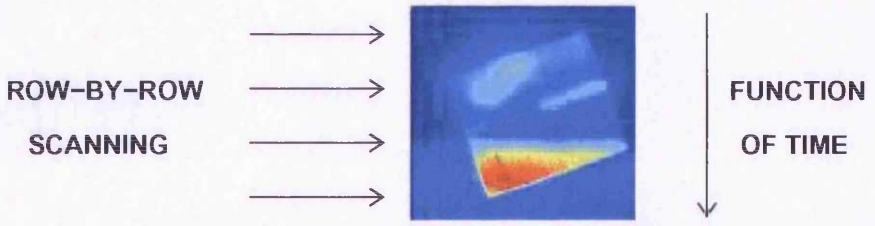

Figure 7.14: Row-by-row scanning makes it possible to reconstruct each row as a function of time.

Artefacts in the IMRT mode of the Varian aS500 EPID led to significant inaccuracies (over 2%) in dose quantification. The device is therefore not recommended for IMRT dose verification until further acquisition software developments are forthcoming.

The proposed alternative imaging sequence and the idea of spatial-cum-temporal interpretation of portal images are potentially applicable for both the SLIC and the a-Si EPIDs. Implementation of these are beyond the timescale of this thesis and therefore await further work and development.

Chapter 8

HIGH THROUGHPUT COMPUTING

If the solution for treatment verification presented in Chapter 5 is to accomplish its mission to become a clinical routine, the run time of Monte Carlo (MC) simulations has to be clinically acceptable. On an average personal computer processor of today, MC simulation of a typical case for treatment verification may take weeks of run time – which is clinically unfeasible. This chapter describes the implementation of *High Throughput Computing** (HTC), which allows different particle histories to be run on different processors simultaneously. Several levels of implementation will be reported – from the *Beowulf*† cluster to the UK National Grid Service (NGS), which is part of the UK *e-Science*‡ program.

Chapter 5 presented a MC portal dosimetry solution that is **accurate** and **versatile**. This chapter contributes the **speed** factor.

* *High Throughput Computing* has been introduced in Section 1.6.

† *Beowulf* is a project for combining independent computers through software and networking. The website is at www.beowulf.org.

‡ *e-Science* has been introduced in Section 1.4.

8.1 Introduction

With increasing demands of complex radiotherapy modalities, case-by-case full MC simulation is becoming essential for highest attainable accuracy. Therefore, the need for MC simulation is expanding from the research domain into daily clinical routines. Due to prohibitively long run times, however, clinical implementation is currently limited.

Possible ways to increase the efficiency (i.e. to reduce the run time required to achieve a given statistical uncertainty) of MC simulations include:

- *variance reduction techniques**, which introduce non-analog and/or preferential sampling;
- denoising [Kawrakow 2002, Miao et al. 2003], which smooths noisy data as a post-simulation process;
- HTC, which runs different particle histories simultaneously on different computers. Grounded on the inherent independence of one radiation history from another, this promises the most accurate outcome since it biases neither the physics nor the statistics.

HTC is the subject of this chapter. Whereas it is commonly practised using cluster computing [Love et al. 2000], a larger resource pool is available on the *Grid*†. The idea of the Grid is to provide computing power in a way analogous to electrical power

* *Variance reduction techniques* have been introduced in Section 3.3.
† The *Grid* has been introduced in Section 1.4

grids: the consumer plugs in whenever service is required, without necessarily being aware of where or how the resource is generated.

8.2 Materials & Methods

8.2.1 Four Levels of Implementation

We implemented HTC at 4 levels.

1. A Beowulf cluster at the University of Surrey, which has been in operation since year 1999 [Love et al. 2000]. A Beowulf cluster is built from *Commodity Off-The-Shelf* (COTS) hardware – it is a group of cheap personal computers running on a cheap operating system (e.g. *Linux**), connected by standard networking (e.g. *Ethernet*†).

2. A pool consisting 64 SGI‡ processors at the Welsh e-Science Centre (WeSC). This is not Beowulf since it is built from high-end servers connected by proprietary networking infrastructure, running a proprietary operating system (*IRIX*§).

3. A pool consisting over 500 desktop computers at the University of Cardiff. These processors are not dedicated to HTC but since they are not constantly in

**Linux* is a free Unix-type operating system originally created by Linus Torvalds with contributions from developers around the world. The source code is freely available to everyone.

†*Ethernet* is a technology that interconnects computers into a high-speed network originally developed by Xerox Corporation. It is widely used because it can network a wide variety of computers, it is not proprietary, and components are widely available from many commercial sources.

‡*Silicon Graphics* website is at www.sgi.com.

§The *IRIX* operating system is a technical high-performance 64-bit operating system based on industry-standard UNIX

use, their "idle times" (e.g. evenings and weekends) may be tapped for intensive computations e.g. MC simulations.

4. The NGS: the core production-level Grid created under the UK e-Science program. The NGS currently provides access to 168 dedicated dual 3.06 GHz Intel Xeon processors (336 in total) spread over four UK sites.

Neither cluster- nor Grid-computing is as straightforward as "plug-and-play". Implementations require considerable effort. Some details will be discussed in Section 8.3.1. The gain in run times of the simulations presented in Section 5.2.3 will be reported.

8.2.2 Simulations on Multiple Platforms

Multi-platform versions of EGSnrc and BEAMnrc were released in December 2003 and January 2005 respectively. With the new releases, the codes now work not only on Linux/Unix but also *Windows NT/2000/XP* and, with some restrictions, even *Apple Mac OSX*. Among the implementations listed in Section 8.2.1, operation systems differ: the cluster at Surrey and the NGS are both Linux-based, WeSC is IRIX, whereas the pool at Cardiff is Windows-XP. The architectures differ too: e.g. the processors at Surrey are Intels, whereas the ones at the WeSC are SGIs. If a simulation is to be distributed across heterogeneous systems, several issues require special handling, which will be discussed in Section 8.3.2.

8.2.3 Planning of Simulations

Radiotherapy MC simulations often involve multiple stages, e.g. a BEAMnrc simulation of the linac head, whose output would be used as input for subsequent DOSXYZnrc simulations of the patient and the electronic portal imaging device (EPID). In such multiple-staged simulations, good planning saves both execution and data transfer time. An example will be given in Section 8.3.3.

8.2.4 Simulations without Pre-installation

Installation of EGSnrc, BEAMnrc and DOSXYZnrc code systems on each and every executing *node** is not always feasible, especially on non-dedicated systems, because

- it might not be known beforehand which node would be free;
- period of node availability might be too short for code installation;
- disk space in the node might be limited (code installation requires over 160 megabytes);
- automated, non-interactive code installations are not always successful; and
- non-automated installation is labour-intensive and time-consuming.

A standalone, "light-weight" (i.e. small-size in terms of disk space) data shipment is therefore necessary for running simulations without prior code installation. This data is to be transferred to each executing node as and when a node becomes available for running simulations.

*A *node* is an individual processor from a cluster or pool consisting many processors.

8.3 Results & Discussion

8.3.1 Four Levels of Implementation

Distributing a simulation across multiple nodes saves computation time. However, without supporting software, the human labour required can be formidable. Distributing a simulation across n processors entails:

1. generating n input files, instead of one;
2. logging into each of the n nodes;
3. checking which nodes are free and which are not;
4. starting a *job** on each of the n nodes;
5. checking which jobs have been successful and which have not been;
6. repeating steps 2 to 5 for each job which has not been successful; and
7. combining n output files.

As an improvement from the preliminary cluster setup at Surrey, we installed Condor [Foster and Kesselman 2003] as the *resource broker*†, which automates steps 2 to 6. Shell scripts were also written to handle steps 1 and 7, and also to automate interfacing between these scripts and Condor.

*A *job* refers to the nth division of a simulation, which has been divided for simultaneous computation on different nodes.

†A *resource broker* matches the available resources to the user's requests by providing a uniform interface to access any of the available and appropriate resources.

On the WeSC pool, we enabled both Condor/G and Nimrod/G resource brokers [Foster and Kesselman 2003], so that the author has the choice of submitting jobs remotely from Velindre Cancer Centre without having to login to WeSC. A set of utility functions was written using the Perl programming language [Christiansen and Torkington 2003]. Further details are given in Chin et al. [2004a]. The idea was to accomplish the entire simulation with minimal user intervention – the user issues a single command from a local desktop and no further user intervention is required. Outputs are delivered direct to the local desktop at Velindre Cancer Centre once the simulation is complete.

Condor was also used to harness idle computing resources from the non-dedicated pool at Cardiff University. Condor is highly configurable, e.g. it can be configured to start a job only when the keyboard has not been used for a specified period of time (as a signal that the owner is not using the computer), and to stop the job once a keystroke has been detected (as a signal that the owner has returned to use the computer). In this way, the computer's availability to its owner is unaffected.

The NGS uses Grid *middleware** (the Globus Toolkit) to provide secure remote access to a collection of hardware, software and support resources available to the UK academic community. Globus also hides some system heterogeneity, such as the use of different batch queue systems (e.g. Condor or PBSPro) to queue and start jobs [Foster and Kesselman 2003]. Authentication is performed using *digital certificates*† issued by the UK e-Science Certificate Authority.

* *Middleware* connects otherwise separate applications and passes data between them.

† *Digital certificates* provide the electronic means of establishing the user's credentials when making transactions on the Web.

The simulations described in Section 5.2.3 were accomplished on the NGS. Nimrod/G was used as a high-level tool to create and monitor individual jobs, and as a resource broker to choose on which resources jobs should run [Abramson et al. 2000]. The geometry contained 75×75×109 voxels. The incident beam was 15 cm × 15 cm. Tally voxels, each of 0.08 cm × 0.5 cm × 3.0 cm, achieved 1% uncertainty in the penumbra and 0.4% in the beam. This simulation would have taken 6 days to run on a single 2.66 GHz Intel Pentium 4 processor. Using the NGS, and in competition with other users' computations, the DOSXYZnrc simulation took less than 3 hours to complete. This 50-fold increase in simulation efficiency brings the run time much closer to an acceptable time frame for clinical operation.

8.3.2 Simulations on Multiple Platforms

The Perl utility functions developed herein are portable across different platforms, "light-weight", and do not require compilation. These scripts are transferred along with each job submission. When a job finishes, the appropriate functions are automatically called to convert output files from binary format (which is architecture-dependent) into text format (which is architecture independent). Text versions of the output files are then transferred back to the user's local desktop computer, which will be able to understand all the output files that are transferred back regardless of the architecture used to compute each job.

8.3.3 Planning of Simulations

Figure 8.1 shows an example of how a multi-staged simulation was run on the WeSC using Condor. Automation was complemented by the in-house Perl utility functions. Immediately following the completion of each job (or "child simulation" in the figure), the utility functions trigger consecutive multi-stage jobs as required, without having to wait for *sibling** jobs to finish. Combination of phase space files are done automatically. A similar distribution scheme has been used for all levels of HTC given in Section 8.2.1, even when using other resource brokers.

8.3.4 Simulations without Pre-installation

The "light-weight" *directory tree*† transferred to each executing node was as follows:

. pegs4/data/521icru.pegs4dat

. data/incoh.data

. data/nist_brems.data

. data/photo_relax.data

. data/msnew.data

. data/photo_cs.data

. data/spinms.data

Siblings refer to jobs belonging to the same stage in a multi-staged simulation.

†A *directory tree* organises data into a hierarchical structure, beginning with a root directory and branching into subdirectories and files.

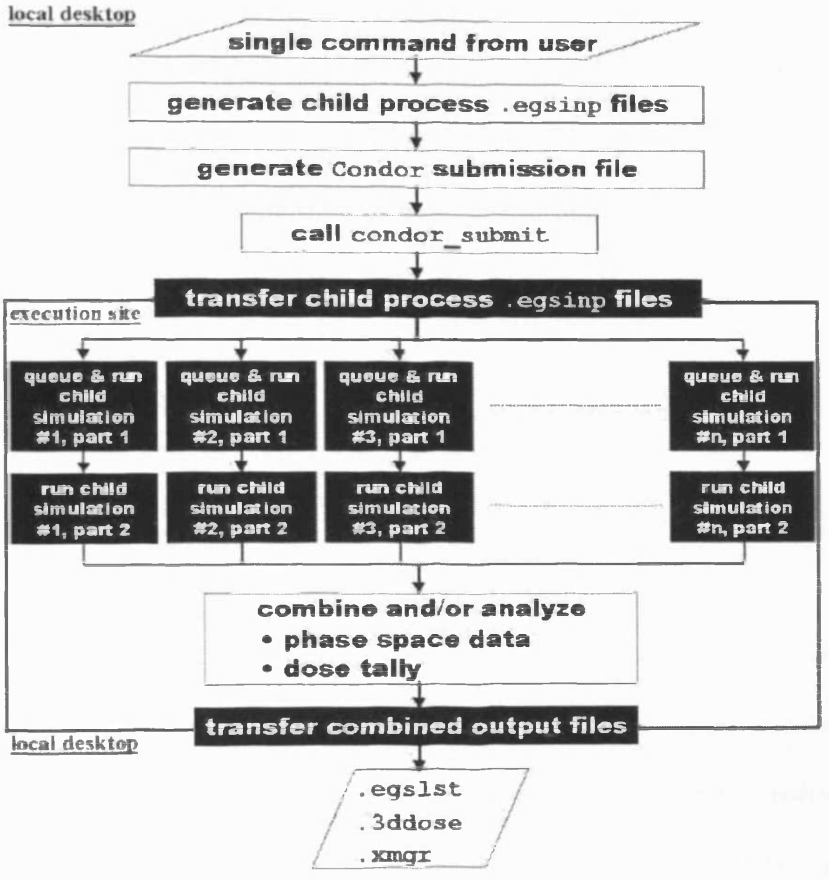

Figure 8.1: A multi-staged simulation on the WeSC. *.egsinp* is the input file. *.egslst*, *.3ddose* and *.xmgr* are the output files. *condor_submit* is a Condor command.

. *mycode*.exe

. *mycode/mycode*.io

. *mycode/mycode*.egsinp

where *mycode* is the EGSnrc code to be run. The disk space required is about 13 megabytes (compared to over 160 megabytes for a full code installation). These are

*relative paths**. No *absolute path* is required, so that the above directory tree may be placed anywhere, as decided by the resource broker at the time of job submission. This has been found to work with the following command line:

mycode.exe -i *mycode* -p 521icru -e . -H .

which runs the code *mycode* by assigning *mycode.egsinp* as the input file, *521icru.pegs4dat* as the cross section file, and the current directory as both the user's and the system's directories.

8.4 Conclusions

Migration of MC simulations from the research domain into clinical routine is no longer impeded by formidable run times. We have not only HTC-enabled EGSnrc, BEAMnrc and DOSXYZnrc simulations, but also developed a set of software utility tools to automate the labour-intensive task of splitting a simulation into parallel runs.

The different levels of HTC explored, enabled and optimised paved the way for unprecedented computing power. Each level entails different ranges of capital, maintenance and labour costs. Based on these factors, the decision to employ one of the levels or a combination of several levels is to be made.

Our usage of the Grid has been free of charge. Collaboration with the WeSC has been on a goodwill basis, as impetus for further funding and investment for both parties. However, the service is expected to be charged for in the future.

*A *relative path* is the designation of a file location in relation to the current working directory, as opposed to an *absolute path* which gives the exact location.

Chapter 9

CONCLUSIONS

9.1 Summary

A Monte Carlo (MC) portal dosimetry solution for verifying radiotherapy photon beams has been presented. It combines the technology of electronic portal imaging devices (EPIDs) with the accuracy of MC simulations. With reference to the purpose set out in the abstract, this project successfully developed a solution which is accurate (2%) across the entire clinical range of beam size, gantry angle, beam-patient and patient-imager separations. The accuracy is maintained for both pre-treatment and on-treatment verifications. Implementation on various levels of High Throughput Computing (HTC) prepares the solution for efficient clinical productivity.

With reference to the objective and context set out in Section 1.5, forward portal dose prediction by the above solution has been shown to overcome the constraints reported in existing techniques. Accuracy is not compromised at regions of inhomogeneous composition, at small and large field sizes, whether or not a patient/phantom is in the beam. Separation of the EPID from the patient/phantom is no longer constrained to 80 cm and beyond.

The solution achieved combined accuracy, versatility and speed hitherto unreported. It is therefore ready to answer the clinical need for verifying treatments of individual patients at Velindre Cancer Centre. Such a need is by no means local, however. The solution developed herein is expected to be equally applicable to other radiotherapy centres.

Table 9.1 summarises the contributions of this research project to the scientific and medical community.

Table 9.1: Original contributions reported in this thesis.

Context	Contribution	Publication
Voxel-based MC codes do not allow definition of oblique planes which are required for simulation of oblique beams (Chapter 5)	A solution based on integrated phantoms where the effect of beam obliquity is included using geometric transformations	Chin et al. [2003]
Response of the SLIC EPID varies with linear accelerator gantry angle (Chapter 7)	A correction technique based on nonlinear regression of a three-variable sinusoidal modulation	Chin et al. [2004b]
Long run times of MC simulations hinder clinical implementation (Chapter 8)	Implementation of BEAMnrc MC simulations on the GRID	Chin et al. [2004a]
Dosimetric use of a-Si EPIDs (Chapter 7)	Identified significant anomalies which could compromise dosimetric accuracy	Chin and Lewis [2004]
The need for a verification solution for photon teletherapy (Chapter 5)	A MC portal dosimetry solution which has been tested under a wide range of clinical conditions	Chin et al. [2005]
MC studies of radiation transport in the a-Si and SLIC detectors (Chapter 6)	Design of simplified EPID models for MC simulations	in preparation

This work included both the scanning liquid ionisation chamber (SLIC) and the amorphous silicon (a-Si) EPID types, with a slight emphasis on the former. This is because an a-Si EPID was not available locally during this project; experiments on the device were carried out at our collaborating institutions. As detailed in Section 5.4, the MC portal dosimetry solution is expected to be readily adaptable for the a-Si EPID. In fact, the application for the a-Si EPID should be simpler due to the linear dose response and the absence of the *bulging effect*.

While some North American and European centres are replacing SLIC EPIDs with a-Si EPIDs, the former is not becoming obsolete just yet in the wider world. Indeed, there have already been requests for further information on our SLIC EPID work from other countries.

9.2 Further Work

The following topics are beyond the timescale of this thesis and therefore await further work and development:

- clinical trials using the MC portal dosimetry solution developed herein for verifying radiotherapy photon treatments at Velindre Cancer Centre;
- the alternative imaging sequence based on strategically programmed sequence templates, as proposed in Chapter 7;
- the new way of interpreting portal images by incorporating both spatial and temporal information as proposed in Chapter 7;

- MC portal dose prediction of electron beams by simulating energy deposition by bremsstrahlung photons on the EPID; and

- feasibility studies of developing and using *inverse Monte Carlo** simulations to reconstruct patient dose from physically acquired portal images.

*By *inverse Monte Carlo* the author refers to simulations that truly invert radiation histories, where a new code with "speeding powers" instead of "stopping powers", and inverse solutions to various transport equations etc. have to be developed, as opposed to the *adjoint Monte Carlo* already available in MCNP, which operates on the multigroup (rather than continuous energy) mode [Wagner et al. 1993]. Application of the latter for portal dose reconstruction has been reported by Jarry and Verhaegen [2004].

Bibliography

D. Abramson, J. Giddy, and L. Kotler. High-performance parametric modeling with Nimrod/G. Killer application for the global Grid? *International Parallel and Distributed Computing Symposium*, pages 520–8, 2000.

A. Ahnesjö and M. M. Aspradakis. Dose calculations for external photon beams in radiotherapy. *Phys. Med. Bio.*, 44:R99–155, 1999.

P. Andreo. *Monte Carlo Transport of Electrons and Photons*, chapter Stopping-power Ratios for Dosimetry. Plenum Press, 1988.

L. E. Antonuk. Electronic portal imaging devices: a review and historical perspective of contemporary technologies and research. *Phys. Med. Biol.*, 47:R31–R65, 2002.

L. E. Antonuk, Y. El-Mohri, J. H. Siewerdsen, J. Yorkston, W. Huang, V. E. Scarpine, and R. A. Street. Empirical investigation of the signal performance of a high resolution, indirect detection, active matrix flat-panel imager (AMFPI) for fluoroscopic and radiographic operation. *Med. Phys.*, 24:51–70, 1997.

L. E. Antonuk, J. Yorkston, W. D. Huang, H. Sandler, J. H. Siewerdsen, and Y. El-Mohri. Megavoltage imaging with a large-area, flat-panel, amorphous silicon imager. *Int. J. Radiat. Oncol. Biol. Phys.*, 36:661–672, 1996.

H. H. Barrett and W. Swindell. *Radiological Imaging.* Academic Press, 1981.

A. Bel, R. Keus, R. E. Vijlbrief, and J. V. Lebesque. Setup deviations in wedged pair irradiation of parotid-gland and tonsillar tumors, measured with an electronic portal imaging device. *Radiother. Oncol.*, 37:153–159, 1995.

R. Berbeco, S. B. Jiang, G. Sharp, H. Mostafavi, S. Kollipara, and G. T. Y. Chen. Patient setup with respiratory gated electronic portal imaging. *Med. Phys.*, 30: 1383–1384, 2003.

M. J. Berger and R. Wang. *Monte Carlo Transport of Electrons and Photons*, chapter Multiple-scattering angular deflections and energy-loss straggling. Plenum Press, 1988.

J. P. Bissonnette, I. A. Cunningham, and P. Munro. Optimal phosphor thickness for portal imaging. *Med. Phys.*, 24:803–14, 1997.

J. P. Bissonnette, P. Munro, and I. A. Cunningham. Monte Carlo simulation of the image formation process in portal imaging. *Med. Phys.*, 30:3243–50, 2003.

R. Boellaard. In vivo dosimetry with a liquid-filled electronic portal imaging device. *Med. Phys.*, 25:2483–2483, 1998.

R. Boellaard, M. van Herk, and B. J. Mijnheer. The dose response relationship of a liquid-filled electronic portal imaging device. *Med. Phys.*, 23:1601–1611, 1996.

R. Boellaard, M. van Herk, H. Uiterwaal, and B. Mijnheer. Two-dimensional exit dosimetry using a liquid-filled electronic portal imaging device and a convolution model. *Radiother. Oncol.*, 44:149–157, 1997.

A. A. Boxwala, E. L. Chaney, D. S. Fritsch, S. Raghavan, C. S. Coffey, S. A. Major, and K. E. Muller. Comparison of computer workstation with light box for detecting setup errors from portal images. *Int. J. Radiat. Oncol. Biol. Phys.*, 44:711–716, 1999.

A. L. Boyer, L. Antonuk, A. Fenster, M. van Herk, H. Meertens, P. Munro, L. E. Reinstein, and J. Wong. A review of electronic portal imaging devices (EPIDs). *Med. Phys.*, 19:1–16, 1992.

A. Brahme. The development of radiation therapy from IMRT to biologically optimized predictive assay based light ion radiation therapy. In *Proc. 14th Int. Conf on the Use of Computers in Radiation Therapy*, Seoul, 2004. Jeong.

J. Briesmeister. *MCNP - A general purpose Monte Carlo code for neutron and photon transport, Version 3A, LANL Report LA-7396-M.* Los Alamos National Laboratory, Los Alamos, 1986.

J. Briesmeister. *MCNP - A general Monte Carlo N-particle transport code, LANL Report LA-12625-M.* Los Alamos National Laboratory, Los Alamos, 1993.

J. Burmeister, J. Farr, L. Santanam, M. Yudelev, and R. L. Maughan. Preliminary investigation of intensity modulated neutron radiotherapy (WIP). *Med. Phys.*, 30: 1448–1448, 2003.

J. Chang, E. Ford, H. Amols, and C. C. Ling. Verify intensity modulated radiotherapy (IMRT) beam delivery using the frame-averaging mode of amorphous silicon (a-Si) electronic portal-imaging device (EPID). *Med. Phys.*, 29:1366–1366, 2002.

J. Chang and C. C. Ling. Using the frame averaging of aS500 EPID for IMRT verification. *J. Appl.Clin. Med. Phys.*, 4:287–99, 2003.

J. Chang, C. H. Obcemea, J. Sillanpaa, J. Mechalakos, and C. Burman. Use of EPID for leaf position accuracy QA of dynamic multi-leaf collimator (DMLC) treatment. *Med. Phys.*, 31:2091–2096, 2004.

J. H. Chang, G. S. Mageras, C. C. Ling, and W. Lutz. An iterative EPID calibration procedure for dosimetric verification that considers the EPID scattering factor. *Med. Phys.*, 28:2247–2257, 2001.

H. Chen, J. Yang, P. Stapleton, and S. Murphy. Calibration of MLC leaf positions with an electronic portal imaging device for IMRT delivery. *Med. Phys.*, 29:1262–1262, 2002.

P. W. Chin and D. G. Lewis. The Varian aS500 EPID as a dosemeter: preliminary investigations. In *Proc. 8th Int. Workshop Electronic Portal Imaging*, 2004.

P. W. Chin, D. G. Lewis, and J. P. Giddy. Implementation of BEAMnrc Monte Carlo simulations on the Grid. In *Proc. 14th Int. Conf on the Use of Computers in Radiation Therapy*, Seoul, 2004a. Jeong.

P. W. Chin, D. G. Lewis, and J. P. Giddy. A Monte Carlo solution for external beam photon radiotherapy verification. In *The Monte Carlo Method: Versatility Unbounded In A Dynamic Computing World*, Chattanooga, 2005.

P. W. Chin, D. G. Lewis, and E. Spezi. Correction for dose-response variations in a scanning liquid ion chamber EPID as a function of linac gantry angle. *Phys. Med. Biol.*, 49:N93–N103, 2004b.

P. W. Chin, E. Spezi, and D. G. Lewis. Monte Carlo simulation of portal dosimetry on a rectilinear voxel geometry: a variable gantry angle solution. *Phys. Med. Biol.*, 48:N231–N238, 2003.

T. Christiansen and N. Torkington. *Perl Cookbook*. O'Reilly, 2nd edition, 2003.

F. Cremers, T. Frenzel, C. Kausch, D. Albers, T. Schonborn, and R. Schmidt. Performance of electronic portal imaging devices (EPIDs) used in radiotherapy: image quality and dose measurements. *Med. Phys.*, 31:985–996, 2004.

A. J. Curtin-Savard and E. B. Podgorsak. Verification of segmented beam delivery using a commercial electronic portal imaging device. *Med. Phys.*, 26:737–742, 1999.

H. C. J. de Boer, J. R. V. De Koste, S. Senan, A. G. Visser, and B. J. M. Heijmen. Analysis and reduction of 3D systematic and random setup errors during the simulation and treatment of lung cancer patients with CT-based external beam radiotherapy dose planning. *Int. J. Radiat. Oncol. Biol. Phys.*, 49:857–868, 2001.

L. Dong, L. Court, H. Wang, J. O. Daniel, and R. Mohan. Image-guided radiotherapy with in-room CT-on-rails. In *Proc. 14th Int. Conf on the Use of Computers in Radiation Therapy*, Seoul, 2004. Jeong.

K. Eberle, J. Engler, G. Hartmann, R. Hofmann, and J. R. Horandel. First tests of a liquid ionization chamber to monitor intensity modulated radiation beams. *Phys. Med. Biol.*, 48:3555–3564, 2003.

Y. El-Mohri, L. E. Antonuk, J. Yorkston, K. W. Jee, M. Maolinbay, K. L. Lam, and J. H. Siewerdsen. Relative dosimetry using active matrix flat-panel imager (AMFPI) technology. *Med. Phys.*, 26:1530–1541, 1999.

A. A. H. Elgayed, A. Bel, R. Vijlbrief, H. Bartelink, and J. V. Lebesque. Time trend of patient setup deviations during pelvic irradiation using electronic portal imaging. *Radiother. Oncol.*, 26:162–171, 1993.

M. Essers, R. Boellaard, M. van Herk, H. Lanson, and B. Mijnheer. Transmission dosimetry with a liquid-filled electronic portal imaging device. *Int. J. Radiat. Oncol. Biol. Phys.*, 34:931–941, 1996.

M. Essers, B. R. Hoogervorst, M. van Herk, H. Lanson, and B. J. Mijnheer. Dosimetric characteristics of a liquid-filled electronic portal imaging device. *Int. J. Radiat. Oncol. Biol. Phys.*, 33:1265–1272, 1995.

P. M. Evans, E. M. Donovan, N. Fenton, V. N. Hansen, I. Moore, M. Partridge, S. Reise, B. Suter, J. R. N. Symonds-Tayler, and J. R. Yarnold. Practical implementation of compensators in breast radiotherapy. *Radiother. Oncol.*, 49:255–265, 1998.

P. M. Evans, E. M. Donovan, M. Partridge, A. M. Bidmead, A. Garton, and C. Mubata. Radiological thickness measurement using a liquid ionization chamber electronic portal imaging device. *Phys. Med. Biol.*, 44:N89–N97, 1999.

A. L. Fielding, P. M. Evans, and C. H. Clark. The use of electronic portal imaging to verify patient position during intensity-modulated radiotherapy delivered by the dynamic MLC technique. *Int. J. Radiat. Oncol. Biol. Phys.*, 54:1225–1234, 2002.

E. C. Ford, G. S. Mageras, E. Yorke, K. E. Rosenzweig, R. Wagman, and C. C. Ling. Evaluation of respiratory movement during gated radiotherapy using film and electronic portal imaging. *Int. J. Radiat. Oncol. Biol. Phys.*, 52:522–531, 2002.

I. Foster and C. Kesselman, editors. *The Grid: Blueprint for a New Computing Infrastructure.* Elsevier, 2003.

L. M. Girouard, J. Pouliot, X. Maldague, and A. Zaccarin. Automatic setup deviation measurements with electronic portal images for pelvic fields. *Med. Phys.*, 25:1180–1185, 1998.

S. Goudsmit and J. L. Saunderson. Multiple scattering of electrons. *Phys. Rev.*, 57, 1940.

K. Gray. Personal communication. *Velindre Cancer Centre*, 2003.

D. Greene and P. C. Williams. *Linear Accelerators for Radiation Therapy.* IOP Publishing, 2nd edition, 1997.

P. B. Greer and C. C. Popescu. Dosimetric properties of an amorphous silicon electronic portal imaging device for verification of dynamic intensity modulated radiation therapy. *Med. Phys.*, 30:1618–1627, 2003.

E. E. Grein, R. Lee, and K. Luchka. An investigation of a new amorphous silicon electronic portal imaging device for transit dosimetry. *Med. Phys.*, 29:2262–2268, 2002.

B. H. Hasegawa. *Medical X-ray Imaging.* Medical Physics Publishing, Wisconsin, 1991.

K. E. Hatherly, J. C. Smylie, A. Rodger, M. J. Dally, S. R. Davis, and J. L. Millar. A double exposed portal image comparison between electronic portal imaging hard copies and port films in radiation therapy treatment setup confirmation to determine its clinical application in a radiotherapy center. *Int. J. Radiat. Oncol. Biol. Phys.*, 49:191–198, 2001.

B. J. M. Heijmen, K. L. Pasma, M. Kroonwijk, V. G. M. Althof, J. C. J. Deboer, A. G. Visser, and H. Huizenga. Portal dose measurement in radiotherapy using an electronic portal imaging device EPID. *Phys. Med. Biol.*, 40:1943–1955, 1995.

M. G. Herman, J. M. Balter, D. A. Jaffray, K. P. McGee, P. Munro, S. Shalev, M. van Herk, and J. W. Wong. Clinical use of electronic portal imaging: report of AAPM radiation therapy committee task group 58. *Med. Phys.*, 28:712–737, 2001.

K. Hierholz, W. Baus, K. Muller-Sievers, and B. Kober. Multileaf collimator: an additional method of quality assurance for a GE-accelerator. *Strahlenther. Onkol.*, 175:616–619, 1999.

R. A. Holroyd and D. F. Anderson. The physics and chemistry of room temperature liquid-filled ionization chambers. *Nucl. Instrum. Meth. A*, 236:294–9, 1985.

M. A. Hunt, T. E. Schultheiss, G. E. Desobry, M. Hakki, and G. E. Hanks. An evaluation of setup uncertainties for patients treated to pelvic sites. *Int. J. Radiat. Oncol. Biol. Phys.*, 32:227–233, 1995.

M. K. Islam, B. Norrlinger, and E. Fan. Performance characteristics of an amorphous silicon electronic portal imaging device as a relative dosimeter. *Med. Phys.*, 30: 1497–1497, 2003.

D. Jaffray. Kilovoltage and megavoltage cone beam computed tomography. In *Proc. 14th Int. Conf on the Use of Computers in Radiation Therapy*, Seoul, 2004. Jeong.

D. A. Jaffray, J. J. Battista, A. Fenster, and P. Munro. X-ray sources of medical linear accelerators - focal and extrafocal radiation. *Med. Phys.*, 20:1417–1427, 1993.

D. A. Jaffray, J. J. Battista, A. Fenster, and P. Munro. X-ray scatter in megavoltage transmission radiography - physical characteristics and influence on image quality. *Med. Phys.*, 21:45–60, 1994.

D. A. Jaffray, J. H. Siewerdsen, J. W. Wong, and A. A. Martinez. Flat-panel cone-beam computed tomography for image-guided radiation therapy. *Int. J. Radiat. Oncol. Biol. Phys.*, 53:1337–1349, 2002.

O. Jakel, D. Schulz-Ertner, C. P. Karger, A. Nikoghosyan, and J. Debus. Heavy ion therapy: status and perspectives. *Technol. Cancer Res. Treat.*, 2:377–387, 2003.

H. V. James, S. Atherton, G. J. Budgell, M. C. Kirby, and P. C. Williams. Verification of dynamic multileaf collimation using an electronic portal imaging device. *Phys. Med. Biol.*, 45:495–509, 2000.

G. Jarry and F. Verhaegen. Modelling of an aSi EPID using forward and inverse Monte Carlo techniques. In *Current Topics in Monte Carlo Treatment Planning, Advanced Workshop*, Montreal, 2004.

R. Jeraj, T. R. Mackie, J. Balog, G. Olivera, D. Pearson, J. Kapatoes, K. Ruchala, and P. Reckwerdt. Radiation characteristics of helical tomotherapy. *Med. Phys.*, 31:396–404, 2004.

H. E. Johns and J. R. Cunningham. *The Physics of Radiology.* Charles C Thomas, 4th edition, 1983.

R. S. J. P. Kaatee, M. J. J. Olofsen, M. B. J. Verstraate, S. Quint, and B. J. M. Heijmen. Detection of organ movement in cervix cancer patients using a fluoroscopic electronic portal imaging device and radiopaque markers. *Int. J. Radiat. Oncol. Biol. Phys.*, 54:576–583, 2002.

C. Kausch, B. Schreiber, F. Kreuder, R. Schmidt, and O. Dossel. Monte Carlo simulations of the imaging performance of metal plate/phosphor screens used in radiotherapy. *Med. Phys.*, 26:2113–2124, 1999.

I. Kawrakow. Accurate condensed history Monte Carlo simulation of electron transport. I. EGSnrc, the new EGS4 version. *Med. Phys.*, 27:485–98, 2000a.

I. Kawrakow. Accurate condensed history Monte Carlo simulation of electron transport. II. Application to ion chamber response simulations. *Med. Phys.*, 27:499–513, 2000b.

I. Kawrakow. On the de-noising of Monte Carlo calculated dose distributions. *Phys. Med. Bio.*, 47:3087–103, 2002.

I. Kawrakow and D. W. O. Rogers. *The EGSnrc Code System, NRCC Report PIRS-701.* NRCC, Ottawa, 2002.

I. Kawrakow, D. W. O. Rogers, and B. R. B. Walters. Large efficiency improvements in BEAMnrc using directional bremsstrahlung splitting. *Med. Phys.*, 31:2883–2898, 2004.

H. Keller, M. Fix, and P. Ruegsegger. Calibration of a portal imaging device for high-precision dosimetry: a Monte Carlo study. *Med. Phys.*, 25:1891–1902, 1998.

F. M. Khan. *The Physics of Radiation Therapy.* Williams & Wilkins, Baltimore, 2nd edition, 1994.

M. C. Kirby and P. C. Williams. The use of an electronic portal imaging device for exit dosimetry and quality-control measurements. *Int. J. Radiat. Oncol. Biol. Phys.*, 31:593–603, 1995.

L. Ko, J. O. Kim, and J. V. Siebers. Investigation of the optimal backscatter for an aSi electronic portal imaging device. *Phys. Med. Bio.*, 49:1723–38, 2004.

M. Kroonwijk, K. L. Pasma, S. Quint, P. C. M. Koper, A. G. Visser, and B. J. M. Heijmen. In vivo dosimetry for prostate cancer patients using an electronic portal imaging device (EPID); demonstration of internal organ motion. *Radiother. Oncol.*, 49:125–132, 1998.

H. D. Kubo, E. G. Shapiro, and E. J. Seppi. Potential and role of a prototype amorphous silicon array electronic portal imaging device in breathing synchronized radiotherapy. *Med. Phys.*, 26:2410–2414, 1999.

G.J. Kutcher, R. Mohan, A. S. Leibel, Z. Fuks, and C. C. Ling. *Radiation Therapy Physics*, chapter Computer-Controlled 3D Conformal Radiation Therapy. Springer Verlag, 1995.

K. L. Lam, R. K. Tenhaken, D. L. McShan, and A. F. Thornton. Automated-determination of patient setup errors in radiationtherapy using spherical radio-opaque markers. *Med. Phys.*, 20:1145–1152, 1993.

D. Letourneau, M. Gulam, D. Yan, M. Oldham, and J. W. Wong. Evaluation of a 2D diode array for IMRT quality assurance. *Radiother. Oncol.*, 70:199–206, 2004.

Q. Li, T. Kanai, and A. Kitagawa. The potential application of beta-delayed particle decay beam C-9 in cancer therapy. *Phys. Med. Biol.*, 49:1817–1831, 2004.

R. J. W. Louwe, R. Tielenburg, K. M. van Ingen, B. J. Mijnheer, and M. B. van Herk. The stability of liquid-filled matrix ionization chamber electronic portal imaging devices for dosimetry purposes. *Med. Phys.*, 31:819–827, 2004.

P. Love, E. Spezi, D. G. Lewis, C. W. Smith, E. Morton, and D. Munro. Parallel processing of radiotherapy Monte Carlo simulations on a remote Beowulf cluster. In W. Schlegel and T. Bortfeld, editors, *Proc. 13th Int. Conf on the Use of Computers in Radiation Therapy*, Heidelberg, 2000. Springer.

D. A. Low, W. B. Harms, S. Mutic, and J. A. Purdy. A technique for the quantitative evaluation of dose distributions. *Med. Phys.*, 25:656–661, 1998.

K. Luchka, D. Chen, S. Shalev, G. Gluhchev, and R. Rajapakshe. Assessing radiation and light field congruence with a video based electronic portal imaging device. *Med. Phys.*, 23:1245–1252, 1996.

K. Luchka and S. Shalev. Pelvic irradiation of the obese patient: a treatment strategy involving megavoltage simulation and intratreatment setup corrections. *Med. Phys.*, 23:1897–1902, 1996.

T. R. Mackie, T. Holmes, S. Swerdloff, P. Reckwerdt, J. O. Deasy, J. Yang, B. Paliwal B, and T. Kinsella T. Tomotherapy: a new concept for the delivery of dynamic conformal radiotherapy. *Med. Phys.*, 20, 1993.

W. P. M. Mayles, R. A. Lake, A. L. McKenzie, E. M. Macaulay, H. M. Morgan, and S. K. Powley. *Physics aspects of quality control in radiotherapy (Report 81)*. IPEM, 1999.

B. M. C. McCurdy, K. Luchka, and S. Pistorius. Dosimetric investigation and portal dose image prediction using an amorphous silicon electronic portal imaging device. *Med. Phys.*, 28:911–924, 2001.

L. N. McDermott, R. J. W. Louwe, J. J. Sonke, M. B. van Herk, and B. J. Mijnheer. Dose-response and ghosting effects of an amorphous silicon electronic portal imaging device. *Med. Phys.*, 31:285–295, 2004.

T. R. McNutt, T. R. Mackie, and B. R. Paliwal. Analysis and convergence of the iterative convolution/superposition dose reconstruction technique for multiple treatment beams and tomotherapy. *Med. Phys.*, 24:1465–1476, 1997.

T. R. McNutt, T. R. Mackie, P. Reckwerdt, and B. R. Paliwal. Modeling dose distributions from portal dose images using the convolution/superposition method. *Med. Phys.*, 23:1381–1392, 1996.

G. V. Menon and R. S. Sloboda. Compensator quality control with an amorphous silicon EPID. *Med. Phys.*, 30:1816–1824, 2003.

B. Miao, R. Jeraj, S. Bao, and T. R. Mackie. Adaptive anisotropic diffusion filtering of Monte Carlo dose distributions. *Phys. Med. Bio.*, 48:2767–81, 2003.

J. L. Millar, K. Hatherly, G. Pitson, and K. Nash. Electronic portal imaging in the detection of setup variation in daily treatment of patients undergoing radiation treatment for prostate cancer. *Eur. J. Cancer*, 33:463–463, 1997.

U. Moch, T. Auberger, D. Georg, J. Bogner, U. Wolff, A. Wambersie, and R. Potter. 3D-proton radiotherapy vs. photon radiotherapy in primary prostate cancer: comparison of dose distribution in stage-adapted target volume choice. *Strahlenther. Onkol.*, 178:57–57, 2002.

G. Moliere. Theorie der Sreuung schneller geladener Teilchen II: Mehrfach- und Vielfachstreuung. *Z. Naturforsch.*, 3a, 1948.

J. J. More. *The Levenberg-Marquardt algorithm: implementation and theory in numerical analysis*, chapter Lecture Notes in Mathematics 630. Springer-Verlag, Berlin, 1977.

P. Munro. Portal imaging technology: past, present, and future. *Semin. Radiat. Oncol.*, 5:115–33, 1995.

P. Munro and D. C. Bouius. X-ray quantum limited portal imaging using amorphous silicon flat-panel arrays. *Med. Phys.*, 25:689–702, 1998.

P. Munro and M. Mulligan. Reducing the weight of the EC-L cassette. *Int. J. Radiat. Oncol. Biol. Phys.*, 54:290–9, 2002.

A. E. Nahum. *Monte Carlo Transport of Electrons and Photons*, chapter Overview of Photon and Electron Monte Carlo. Plenum Press, 1988.

W. R. Nelson, H. Hirayama, and D. W. O. Rogers. *The EGS4 Code System, Report SLAC-265.* SLAC, Stanford, 1985.

J. Nielsen and S. H. Jensen. Some experimental and clinical lights on rotation therapy, its basis and possibilities. *Acta Radiol.*, 23:51–66, 1942.

C. Obcemea, J. Chang, J. Mechalakos, and C. Burman. Use of electronic portal imaging device (EPID) for leaf position accuracy QA of dynamic multi-leaf collimator (DMLC) treatments. *Med. Phys.*, 30:1395–1396, 2003.

S. R. Ozard and E. E. Grein. Analytical calculation of the portal scatter to primary dose ratio: an EGS4 Monte Carlo and experimental validation at large air gaps. *Phys. Med. Biol.*, 46:1719–1736, 2001.

G. Pang and J. A. Rowlands. Electronic portal imaging with an avalanche-multiplication-based video camera. *Med. Phys.*, 27:676–684, 2000.

M. Partridge, P. M. Evans, M. van Herk, L. S. Ploeger, G. J. Budgell, and H. V. James. Leaf position verification during dynamic beam delivery: a comparison of three applications using electronic portal imaging. *Med. Phys.*, 27:1601–1609, 2000.

M. Partridge, P. M. Evens, and J. R. N. Symonds-Tayler. Optical scattering in camera-based electronic portal imaging. *Phys. Med. Biol.*, 44:2381–2396, 1999.

K. L. Pasma, M. L. P. Dirkx, M. Kroonwijk, A. G. Visser, and B. J. M. Heijmen. Dosimetric verification of intensity modulated beams produced with dynamic multileaf collimation using an electronic portal imaging device. *Med. Phys.*, 26:2373–2378, 1999.

B. L. Phillips, M. R. Jiroutek, G. Tracton, M. Elfervig, K. E. Muller, and E. L. Chaney. Thresholds for human detection of patient setup errors in digitally reconstructed portal images of prostate fields. *Int. J. Radiat. Oncol. Biol. Phys.*, 54: 270–277, 2002.

L. Pisani, D. Lockman, D. Jaffray, D. Yan, A. Martinez, and J. Wong. Setup error in radiotherapy: on-line correction using electronic kilovoltage and megavoltage radiographs. *Int. J. Radiat. Oncol. Biol. Phys.*, 47:825–839, 2000.

L. S. Ploeger, M. H. P. Smitsmans, K. G. A. Gilhuijs, and M. van Herk. A method for geometrical verification of dynamic intensity modulated radiotherapy using a scanning electronic portal imaging device. *Med. Phys.*, 29:1071–1079, 2002.

C. Popescu, P. Greer, and D. Wells. Use of an amorphous silicon electronic portal imaging device for dynamic multileaf collimator quality assurance. *Med. Phys.*, 29: 1366–1366, 2002.

J. Pouliot and A. Lirette. Verification and correction of setup deviations in tangential breast irradiation using EPID: gain versus workload. *Med. Phys.*, 23:1393–1398, 1996.

B. W. Raaymakers, A. J. E. Raaijmakers, A. N. T. J. Kotte1, D. Jette, and J. J. W. Lagendijk1. Integrating a MRI scanner with a 6 MV radiotherapy accelerator: dose deposition in a transverse magnetic field. *Phys. Med. Bio.*, 49(17):4109–4118, 2004.

T. Radcliffe, G. Barnea, B. Wowk, R. Rajapakshe, and S. Shalev. Monte-Carlo optimization of metal phosphor screens at megavoltage energies. *Med. Phys.*, 20: 1161–1169, 1993.

D. M. Roback and B. J. Gerbi. Evaluation of electronic portal imaging device for missing tissue compensator design and verification. *Med. Phys.*, 22:2029–2034, 1995.

D. W. O. Rogers, C-M Ma, B. Walters, G. X. Ding, D. Sheikh-Bagheri, and G. Zhang. *BEAM Users Manual, NRCC Report PIRS-0509A (rev D).* NRCC, Ottawa, 2000.

D. W. O. Rogers, C-M Ma, B. Walters, G. X. Ding, D. Sheikh-Bagheri, and G. Zhang. *BEAMnrc Users Manual, NRCC Report PIRS-0509A (rev G).* NRCC, Ottawa, 2001.

S. S. Samant, W. Zheng, N. A. Parra, J. Chandler, A. Gopal, J. Wu, J. Jain, Y. P. Zhu, and M. Sontag. Verification of multileaf collimator leaf positions using an electronic portal imaging device. *Med. Phys.*, 29:2900–2912, 2002.

M. J. Samson, J. R. V. de Koste, H. C. J. de Boer, H. Tankink, M. Verstraate, M. Essers, A. G. Visser, and S. Senan. An analysis of anatomic landmark mobility and setup deviations in radiotherapy for lung cancer. *Int. J. Radiat. Oncol. Biol. Phys.*, 43:827–832, 1999.

F. Sauter. Über den atomaren photoeffekt in der k-schale nach der relativistischen wellenmechanik diracs. *Ann. Physik*, 11:454–488, 1931.

J. Seco, E. Adams, M. Bidmead, M. Partridge, and F. Verhaegen. Head-and-neck IMRT treatments assessed with a Monte Carlo dose calculation engine. *Phys. Med. Bio.*, 50:817–30, 2005.

J. Sempau, A. Snchez-Reyes, F. Salvat, H. Oulad ben Tahar, S. B. Jiang, and J. M. Fernndez-Varea. Monte Carlo simulation of electron beams from an accelerator head using PENELOPE. *Phys. Med. Bio.*, 46:1163–86, 2001.

S. Shalev. *Radiation Therapy Physics*, chapter Treatment Verification Using Digital Imaging. Springer Verlag, 1995.

J. V. Siebers, J. O. Kim, L. Ko, P. J. Keall, and R. Mohan. Monte Carlo computation of dosimetric amorphous silicon electronic portal images. *Med. Phys.*, 31:2135, 2004.

J. J. Sonke, L. S. Ploeger, B. Brand, M. H. P. Smitsmans, and M. van Herk. Leaf trajectory verification during dynamic intensity modulated radiotherapy using an amorphous silicon flat panel imager. *Med. Phys.*, 31:389–395, 2004.

E. Spezi. *A Monte Carlo investigation of the accuracy of intensity modulated radiotherapy.* PhD thesis, University of Wales College of Medicine, 2003.

E. Spezi and D. G. Lewis. Full forward Monte Carlo calculation of portal dose from MLC collimated treatment beams. *Phys. Med. Biol.*, 47:377–390, 2002.

L. Spies and T. Bortfeld. Analytical scatter kernels for portal imaging at 6 MV. *Med. Phys.*, 28:553–559, 2001.

E. Storm and H. I. Israel. Photon cross sections from 1 kev to 100 MeV for elements Z=1 to Z=100. *Atomic Data and Nuclear Data Tables*, 7, 1970.

P. Suortti and W. Thomlinson. Medical applications of synchrotron radiation. *Phys. Med. Biol.*, 48:R1–R35, 2003.

W. Swindell and P. M. Evans. Scattered radiation in portal images: a Monte Carlo simulation and a simple physical model. *Med. Phys.*, 23:63–73, 1996.

B. van Asselen, C. P. J. Raaijmakers, J. J. W. Lagendijk, and C. H. J. Terhaard. Intrafraction motions of the larynx during radiotherapy. *Int. J. Radiat. Oncol. Biol. Phys.*, 56:384–390, 2003.

A. van Esch, T. Depuydt, and D. P. Huyskens. The use of an aSi-based EPID for routine absolute dosimetric pre-treatment verification of dynamic IMRT fields. *Radiother. Oncol.*, 71:223–234, 2004.

A. van Esch, B. Vanstraelen, J. Verstraete, G. Kutcher, and D. Huyskens. Pre-treatment dosimetric verification by means of a liquid-filled electronic portal imaging device during dynamic delivery of intensity modulated treatment fields. *Radiother. Oncol.*, 60:181–190, 2001.

M. van Herk. Physical aspects of a liquid-filled ionization-chamber with pulsed polarizing voltage. *Med. Phys.*, 18:692–702, 1991.

M. van Herk, D. Jaffray, P. Remeijer, J-J Sonke, M. Smitsmans, and J. Lebesque. Image guided radiotherapy. In *Proc. 14th Int. Conf on the Use of Computers in Radiation Therapy*. Jeong, 2004.

M. van Herk and J. Meertens. A matrix ionisation chamber imaging device for on-line patient setup verification during radiotherapy. *Radiother. Oncol.*, 11:369–78, 1988.

G. Vantienhoven, J. H. Lanson, D. Crabeels, S. Heukelom, and B. J. Mijnheer. Accuracy in tangential breast treatment set-up - a portal imaging study. *Radiother. Oncol.*, 22:317–322, 1991.

F. Verhaegen and J. Seuntjens. Monte Carlo modelling of external radiotherapy photon beams. *Phys. Med. Biol.*, 48:R107–R164, 2003.

D. Vetterli, H. Riem, D. M. Aebersold, R. H. Greiner, P. Manser, P. Cossmann, L. Kemmerling, E. J. Born, and R. Mini. Introduction of a novel dose saving acquisition mode for the PortalVision (TM) aS500 EPID to facilitate on-line patient setup verification. *Med. Phys.*, 31:828–831, 2004.

S. C. Vieira, M. L. P. Dirkx, B. J. M. Heijmen, and H. C. J. de Boer. SIFT: a method to verify the IMRT fluence delivered during patient treatment using an electronic portal imaging device. *Int. J. Radiat. Oncol. Biol. Phys.*, 60:981–993, 2004.

S. C. Vieira, M. L. P. Dirkx, K. L. Pasma, and B. J. M. Heijmen. Fast and accurate leaf verification for dynamic multileaf collimation using an electronic portal imaging device. *Med. Phys.*, 29:2034–2040, 2002.

E. Vigneault, J. Pouliot, J. Laverdiere, J. Roy, and M. Dorion. Electronic portal imaging device detection of radioopaque markers for the evaluation of prostate position during megavoltage irradiation: a clinical study. *Int. J. Radiat. Oncol. Biol. Phys.*, 37:205–212, 1997.

A. E. Schach von Wittenau, C. M. Logan, M. B. Aufderheide III, and D. M. Slone. Blurring artifacts in megavoltage radiography with a flat-panel imaging system: comparison of Monte Carlo simulations with measurements. *Med. Phys.*, 29:2559–70, 2002.

J. C. Wagner, E. L. Redmond II, S. P. Palmtag, and J. S. Hendricks. *MCNP: Multigroup/Adjoint Capabilities, LANL Report, LA-12704*. Los Alamos National Laboratory, Los Alamos, 1993.

B. R. B. Walters, I. Kawrakow, and D. W. O. Rogers. History by history statistical estimators in the BEAM code system. *Med. Phys.*, 29:2745–52, 2002.

B. R. B. Walters and D. W. O. Rogers. *DOSXYZnrc Users Manual, NRCC Report PIRS-794*. NRCC, Ottawa, 2002.

B. Warkentin, S. Steciw, S. Rathee, and B. G. Fallone. Dosimetric IMRT verification with a flat-panel EPID. *Med. Phys.*, 30:3143–3155, 2003.

S. Webb. *The Physics of Medical Imaging.* IOP Publishing, Bristol, 1988.

S. Webb. *The Physics of Conformal Radiotherapy.* IOP Publishing, Bristol, 1997.

D. R. White, J. Booz, R. Griffith, J. Spokas, and I. J. Wilson. *Tissue Substitutes in Radiation Dosimetry and Measurement, ICRU Report 44.* ICRU, 1988.

J. R. Williams and D. I. Thwaites, editors. *Radiotherapy physics in practice.* Oxford University Press, 2nd edition, 2000.

D. Yan, E. Ziaja, D. Jaffray, J. Wong, D. Brabbins, F. Vicini, and A. Martinez. The use of adaptive radiation therapy to reduce setup error: a prospective clinical study. *Int. J. Radiat. Oncol. Biol. Phys.*, 41:715–720, 1998.

F. F. Yin, M. C. Schell, and P. Rubin. Input/output characteristics of a matrix ion-chamber electronic portal imaging device. *Med. Phys.*, 21:1447–1454, 1994.

Y. P. Zhu, X. Q. Jiang, and J. Van Dyk. Portal dosimetry using a liquid ion-chamber matrix - dose response studies. *Med. Phys.*, 22:1101–1106, 1995.

Appendix A

DISSEMINATION OF WORK

Journal Publications

Chin PW, Spezi E and Lewis DG 2003 Monte Carlo simulation of portal dosimetry on a rectilinear voxel geometry: a variable gantry angle solution, Physics in Medicine & Biology **48** N231-8

Chin PW, Lewis DG and Spezi E 2004 Correction for dose-response variation in a scanning liquid ion chamber EPID as a function of linac gantry angle, Physics in Medicine & Biology **49** N93-103

Proffered Conference Presentations with Extended Abstracts

Chin PW, Lewis DG and Giddy J 2004 Implementation of BEAMnrc Monte Carlo simulations on the GRID, Proc 14th Int Conf on the Use of Computers in Radiation Therapy ed Yi BY, Ahn SD, Choi EK and Ha SW (Seoul: Jeong)

Chin PW and Lewis DG 2004 Monte Carlo portal dosimetry for segmented IMRT verification using the SLIC, Proc 8th Int Workshop in Electronic Portal Imaging (Brighton)

Chin PW, Lewis DG and Jarvis RJ 2004 The Varian aS500 as a dosemeter: preliminary investigations, Proc 8th Int Workshop in Electronic Portal Imaging (Brighton)

Chin PW and Lewis DG 2005 A Monte Carlo solution for external beam photon radiotherapy verification, Monte Carlo 2005 Conference – the Monte Carlo Method: Versatility Unbounded In A Dynamic Computing World (Chattanooga)

Proffered Conference Presentations with Short Abstracts

9th Annual Monte Carlo Users Group Meeting 2003, Edinburgh

All Wales Medical Physics & Clinical Engineering Summer Meeting 2003, Bodelwyddan

10th Annual Monte Carlo Users Group Meeting 2004, Teddington

Speaking of Science Postgraduate Conference 2004, Cardiff

Current Topics in Monte Carlo Treatment Planning 2004, Montreal

All Wales Medical Physics & Clinical Engineering Summer Meeting 2004, Cardiff

IPEM Annual Scientific Meeting 2004, York

11th Annual Monte Carlo Users Group Meeting 2005, Birmingham

Visiting Talks

2003 Virginia Commonwealth University, Richmond

2003 Royal Marsden Hospital, London